Doctoral theses at NTNU, 2023:242

Shabnam Karimi

Investigation of corrosion behavior, hydrogen uptake, and hydrogen embrittlement of armor wires made from carbon steels

Doctoral thesis

NTNU
Norwegian University of Science and Technology
Thesis for the Degree of Philosophiae Doctor
Faculty of Engineering
Department of Mechanical and Industrial Engineering

NTNU
Norwegian University of Science and Technology

Shabnam Karimi

Investigation of corrosion behavior, hydrogen uptake, and hydrogen embrittlement of armor wires made from carbon steels

Thesis for the Degree of Philosophiae Doctor

Trondheim, August 2023

Norwegian University of Science and Technology
Faculty of Engineering
Department of Mechanical and Industrial Engineering

NTNU
Norwegian University of
Science and Technology

NTNU
Norwegian University of Science and Technology

Thesis for the Degree of Philosophiae Doctor

Faculty of Engineering
Department of Mechanical and Industrial Engineering

ISBN 978-82-326-7184-7 (printed ver.)
ISBN 978-82-326-7183-0 (electronic ver.)
ISSN 1503-8181 (printed ver.)
ISSN 2703-8084 (online ver.)

Doctoral theses at NTNU, 2023:242

Printed by NTNU Grafisk senter

Preface

This thesis is submitted to describe the authentically performed investigations during a period from October 2018 to May 2022 at the Norwegian University of Science and Technology (NTNU) for partial fulfillment of the requirements for the degree of *Philosophiae Doctor*.

The Ph.D. work was carried out at the department of Mechanical and Industrial Engineering under the supervision of Professor Roy Johnsen, and Professor Afrooz Barnoush (from October 2018 until January 2020). Dr. Tarlan Hajilou, Professor Tom Depover, and Dr. Arne Dugstad were appointed as co-supervisors in this work.

The work was part of the project “Environmental Cracking of Flexible Pipe Armor Wires”. The project was financially supported by the Research Council of Norway, Equinor, Shell, Chevron, Petrobras, OKEA, TechnipFMC, NOV, Baker Hughes, and 4Subsea.

The thesis consists of two parts. The first part includes an introduction, a brief literature review, and a summary of the work. The second part includes three articles published in scientific journals.

Shabnam Karimi

August 2023, Trondheim

Acknowledgments

I would like to express my deepest gratitude to Afrooz Barnoush, my supervisor in the first year of my PhD. Although we worked together for a short period, I never forget his generosity in knowledge sharing, his enthusiasm for guiding me, and his dedication to science. I lost his supervision at the start of the second year of my PhD under a heartbreaking unfair situation. However, I was lucky enough to continue my PhD under the supervision of another amazing man, Roy Johnsen. I am extremely grateful to him for his invaluable advice, continuous support, and patience during my PhD.

I would like to thank and appreciate Tarlan Hajilou, my friend and my co-supervisor, not just for her enormous scientific support but also for her unique positive character that affected me deeply. Special thanks to Tom Depover, my co-supervisor for his generous support. The online meetings with him were always troubleshooting and gave me the courage to continue.

Everybody who had done a PhD knows that taking this journey would be very difficult without a special close comrade. Somebody that you can knock on her/his door whenever you face a challenge, somebody that you can celebrate your lab achievements with her/him, somebody that you can laugh and cry with her/him in challenging confrontations, somebody who is there all the time for you. I could not have undertaken this journey without my friend and my colleague, Iman Taji. I am very thankful for his presence.

I am thankful to Arne Dugstad, my co-supervisor, and Simona Palencsar for their contributions which are very influential in shaping my experiment methods and critiquing my results. I also like to acknowledge Kim Verbeken whom I had the honor to know and have his useful comments on my papers.

I would like to express my special gratitude to my family (whom I miss all the time), especially my parents for their belief in me which has kept my spirits and motivation high during this process.

Last but not least, I would like to extend my sincere thanks to my special friends in Trondheim, the people who are an important part of my life, the people who make a supportive joyful environment for me that allow me to share my emotions, my thoughts, my life and my love with them.

Abstract

The effect of cementite morphology on corrosion layer formation, hydrogen uptake, crack initiation, and growth in the presence of hydrogen was investigated in carbon steels which are used to fabricate armor wires in flexible pipelines.

In situ electrochemical micro-cantilever bending test was used to examine the crack initiation and growth path considering hydrogen interaction with the cementite morphology of the steels. To realize this, a miniaturized electrochemical three-electrode cell was incorporated into the Nanoindenter. The fabricated micro-cantilevers were bent under hydrogen-free and in situ hydrogen-charged conditions. It was shown that in spheroidite microstructure, the crack growth followed a straight path from the notch through the thickness of the micro-cantilever, and under high negative charging potentials (high hydrogen fugacity) the crack growth is independent of grain boundaries or ferrite-cementite interfaces. In the ferrite-pearlite microstructure, competition between the shear mechanism and the interfacial cracking determines the crack growth path.

The linear polarization resistance and weight loss tests were used to examine the effect of cementite morphology on the corrosion layer formation on carbon steels in an aqueous solution containing CO_2 and CO_2/H_2S. After the corrosion test, the corrosion layers that formed on the carbon steel surfaces were characterized using scanning electron microscopy-energy dispersive spectroscopy, focus ion beam, and x-ray photoelectron spectroscopy to reveal the effect of cementite morphology on the layer formation and corresponding corrosion properties. It was revealed that as the cementite phase fraction is increased, the corrosion rate increases in the CO_2 environment, while no similar trend was observed in the CO_2/H_2S environment, since the iron sulfide layer which formed immediately after the exposure prevented corrosion on the substrate material. Under CO_2 exposure, the corrosion rate of the materials with lamellar ferrite-pearlite microstructures was higher than the materials with a spheroidite microstructure. A mechanism that explains the role of cementite morphology on corrosion layer formation in a CO_2 environment is proposed for the studied materials.

Hydrogen thermal desorption and hot extraction analysis were performed on the studied materials after exposure to three different environments (an aqueous solution with CO_2 bubbling, CO_2/H_2S bubbling, and cathodic charging) to investigate the influence of the charging condition and environment, the cementite morphology, and the corrosion layer on the hydrogen uptake and hydrogen desorption. The hydrogen uptake is substantially higher in the CO_2/H_2S environment compared to the CO_2 environment for all materials. The hydrogen

uptake increases with carbon content in the CO_2/H_2S environment and under cathodic charging. The lamellar cementite morphology absorbed more hydrogen than the material with spheroidite microstructure with almost the same amount of carbon content in the microstructure. The corrosion layer formed on the steels in the CO_2 environment strongly affects the hydrogen effusion and the thermal desorption spectroscopy spectrum, while the corrosion layer formed in the CO_2/H_2S environment does not show this effect.

Contents

List of Figures

List of Tables

Abbreviations

AIDE	Adsorption-induced dislocation emission
EBSD	Electron back scattered diffraction technique
ECCB	Electrochemical micro-cantilever bending
EDM	Electrochemical discharge machining technique
EDS	Energy dispersive spectroscopy
EELS	Electron energy loss spectroscopy
FIB	Focus ion beam
HE	Hydrogen embrittlement
HEDE	Hydrogen-enhanced decohesion
HELP	Hydrogen-enhanced localized plasticity
HER	Hydrogen evolution reaction
L-Δ	load-displacement curves
LPR	Linear polarization resistance
SEM	Scanning electron microscopy
STEM	Scanning transmission electron microscope
TCD	Thermal conductivity detector
TDS	Thermal desorption spectroscopy
TEM	Transmission electron microscopy
UHV	Ultra-high vacuum
UTS	Ultimate tensile strength
XPS	X-ray photoelectron spectroscopy
YS	Yield strength

Part I

Thesis overview

This thesis consists of two parts, an introductory part, and three research papers that were published in scientific journals. The first part is the introductory part that provides the motivation, research objectives and scopes, the fundamental background, the main testing methods applied in this thesis work, a summary of the journal papers on the thesis topic, the main conclusions, and an outlook for future works. In the second part, the publications that have been published in scientific journals are collected.

List of papers and contributions

Three research papers published to peer-review journals are included in this thesis. The details of the papers and author contributions are presented below.

Peer-review journal papers

1. Shabnam Karimi, Iman Taji, Tarlan Hajilou, Afrooz Barnoush, and Roy Johnsen. "Evaluation of the cementite morphology influence on the hydrogen induced crack nucleation and propagation path in carbon steels." *International Journal of Hydrogen Energy* 47, no. 30 (2022): 14121-14129.
2. Shabnam Karimi, Iman Taji, Tarlan Hajilou, Simona Palencsar, Arne Dugstad, Afrooz Barnoush, Kim Verbeken, Tom Depover, and Roy Johnsen. "Role of cementite morphology on corrosion layer formation of high-strength carbon steels in sweet and sour environments. " *Corrosion Science 214 (2023) 111031.*
3. Shabnam Karimi, Iman Taji, Simona Palencsar, Arne Dugstad, Tarlan Hajilou, Afrooz Barnoush, Kim Verbeken, Roy Johnsen, and Tom Depover. "Evaluation of microstructural and environmental effects on the hydrogen uptake and desorption in high-strength carbon steels: a thermal desorption spectroscopy study. " *Corrosion Science 219 (2023) 111210* .

Statement of author contributions

Shabnam Karimi planned and conducted the experimental work, analyzed the data, and prepared the full manuscript. Iman Taji and Tarlan Hjilou helped with planning the tests, the experimental work, and analyzing the data. Simona Palencsar and Arne Dugstad performed the corrosion tests at the institute for energy technology. Tom Depover helped with the TDS

experiments. Roy Johnsen contributed to planning the tests and intellectual discussions on data analysis. All the authors contributed to revising the manuscripts.

Other peer-review journal publications that are not included in the thesis, but including contribution from the PhD candidate performed as part of the PhD project:

1. Iman Taji, Tarlan Hajilou, Anna Sophie Ebner, Daniel Scheiber, Shabnam Karimi, Ernst Plesiutschnig, Werner Ecker, Afrooz Barnoush, Verena Maier-Kiener, Roy Johnsen, Vsevolod I Razumovskiy. "Hydrogen assisted intergranular cracking of alloy 725: The effect of boron and copper alloying" *Corrosion Science* 203 (2022): 110331.
2. Iman Taji, Tarlan Hajilou, Shabnam Karimi, Florian Schott, Ernst Plesiutschnig, Afrooz Barnoush, Roy Johnsen. "Role of grain boundaries in hydrogen embrittlement of alloy 725: single and bi-crystal microcantilever bending study" *International Journal of Hydrogen Energy* 47, no. 25 (2022): 12771-1278.

1. Introduction

1.1 Motivation

Flexible pipes are critical elements in the offshore oil and gas industry. They are applied for the transition of fluids, gas, and hydrocarbons between the installations located at the seabed and the production facilities. As displayed in Fig.1.1[3], flexible pipes encompass several layers made from different materials to fulfill stiffness, strength, and fluid contaminants requirements and each layer plays a particular role. A flexible pipe is mainly composed of five layers: the carcass layer which is the nearest layer to the bore and made of a corrosion-resistant alloy, a polymer sheath, a pressure armor layer made of steel, a tensile armor layer made of high-strength steel, and the outer polymeric layer [4]. If there are damages in the inner polymeric layer, the water containing corrosive species like CO_2 and H_2S can penetrate from the bore into the annulus space around the armor wires. The presence of these corrosive species can cause corrosion and hydrogen embrittlement (HE) of the armor wires [5]. The corrosion process and the cathodic protection of the wires can generate atomic hydrogen and introduce it to the wires through the damages in the outer polymeric layer. The failure mechanisms' explanation when damages, fractures, and corrosion attacks occur in flexible pipes can be very complicated [6].

To be able to explain the complicated failure mechanisms of flexible pipes, understanding the the combined effect of the environmental conditions and the role of the microstructure of the

Figure 0.1. The cross-section of an unbonded flexible pipe [3].

armor wire steels on the corrosion behavior and hydrogen uptake, are important research questions to be answered. In this thesis, several high-strength steels which are used in the armor wires (later called armor wires) in flexible pipes are included to study the role of microstructure, particularly the role of cementite morphology and distribution, on fracture behavior in the presence of hydrogen. Besides, the environmental effects coupling with the steel microstructure's role on corrosion, corrosion layer formation, and hydrogen uptake in CO_2 and CO_2/H_2S environments are investigated.

1.2 Tensile armor layer

Each armor wire composes of several carbon steel wires with a rectangular cross-section laid at an angle usually between 30 and 35 degrees from the pipe's longitudinal axis giving it a helical shape. Cold-drawn and heat-treated carbon steels are often used in the armor wires due to the development of fields and immersing the pipes in deeper water and the consequent increased mechanical loads on flexible pipes [7], [8].

The armor wires provide the tensile strength in the pipe to resist axial stress due to internal pressure and external forces. The weight of the flexible pipe is carried by armor wires to keep the integrity of the pipe. Two or four layers of armor wires are used in the pipe structure and

the lay direction of each layer alternate to avoid torsion during tension loading. Any damage to the armor wires could crucially decrease the load capacity of the flexible pipe. The rupture of armor wires is one of the most severe failures that can happen in flexible pipes which may lead to the failure of the whole structure. Different failure modes and mechanisms for armor wires include burst (rupture of tensile armor due to excess internal pressure), tensile failure (rupture of tensile armor due to excess tension), compressive failure (bird-caging of armor wires), over-bending (unlocking of interlocked pressure or tensile armor layer), torsional failure (failure of armor wires, bird-caging of armor wires), fatigue failure (Armor wire fatigue) and corrosion (tensile armor exposed to seawater or diffused product).

1.3 Research objectives

This work focuses on the role of the microstructure on corrosion, hydrogen uptake, and mechanical behavior in the presence of hydrogen in carbon steels used as armor wires. The effect of the distribution and the morphology of the cementite phase formed in the microstructure during the thermo-mechanical processes, on the HE was studied in small-scale tests using in situ electrochemical micro-cantilever bending (ECCB) technique. In addition, the interaction between the cementite morphology, corrosion behavior, and corrosion layer formation was investigated by doing linear polarization resistance (LPR) tests and Focus ion beam (FIB) and SEM characterization of the corrosion layers formed in simulated environments containing CO_2 and H_2S species at room temperature. The hydrogen uptake capacitance of different microstructures with different cementite morphologies was studied based on thermal desorption spectroscopy (TDS) and hot extraction test results. The main objectives of this work are as follows:

- Establish the correlation between the lamellar and spherical cementite morphology and the fracture mechanism in the presence of hydrogen.
- Investigate the combined effect of environment and cementite morphology on corrosion under exposure to CO_2 and CO_2/H_2S.
- Reveal the role of microstructure and especially the cementite morphology on the corrosion layer formation in both CO_2 and CO_2/H_2S environments.
- Investigate the effect of environmental conditions, microstructures, and corrosion layers on the hydrogen uptake, hydrogen effusion, and TDS spectrum.

2. Degradation of armor wires

A flexible pipe may fail and lose its integrity due to various damage and failure mechanisms. One of the main damages that have received remarkable attention is corrosion. Any damage in the internal polymeric layer (see Fig.1.1) of the flexible pipes may lead to corrosive species like CO_2, H_2S, and O_2 diffusing into the annulus space around the armor wires and causing the corrosion of armor wires. The application of carbon steels is more popular for pipelines than corrosion resistance alloys and stainless steels because they are more cost-effective. However, the application prospects of carbon steels in armor wires remain limited due to their susceptibility to corrosion failures in sweet (CO_2-containing) and sour (H_2S-containing) environments. Sweet corrosion is the most frequent type of corrosion which occurs in oils containing a high partial pressure of CO_2. Sour corrosion generally occurs in oils containing H_2S at partial pressures higher than 0.003 atm. The partial pressure ratio of CO_2 and H_2S (pCO_2/pH_2S) defines the corrosion type. Although there is no consensus about this ratio, ratios lower than 20 and higher than 500 seem to sort sweet and sour corrosion, respectively [8]. The corrosion failure cases of armor wires are usually due to the inadequate understanding of the corrosion process of carbon steels in sweet and sour environments [9]–[11].

2.1 Sweet Corrosion

Sweet corrosion (CO_2 corrosion) of carbon steels in an aqueous solution is one of the most serious problems in the oil and gas industry since 1940. After the use of CO_2 as a technique to enhance oil recovery and reduce greenhouse gas emissions in oil production and transport, the understanding of CO_2 corrosion of carbon steels has become more essential [11], [12].

In the aqueous CO_2 environment, dissolved CO_2 hydrates form carbonic acid. Carbonic acid dissociates into a hydrogen ion and a bicarbonate ion which dissociates to give another hydrogen ion and a carbonate ion. The corrosion process of carbon steel occurs through the anodic dissolution of iron and the cathodic evolution of hydrogen. There is a consensus in the literature that the rate of the cathodic process or hydrogen evolution reaction (HER) on steel is increased in the presence of CO_2 in comparison with the strong acid solutions with constant pH [13]–[15]. This fact is generally used in oil and gas industries to explain the high level of corrosion rate in CO_2-containing solutions [16]. Different cathodic process mechanisms have been extensively discussed:

- The direct reduction mechanism which is the direct reduction of H_2CO_3 [14], [16]

- The buffering effect mechanism in which the dissolved CO_2 constitutes an additional reservoir for HER [17]
- H_2O reduction [18]

De Waard and Milliams [19] are the first scientists who proposed the direct reduction mechanism of H_2CO_3 in an aqueous solution occurs on steel surface as follows:

$$H_2CO_{3(ads)} + e^- \rightarrow H_{(ads)} + HCO^-_{3(ads)} \quad (1)$$

$$HCO^-_{3(ads)} + H^+ \rightarrow H_2CO_{3(ads)} \quad (2)$$

$$2H_{(ads)} \rightarrow H_2 \quad (3)$$

The buffering effect mechanism can explain the increase of HER in CO_2-containing solutions as follows [17]:

$$H_2O + CO_{2(aq)} \rightarrow HCO_3^- + H^+ \quad (4)$$

$$HCO_3^- \rightarrow CO_3^{2-} + H^+ \quad (5)$$

$$2H^+ + 2e^- \rightarrow H_2 \quad (6)$$

And the water reduction which only plays a significant role at very high pH or very low partial pressure of CO_2 [18], [20] is as follows:

$$H_2O_{eq} + e^- \rightarrow \frac{1}{2}H_{2(g)} + OH^-_{eq} \quad (7)$$

The anodic dissolution of iron (Eq.8) is also affected by CO_2 presence and the kinetic of iron dissolution in CO_2-containing solutions is different than the kinetic in strong acids. This difference is due to the carbonic species which act as a chemical ligand and accelerate the dissolution of iron [21].

$$Fe^{2+} + 2e^- \rightarrow Fe \quad (8)$$

The CO_2 corrosion process is often accompanied by scale formation. The overall reaction is:

$$Fe + CO_2 + H_2O \rightarrow FeCO_3 + H_2 \quad (9)$$

The most common type of corrosion layer formed in CO_2 corrosion is iron carbonate ($FeCO_3$). It is believed that $FeCO_3$ precipitation is achieved when the concentrations of Fe^{2+} and CO_3^{2-} exceed the solubility limit. However, the corrosion of carbon steel leads to a higher pH at the steel-electrolyte interface which in turn leads to an increase in CO_3^{2-} concentration at the surface, and less Fe^{2+} concentration is required to exceed the $FeCO_3$ solubility limit [22], [23]. This corrosion layer can be protective and reduce the corrosion rate by several order of magnitude in some instances or non-protective depending on the conditions under which it is formed [21], [24]. It can decrease the corrosion rate by providing a diffusion barrier for the corrosion species transfer and covering a part of the steel surface. The corrosion layers' properties like thickness, composition, morphology, and porosity control the diffusion of the corrosion products and reactants through the layer and govern the rate of corrosion.

2.2 Sour Corrosion

The carbon steel corrosion in aqueous solutions containing dissolved H_2S and CO_2 is called sour corrosion (CO_2/H_2S corrosion). In a coexistence system of CO_2–H_2S, even a small amount of H_2S has a considerable effect on CO_2 corrosion and the corrosion behavior is more obscure and complex to understand [25]. Although the low concentrations of H_2S can inhibit the corrosion process due to the protective iron sulfide film formation on the steel surface, the high H_2S concentrations can cause severe corrosion and a catastrophic failure [26], [27], [28].
Hydrogen sulfide (H_2S) is a usual species in the reservoirs of natural gas. The sour corrosion of carbon steel in the presence of H_2S is the result of the dissolution of iron (Eq.8) as the main anodic reaction, accompanied by different cathodic reactions. Exactly like CO_2, H_2S can dissolve in an aqueous solution and make a weak acid (Eq.10) which can hydrate and result in the sour corrosion of carbon steel.

$$H_2S_{(g)} \rightarrow H_2S_{(aq)} \quad (10)$$

$$H_2S_{(aq)} \rightarrow HS^-_{(aq)} + H^+_{(aq)} \quad (11)$$

$$HS^-_{(aq)} \rightarrow S^{2-}_{(aq)} + H^+_{(aq)} \quad (12)$$

Therefore, both CO_2 and H_2S provide oxidizing power and raise iron corrosion by establishing an equilibrium between the anodic and cathodic reactions. Much like sweet environments which are previously discussed, different cathodic process mechanisms were regarded in the

literature for the sour environment. The direct dissociation of H_2S (Eq.13) [29], the reduction of H^+ (Eq.6) in which H_2S plays a buffering role in the mechanism, and H_2O reduction (Eq.7). Based on recent studies, under oil and gas transportation, the dominant cathodic reaction in both sweet and sour environments is H^+ reduction (Eq.6) [30], [31] [32].

$$H_2S + e^- \rightarrow HS^- + \frac{1}{2}H_2 \quad (13)$$

Shoesmith et al. stated that the corrosion reaction of iron in a sour environment occurs predominantly by a solid-state reaction [33]:

$$Fe + H_2S \rightarrow FeS + H_2 \quad (14)$$

The formation of the protective FeS (mackinawite) scale is the main parameter for corrosion control, rather than the electrochemical kinetics [26], [34].

2.3 Hydrogen uptake in CO_2 and CO_2/H_2S environment

Hydrogen damage is one of the most destructive types of corrosion in CO_2 and CO_2/H_2S environments which can be known as hydrogen-type corrosion or hydrogen embrittlement (HE) [35]. Hydrogen can enter the metal from two sources: one is the internal hydrogen or the entering of hydrogen into the metal from the thermomechanical and chemical processes such as pickling, cathodic hydrogenation, electroplating, heat treatment, etc. The other source is the external hydrogen or entering of hydrogen into the metal from hydrogen-generating species (like CO_2 and H_2S, etc) which is produced during the corrosion process. The cathodic corrosion reaction in CO_2 and H_2S environments is the main source of hydrogen production [36]. After the atomic hydrogen absorbs into the metal, it can diffuse through the lattice or along the grain boundaries and occupy the microstructure defects such as interfaces, grain boundaries, voids, etc. These microstructure defects are categorized as hydrogen traps. The traps can be reversible or irreversible depending on their hydrogen binding energies. The hydrogen traps have a considerable effect on hydrogen diffusion [37].

The hydrogen uptake in carbon steels depends on different factors such as the environment, the surface condition, and the steel microstructure [4]. H_2S is a major source of hydrogen. It reacts with the steel surface to produce iron sulfide and releases hydrogen previously bonded with sulfur that can be absorbed and cause a decrease in mechanical properties [38]. Moreover, H_2S

hinders the transformation of atomic hydrogen into hydrogen molecules and facilitates the diffusion of atomic hydrogen into steel [39]. Although CO_2 is less aggressive than H_2S in increasing the adsorption of hydrogen in steels, it can have a direct contribution to the hydrogen uptake in carbon steels due to the enhanced cathodic reaction rate in its presence in an aqueous solution [14]. However, the corrosion products which form on the carbon steel surface are one of the important parameters that affect both the corrosion rate and the hydrogen uptake [40]. The corrosion products can block the hydrogen entry into the material or be considered as a hydrogen reservoir that can increase hydrogen absorption [41], [42], [43].

2.4 Hydrogen embrittlement (HE)

HE is a failure mechanism that occurs in a susceptible microstructure in the presence of elemental hydrogen and mechanical stress. As mentioned in the previous section, hydrogen can be introduced to the steel during the manufacturing process or its application and use. To explain the HE mechanism, different theories have been proposed in literature such as hydrogen-enhanced localized plasticity (HELP) [44], hydride formation [2], hydrogen-enhanced decohesion (HEDE) [45], hydrogen-enhanced strain-induced vacancies [46], adsorption-induced dislocation emission (AIDE) [47], and the defactant theory [48].
The HELP mechanism (Fig.2.1) is based on the idea that the presence of hydrogen in a solid solution declines the obstacles to dislocation motion, thereby intensifying the amount of deformation that occurs in a localized zone adjacent to the fracture surface. Therefore, the fracture process is a highly localized plastic failure process rather than embrittlement and the root cause of the HE in this mechanism is the increase in the dislocation velocity, e.g., by the formation of very shallow and localized micro-voids and a localized reduction in flow stress. The resultant fracture surface has a macroscopically brittle appearance.

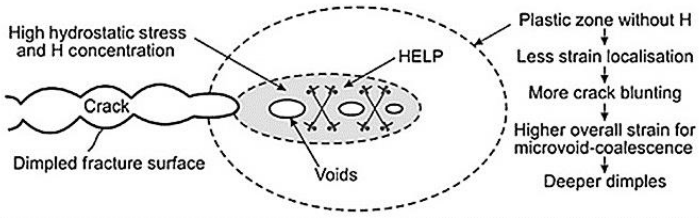

Figure 2.1. Schematic diagram of HELP mechanism [1].

Hydride formation (Fig.2.2) is a mechanism based on the formation and fracture of hydrides at crack tips. In this mechanism, the hydrogen diffuses to the regions with high hydrostatic stress at the crack tip and results in the nucleation and growth of the hydride phase. The cleavage of the hydride occurs when it reaches a critical size and the progressive crack is arrested at the hydride-matrix interface [2]. The hydrogen-enhanced strain-induced vacancies mechanism has a close concept to the HELP mechanism. It occurs due to the decrease in the formation energy of vacancy in the presence of hydrogen [49].

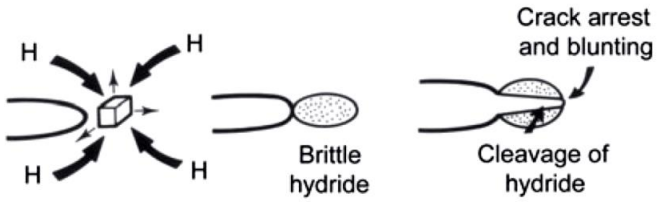

Figure 2.2. Schematic diagram of hydride formation mechanism [2].

In the HEDE mechanism (Fig.2.3), hydrogen accumulates at regions of high stress and results in the weakening of the interatomic bonds (Fe-Fe). Indeed, this weakening occurs when hydrogen donates its 1s electron to the unfilled 3d shell of the iron atoms. This mechanism involves also the decohesion at grain boundaries and particle/matrix interfaces ahead of the crack due to the hydrogen segregation in these regions.

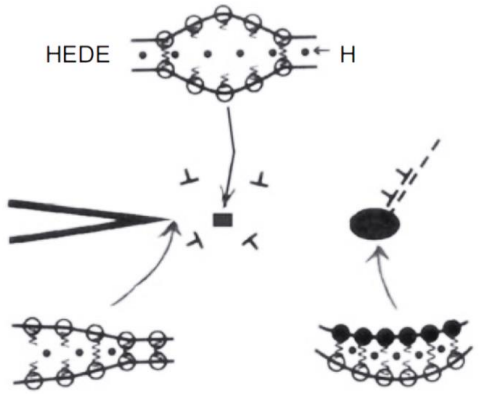

Figure 2.3. Schematic diagram of HEDE mechanism [2].

For the adsorption-induced dislocation emission (AIDE) mechanism (Fig.2.4) both nucleation and subsequent movement of dislocations away from the crack tip are considered. It is important to mention that the nucleation step is critical and facilitated by hydrogen adsorption. After nucleation, dislocations can move away from the crack tip under the applied stress. Indeed, when a dislocation core is made in the nucleation step the breaking and reforming of interatomic bonds occur over several atomic distances which can facilitate the process [2].
Based on the defactant theory, the activation energy for dislocation nucleation is reduced by hydrogen. In this mechanism, hydrogen can facilitates the dislocation nucleation and decrease the energy of the double kink nucleation for screw dislocations [50], [51]. HE susceptibility of carbon steels is one of the most important concerns for material selection in the oil and gas industry [52]. The produced H^+ during the cathodic reactions in sweet and sour environments can adsorb on the steel surface. The adsorbed H^+ is reduced to elemental H and absorbed into the steel which can result in HE. When elemental hydrogen ingresses into the steel, it can occupy the lattice sites or the microstructural sites that show a higher affinity for hydrogen than the lattice. These microstructural sites such as dislocations, vacancies, grain boundaries, voids,

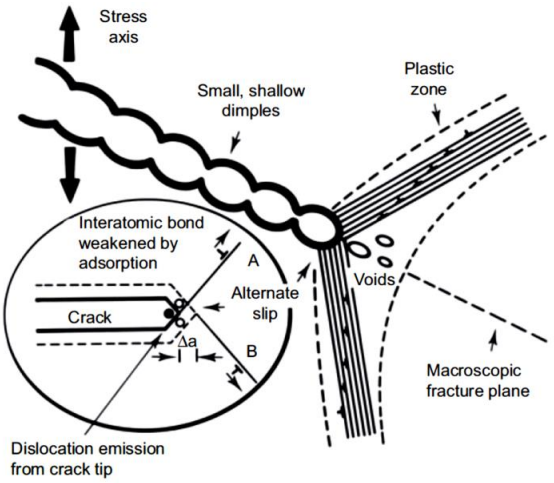

Figure 2.4. Schematic diagram of AIDE mechanism [41].

phase boundaries and some intermetallic particles function as hydrogen traps in steels. The hydrogen traps can cause hydrogen fixation or hydrogen dispersion and the hydrogen motion in the steel is affected by them. The higher binding energy of hydrogen with the hydrogen trap leads to a stronger stability of hydrogen in the trap [53].

Johnson declared for the first time in 1875 that only diffusible hydrogen can cause HE [54] and that the susceptibility to HE is highly dependent upon diffusible hydrogen (reversible or trapped weakly) not non-diffusible (irreversible or trapped strongly) [55]. The diffusible hydrogen can accumulate in the regions with a high level of stress in the steel and facilitate crack initiation and propagation.

2.5 Carbon steel microstructure effect

The carbon steel microstructure is a crucial aspect of material design and selection in armor wires. Considering a specified chemical composition, the nature of the microstructure, the degree of deformation, and the shape, size, and distribution of the carbide phase (cementite, Fe_3C) are usually what determines the steel corrosion resistance in CO_2 and CO_2/H_2S environments [56]. In fact, the driving force for corrosion in aqueous environments is the heterogeneities in the microstructure and the resultant potential difference of small areas. In this regard, the different phases in the steel microstructure can act as anodic or cathodic preferential sites during the corrosion process. Cementite (Fe_3C) functions as a preferential site for the hydrogen cathodic reaction in ferrite-pearlite steels [57]. A large number of researches published that the ferrite-pearlite microstructures show more resistance to CO_2 corrosion than martensitic steels [58], while some other studies reported an opposite behavior [59], [60]. However, there is an agreement in the literature that the corrosion product's formation and properties and its adherence to the steel surface are dependent on the steel microstructure [61], [62], [63]. The higher corrosion resistance of the lamellar ferritic-pearlitic microstructure than the martensitic or bainitic steels is because the lamellar cementite phase provides a stronger adherence to $FeCO_3$ protective film. As mentioned in section 2.1, the formation of a protective layer of $FeCO_3$, in CO_2 environments can prevent the diffusion of corrosive specimens and the dissolution of the steel [16]. Therefore, the cementite morphology in carbon steel microstructures plays a vital role in the steel corrosion behavior.

As noted previously, the HE susceptibility of steel is mostly determined by the hydrogen diffusivity and the hydrogen uptake capacity [64]. Therefore, the most important factors that determine the HE susceptibility of a microstructure are the hydrogen trapping sites and hydrogen permeability and diffusion in that microstructure. It has been noted in the literature that carbon steel with as-quenched martensitic microstructure shows less HE resistance, while tempered martensitic or tempered bainitic microstructures show the highest level of HE resistance. Pearlitic microstructures and spheroidite microstructures HE resistance are in the

middle of the two abovementioned ones [65]. However, in high-strength carbon steel with ferritic-pearlitic microstructures, the ferrite–cementite interfaces are the main trapping sites and the effective diffusion coefficients increase with a decrease in the ferrite–cementite interface area [66].

The role of microstructure in HE is a complex issue that needs more investigation. Nonetheless, some considerations are highly effective in HE resistance in a microstructure and they should not be ignored, such as the morphology of the martensite or pearlite, the phase distribution, the presence of retained austenite, the interfaces, etc. [67].

3. Experimental procedure

The details of experimental procedures are mainly presented in the respective papers concluded from this Ph.D. work. However, a general overview of the methodology and the used equipment is provided in this section.

3.1 Materials and sample preparation

Four types of carbon steels that are applied as armor wires in pipelines were used in this Ph.D. thesis. The samples are named based on their carbon content, CS28, CS62, CS65, and CS83 (for instance the carbon content of material CS65 is 0.65%). The compositions and mechanical properties of these four steels are listed in Table 3.1. The carbon steels are armor wires of flexible pipes, received in the form of drawn curved wires with different widths of 9 to 12 mm and a thickness of 3 mm.

Table 3.1. Chemical composition in wt% and the mechanical properties (yield strength (YS), and ultimate tensile strength (UTS) of the studied materials [66].

Element	C	Al	Si	P	Mo	V	Cr	Mn	Ni	Cu	YS(MPa)	UTS(MPa)
CS28	0.28	0.32	0.32	0.2	0.2	0.4	0.42	0.72	0.46	0.62	800	850
CS62	0.62	0.26	0.40	0.23	0.46	0.70	0.61	1.36	0.89	0.75	1100	1300
CS65	0.65	0.30	0.24	0.20	0.35	0.51	0.51	0.96	0.60	0.75	1250	1400
CS83	0.83	0.19	0.35	0.30	0.35	0.54	0.55	1.07	0.69	0.59	1400	1600

The microstructure of the studied materials is shown in Fig.3.1. In general the microstructure of all materials includes ferrite and cementite. However, the cementite morphology and distribution are not the same in different materials microstructures. Material CS28 is a low-carbon steel with both large and small drawn ferrite grains, including different types of small ferrite sub grains The cementite particles continuously precipitated mainly along the grain boundaries, while a small fraction of cementite particles was dispersed inside the ferrite grains. Materials CS62 and CS65 are high-carbon steels that exhibited a ferrite-cementite microstructure with small fractions of ferrite. The morphology of the cementite in material CS62 consisted of spherical particles or broken lamellae in a ferrite matrix, whereas material CS65 showed a pearlite microstructure with thick lamellae of cementite in a ferrite matrix. The ferrite grain size and connection network between the ferritic grains were larger in material CS65 than in material CS62. Material CS83 was a hypereutectoid high-carbon steel that

exhibited a predominantly lamellar pearlite microstructure with a lower fraction of ferrite than the other materials. The ferrite, cementite, and pearlite phase fractions for all materials were determined by image analysis using ImageJ, and the data are listed in Table 3.2.

Table 3.2. Microstructures phase fraction and interlamellar spacing [68].

Element	Ferrite (%)	Cementite (%)	Pearlite (%)	Interlamellar spacing (nm)
CS28	96	4	35	-
CS62	91	9	81	-
CS65	90	10	85	242±64
CS83	80	12	98	117±30

The following investigations were performed for each of the materials:

- Microstructure characterization with scanning electron microscopy (SEM), and Micro-cantilever bending test:

The studied materials were cut into disk shape samples using the electrochemical discharge machining technique (EDM) with a diameter of 9 to 12 mm (each wire had a different width) and a thickness the same as the original wires. All the samples were ground sequentially from 120 to 4000 grit SiC papers followed by mechanical polishing up to 1µm diamond suspensions and finally etched in 2% nital solution.

- Transmission electron microscopy (TEM):

After the micro-cantilever bending test, to investigate the crack propagation path under the notch root, the notch area was covered by a platinum-carbon layer using focused ion beam (FIB) deposition to prevent any damage to the crack by the gallium ion beam. Then the cross-sections normal to the cantilever directions were milled and sliced by FIB. Each slicing step was 100 to 200 nm in thickness. The final thickness of the TEM sample was 100 nm.

- Corrosion test, Thermal desorption spectroscopy (TDS) test, X-ray photoelectron spectroscopy (XPS), and Energy dispersive spectroscopy (EDS):

The as-received wires were cut into rectangular specimens with a length of 12 mm and the same width and thickness as the original wires. All surfaces were ground with 320 grit SiC paper washed in acetone and isopropanol in an ultrasound bath, and dried.

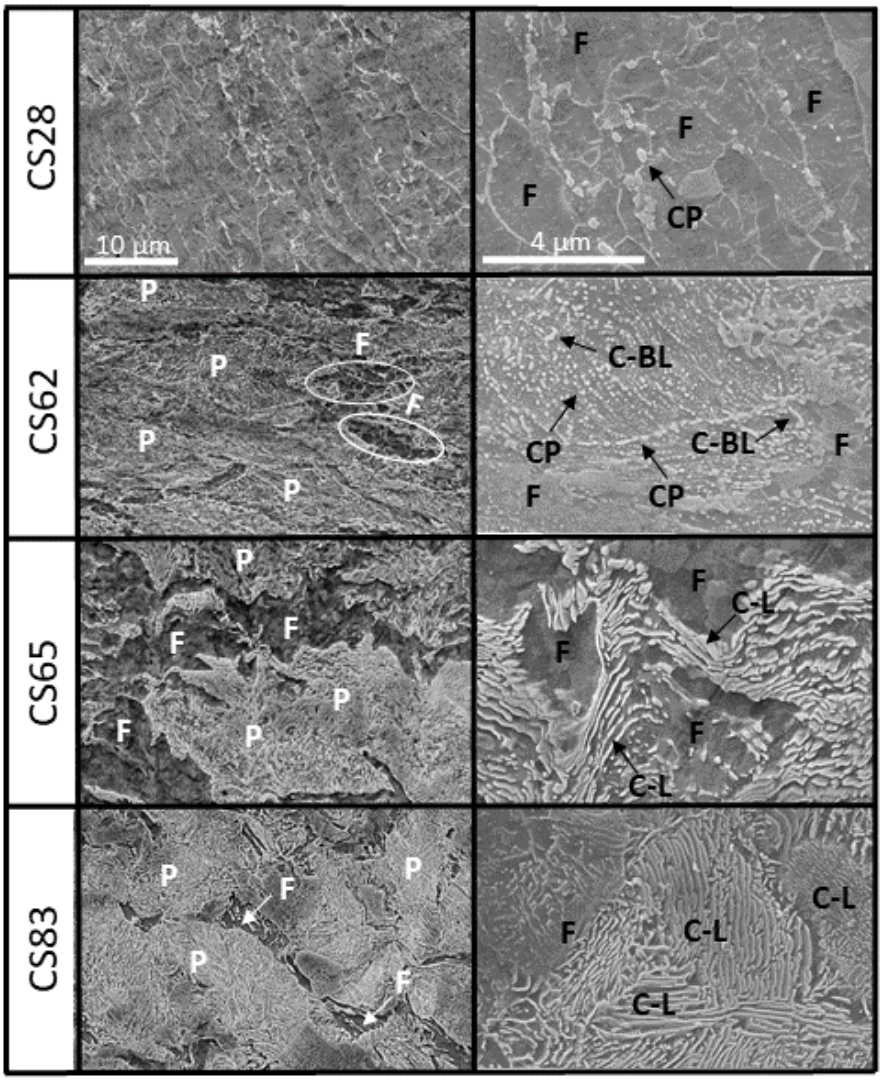

Figure 3.1. S EM micrographs of the studied materials surface. The right column shows the high magnification images of the microstructure of the materials. The magnification of the S EM images in each column is the same for all materials. The ferrite and pearlite phases are marked by F and P, respectively. The cementite particles, cementite lamellae, and broken lamella of cementite are marked by C-P, C-L, and C-BL, respectively [68].

3.2 Hydrogen charging

3.2.1 Electrochemical hydrogen charging

The hydrogen charging electrolyte used for the ECCB test is a glycerol-based solution, which consists of 1.3 molar borax (sodium tetraborate decahydrate) dissolved in glycerol. 1g/l

thiourea dissolved in 20 vol.% distilled water is added as a poison to increase the efficiency of hydrogen absorption [69]. This glycerol-based electrolyte can protect the sample surface from corrosion during the test because of its extremely low oxygen solubility and diffusivity [51]. For hydrogen charging of the specimens for the ECCB test, an integrated miniaturized three-electrode electrochemical cell with a platinum counter electrode was used. The counter electrode was immersed in the cell electrolyte. $Hg/HgSO_4$ was used as the reference electrode to avoid the surface attack which can be made by chloride ions (The Cl^- ions which can be found in Calomel or Ag/AgCl electrodes, do not exist in this electrode. Cl^- ions can interfere with the corrosion reactions). The reference electrode was connected to the cell through a tube that contains a similar solution as the charging electrolyte (Fig.3.2). The micro-cantilevers were potentiostatically charged at -1050 and -1550 mV versus Ag/AgCl (the potentials were converted and reported versus Ag/AgCl). The hydrogen charging was performed at room temperature.

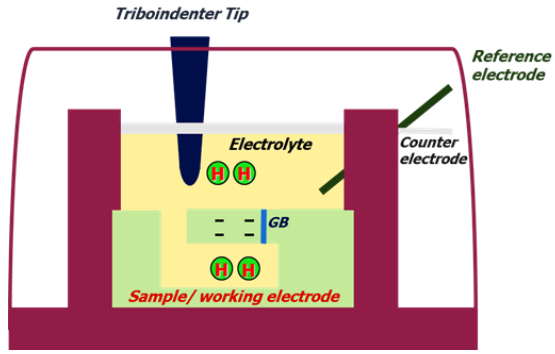

Figure 3.2. Schematic drawing of the in situ ECCB test setup.

Another set of samples that were prepared for doing the TDS tests were electrochemically charged in a three-electrode cell using a 3.5% NaCl solution at a constant potential of -1400 mV versus an Ag/AgCl reference electrode. 1 g/L thiourea was added to the solution as a poison. A piece of platinum wire was used as the counter electrode (Fig.3.3). Samples of carbon steels with high carbon content, CS62, CS65, and CS83, (later called high-carbon steel) were charged in this cell for a duration securing saturation of the samples. The charging duration was aquired based on Fick's law of diffusion [70], using the permeation diffusivity data from Skilbred et al. study on the same materials used in this PhD [66].

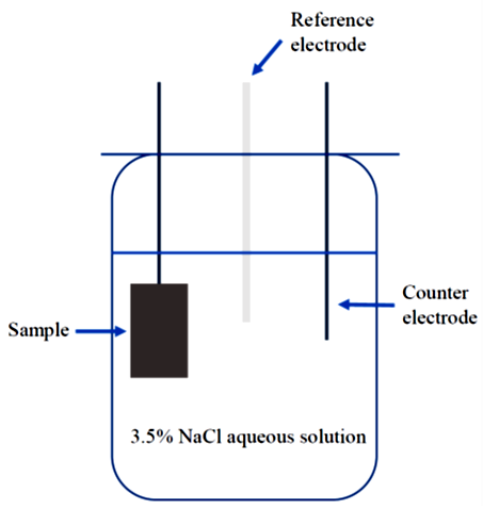

Figure 3.3. Schematic drawing of the three-electrode charging cell for electrochemical hydrogen charging.

3.2.2 Hydrogen charging during the corrosion test

Modified ASTM D1141-90 seawater (without calcium chloride to avoid the formation of calcium carbonate) [71] was used as the corrosion test electrolyte. The corrosion tests were performed in a setup comprising two parts: the test cell, where the samples were immersed in the electrolyte, and the refill cell, which contained the fresh electrolyte required to replenish the electrolyte in the test cell (Fig.3.4.). Both the test cell and the refill cell were continuously purged with the required gas mixture. A gas-dosing system based on the Bronkhorst mass flow controller was used to blend the N_2, CO_2, and H_2S. Both cells were kept at room temperature. The analysis of the hydrogen uptake in the samples during the corrosion test and the comparison between the hydrogen uptake after electrochemical charging and after the corrosion test is a part of this thesis.

The hydrogen charging conditions in CO_2 and CO_2/H_2S environments are summarized as follows:

- CO_2 exposure: 25 °C, 0.2 bar CO_2, gas flow: 200ml/min in modified ASTM seawater (no Ca^{2+}), low Fe^{2+} concentration due to electrolyte replacement (100-250 ml/h), exposure time: 21 days.
- CO_2/H_2S exposure: 25 °C, 0.2 bar CO_2, 1 mbar H_2S, gas flow: 200 ml/min in modified ASTM seawater (no Ca^{2+}), low Fe^{2+} concentration due to the formation of iron sulfide layer, exposure time: 21 days.

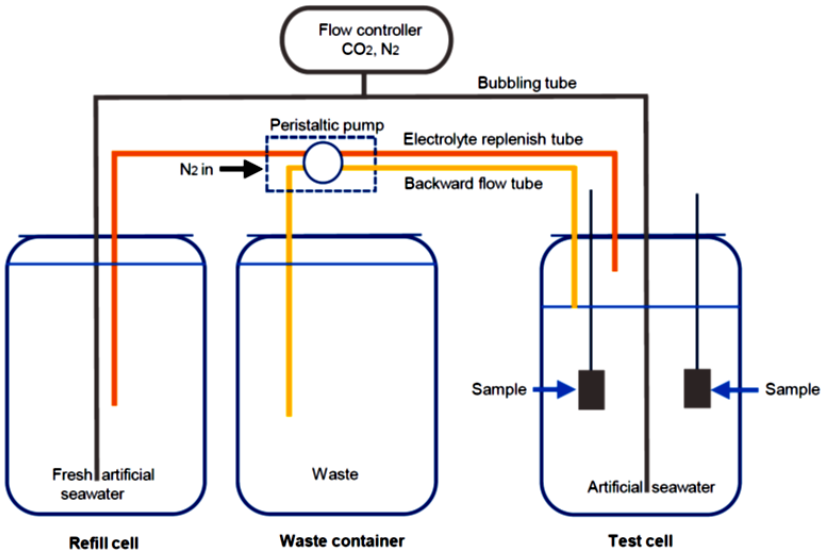

Figure 3.4. Schematic drawing of the corrosion test setup used for CO_2 exposure. The test cell is replenished by fresh artificial seawater in the CO_2 environment experiment, while in the CO_2/H_2S environment experiment the precipitation of FeS kept the concentration of the dissolved Fe^{2+} ions low, and therefore the test cell is not replenished by fresh artificial seawater [68].

3.3 Hydrogen uptake measurement

Hydrogen uptake measurements and analysis were done on high-carbon steels, i.e. CS62, CS65, and CS83. TDS was applied to measure the hydrogen uptake and analyze the interaction between the carbon steel microstructures and hydrogen after corrosion tests in CO_2, and CO_2/H_2S environments and after the electrochemical charging in 3.5% NaCl solution. The specimens were rinsed with isopropanol or ethanol and inserted in the liquid nitrogen as quickly as possible (took less than 1 minute) after being removed from the corrosion test cell or electrochemical charging cell to prevent the hydrogen egress from the samples. Besides, keeping the samples in liquid nitrogen gives this opportunity to start the TDS tests with a specimen at a lower temperature to minimize the hydrogen loss before the test onset. The hydrogen uptake analysis was performed using Bruker G4 PHOENIX DH machine. This apparatus consists of an ultra-high vacuum (UHV) measurement chamber equipped with a vacuum quartz furnace and a mass spectrometer. The infrared furnace allows the fast heating of the sample from room temperature up to 800 °C (Fig.3.5.). Two methods were used for hydrogen uptake analysis using Bruker G4 PHOENIX DH machine as follows:

- Hot extraction: The hot extraction method is based on the thermal activation of hydrogen atoms in the solid-state specimen and consecutive thermal desorption. In this method, the specimen is heated (via infrared radiation in G4 PHOENIX DH machine vacuum quartz furnace) and hydrogen is activated and desorbed out of the specimen. The desorbed hydrogen atoms are recombined to form hydrogen molecules. An inert gas (which is nitrogen in this study) is purged to the system continuously and acts as a gas flow to carry the desorbing hydrogen. The gas mixture is transferred to a mass spectrometer or a thermal conductivity detector (TCD) to measure the hydrogen content (in this study mass spectroscopy was used both in hot extraction and TDS analysis) [72]. In this study, the total hydrogen concentration of the studied high-carbon steel specimens was measured by Bruker G4 PHOENIX DH hot-extraction analyzer at 650 °C for 15 mins after hydrogen charging.

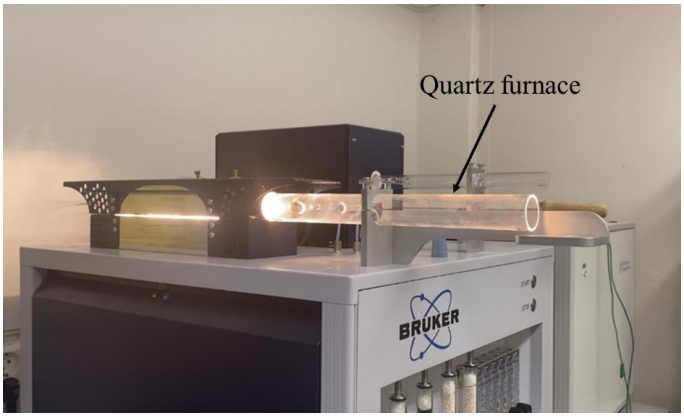

Figure 3.5. Bruker G4 PHOENIX DH.

- TDS: TDS provides an indirect assessment of the microstructural features that play a controlling role in the hydrogen diffusivity, solubility, and trapping in the studied steels [73]. TDS has the same fundamentals in the hydrogen measurement technique as the hot extraction method. In this method, a sample that is charged previously by hydrogen is continuously heated following a predefined linear temperature ramp profile while the amount of hydrogen gas desorbed from the material is recorded. The plot of the flow of the desorbed hydrogen gas as a function of temperature is a TDS spectrum. The TDS spectrum can be deconvoluted into several peaks, each one corresponding to specific hydrogen traps. The activation energy of hydrogen for each trap site can be get by

recording T_{max} and the used heating rate and by fitting the data. At least three heating rates should be selected to obtain a reliable fitting result [74], [75].

In this study, for the TDS analysis and the hydrogen desorption rate measurements, the temperature ramping program was used from 25 ℃ to 650 ℃ with various linear heating rates, i.e., 0.2, 0.3, and 0.5 $K \cdot s^{-1}$.

3.4 Corrosion layer characterization

The characteristics of the corrosion layer which is formed on the carbon steel surfaces during the corrosion process in CO_2 and CO_2/H_2S environment can affect the corrosion rate, hydrogen uptake, and hydrogen desorption of carbon steels. In this study, the role of cementite morphology on the corrosion rate and corrosion layer formation is investigated using SEM, FIB, EDS, and XPS.

3.4.1 SEM, EDS, and FIB characterization

To observe the morphology and thickness of the corrosion layers, the samples which were exposed to the CO_2 environment were embedded in DuroCit-3kit, an acrylic resin that is suitable to protect the formed corrosion layer on the carbon steel's surface. After the curing time, the embedded samples were cut and the cross-section of the embedded cut samples was grounded up to 4000 grit SiC abrasive paper and polished up to 1µm diamond suspensions. The thickness of the corrosion layer formed on the samples which were exposed to the CO_2/H_2S environment was less than 1µm and the embedding process could damage these layers. Therefore, FIB-SEM (Helios Nanolab DualBeam FIB, Thermo Fisher Inc., USA) was employed to characterize the cross-sections of the specimens exposed to the CO_2/H_2S environment. First, two platinum protection layers with thicknesses of 1 µm using an electron beam and 1.5 µm using an ion beam were applied on a selected area on the sample surfaces to protect the corrosion layer from potential damage by the ion beam. Then, the cross-sections of the corrosion layers were imaged.

3.4.2 XPS characterization

XPS is an effective and useful technique that can provide information regarding the elemental composition and chemical state of the corrosion layers [76]. The output of the XPS tests are spectra which are gained by irradiating the surface of a material with an X-ray beam and

measuring the kinetic energy and number of electrons that escape from the material. This technique delivers the information from a thin surface layer.

In this study, XPS was used to get the chemical composition information from the surface of the corrosion layers formed on the studied carbon steels exposed to the CO_2 and CO_2/H_2S environments. After the corrosion tests, the samples were taken out from the electrolyte and washed with isopropanol and deionized water, and transferred immediately to a desiccator. The XPS were performed using Kratos Axis Ultra DLD equipped with an Al Kα source. The sample analysis chamber pressure was 1×10^{-9} Torr (0.13 μPa) during the operation. First, the elemental maps were obtained with the pass energy of 160 eV with two sweeps. High-resolution regional acquisitions were performed with the pass energy of 20 eV with ten sweeps and 0.1 eV step size for each element. The analysis area was 300×700 μm^2, and five areas were analyzed for each sample. Argon sputtering with the energy of 4 V was used for 30 seconds to remove the surface contaminations before the start of the XPS analysis. The analysis started with the elemental map, then the high-resolution regional spectroscopy was carried out followed by 30 s argon sputtering. The obtained data were analyzed using Casa XPS software [77].

3.5 In situ electrochemical micro-cantilever bending (ECCB) test

3.5.1 Micro-cantilever fabrication

The micro-sized cantilevers with pentagonal cross-sections and a notch (with notch depth identical for all the micro-cantilevers), were fabricated using FEI Helios 600 DualBeam FIB microscope. The reason for using a notch was to increase the local stress in the notch root. A geometry was designed and tested to fulfill the research objectives. Micro-cantilevers were milled on the disk shape samples and the same design was used to mill the micro-cantilevers on two selected steels, CS62, and CS65, with high carbon content (Fig.3.6). The reason for choosing these two materials is that they have almost a similar chemical composition and they both have a ferrite-cementite microstructure. But the cementite morphology in material CS62 is spherical while in material CS65 is lamellar. Therefore, the comparison between these two materials would be helpful to understand the role of cementite morphology on crack initiation and growth in the presence of hydrogen.

3.5.2 In situ bending test

The micro-cantilever bending tests were performed using the Hysitron TI950 TriboIndenter system. This system is a depth-sensing nanomechanical test instrument that provides the possibility to perform quantitative nanomechanical testing. A miniaturized three-electrode cell

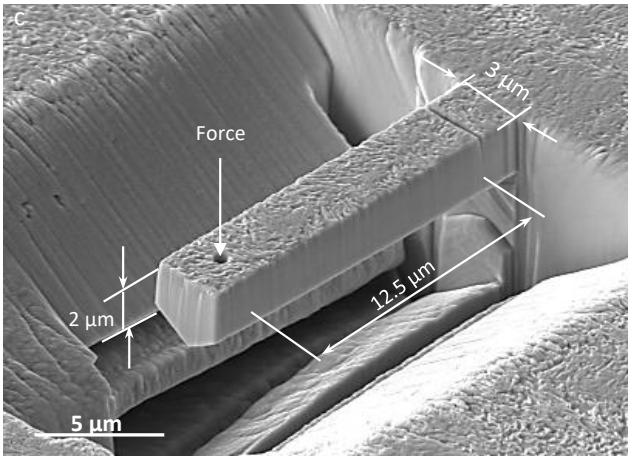

Figure 3.6. The micro-cantilever design used in this study.

was used for in situ charging of the microcantilevers as schematically shown in Fig.3.2. The electrochemical charging cell was installed in the Hysitron TI950 TriboIndenter chamber (Fig.3.7). The HE effect on mechanical properties was analyzed by the comparison experiments that the same set of cantilevers bent in two different environmental conditions, hydrogen-free, and hydrogen-charging conditions. The hydrogen charging process in the miniaturized cell was explained previously in section 3.2.1.

During the micro-cantilever bending test, the load (F) versus the displacement (Δ) is measured continuously. These data are converted into the common measuring units.

3.5.3 Post-mortem microstructure analysis

Micro-cantilevers bent in different environmental conditions were gently taken out of the cell, and washed with deionized water and ethanol. The bent micro-cantilevers were imaged by SEM. To have a clearer view of the crack growth path, the slice and view technique was performed on the bent micro-cantilever's notch area. In this technique, the cross-section of the micro-cantilever in the notch area is milled in FIB to get a view from the internal parts of the micro-cantilever and get a deeper view of the crack initiation and growth. In the first step of

the slice and view technique, the surface of the micro-cantilevers was covered by platinum to avoid damaging the surface during the cross-section ion milling process. The notch area was covered by an excess layer of platinum to be detectable (Fig.3.8). In the next step, the area near the cantilever root was milled to keep the notch area intact during the micro-cantilever milling process. The bent micro-cantilevers were transferred to a copper grid using a lift-out finger and then the cross-section of the notch area of the micro-cantilevers was milled from both sides with intervals of 100 nm followed by taking an SEM image. The final thickness was approximately 100 nm which was used for TEM characterization. The transferring procedure is shown in Fig.3.9.

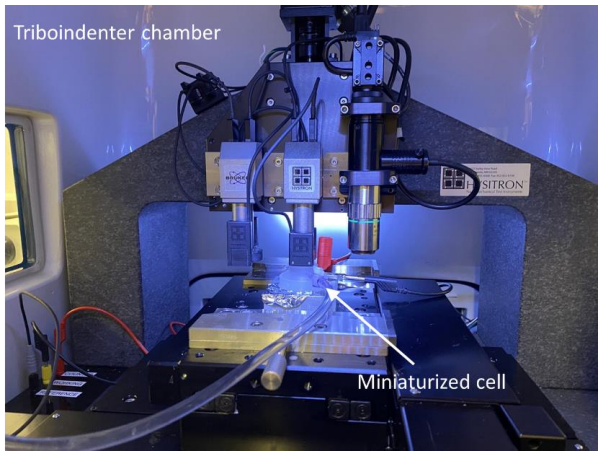

Figure 3.7. The three-electrode miniaturized cell installed in the Hysitron TI950 TriboIndenter chamber.

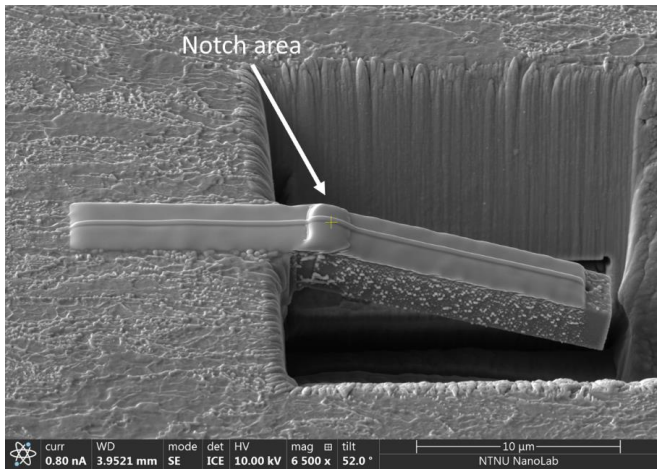

Figure 3.8. Platinum coating on a bent micro-cantilever. The notch area is covered by an excess layer of platinum.

3.5.4 Transmission electron microscopy (TEM)

TEM was performed by using a double spherical aberration corrected, cold field emission gun JEOL ARM 200FC, operated at 200 kV, on the prepared micro-cantilevers with 100 nm thickness. TEM was used to evaluate the cementite morphology role in crack initiation and propagation. TEM made it possible to follow the crack path through the lamellar cementite morphology in the pearlitic microstructure or the behavior of the crack around a cementite particle in the spheroidite microstructure. Electron energy loss spectroscopy (EELS) and scanning transmission electron microscopy (STEM) were performed simultaneously to get precise information about the microstructure phases.

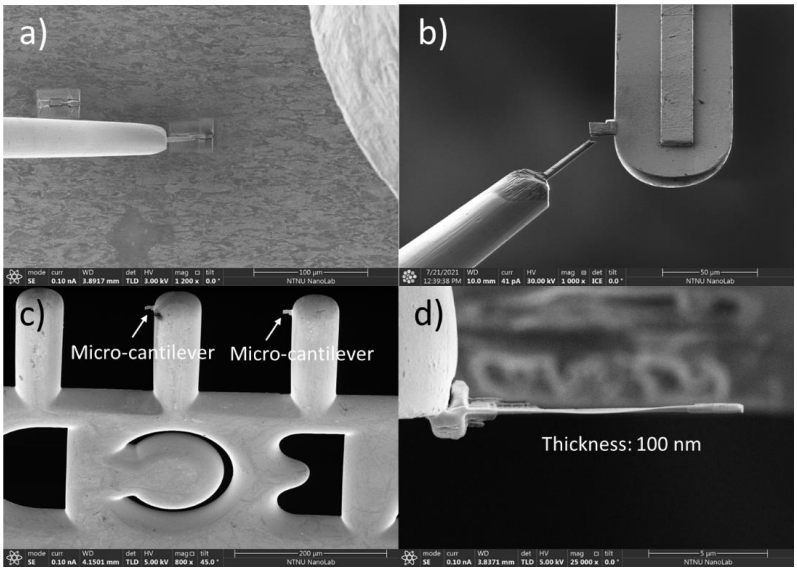

Figure 3.9. The procedure of lifting off the TEM sample with 100 nm thickness and transferring it to a copper grid. a) the omniprobe is attached to the cut micro-cantilever (TEM sample) by platinum deposition with a low current (0.44 nA), b) the TEM sample is placed and attached to a finger of the copper grid and it is detached from the omniprobe, c) overview of two TEM samples attached to the fingers of the copper grid, d) a close image of the attached micro-cantilever to a finger. The thickness of the TEM sample is 100 nm.

4. Summary of the journal papers

4.1 Paper 1

4.1.1 Introduction

Paper 1 with the title: " Evaluation of the cementite morphology influence on the hydrogen induced crack nucleation and propagation path in carbon steels" was published in the International Journal of Hydrogen Energy [78].

The main objective of paper 1 was to determine the cementite morphology role in the crack initiation and growth path in a ferrite-pearlite microstructure and in the presence of hydrogen. Consequently, the experimental procedure consisted of micro-cantilever fabrication using FIB and in situ ECCB tests. A miniaturized three-electrode electrochemical cell was incorporated into the nanoindenter to charge the micro-cantilevers with hydrogen and test them in situ. Two high-carbon steels with similar cementite phase fractions and different cementite morphologies (lamellar and spherical) were chosen for this study. The ECCB tests were performed in three environments, hydrogen-free, -1050 mV hydrogen charging, and -1550 mV hydrogen-charging (the potentials reported here are versus Ag/AgCl reference electrode). The postmortem analysis was done using SEM, FIB, and TEM to follow the crack path.

4.1.2 Main results and conclusions

The L-Δ curves from the ECCB tests displayed a higher strength and yield point in all environmental conditions for the pearlite microstructure. The spheroidite microstructure exhibits a load reduction with displacement increment in hydrogen-charging environments, while the load decreases continuously in all environments for the pearlite microstructure. However, it should be mentioned that for the pearlite microstructure, this decrease is small under both hydrogen-free and -1050 mV hydrogen charging and it's significant only under -1550 mV hydrogen charging.

In the first step of charging (-1050 mV), the pearlite microstructure showed more resistance to delamination in comparison with the spheroidite microstructure. Several small cracks appeared just in the middle of the width of the micro-cantilever where the material experience stress triaxiality. In the spheroidite microstructure, the ferrite-cementite delamination mechanism involves a higher volume of the material near the notch area and the initiated crack follows a tortuous path that passes around the cementite particles.

In the second step of charging (-1550 mV), by increasing the hydrogen concentration, the main crack is initiated from the notch tip and propagates transgranular through the micro-cantilever thickness in the spheroidite microstructure. In this case, the crack path is independent of the

grain boundaries or ferrite-cementite interfaces. In the pearlite microstructure, the lamellae cause the crack to transact the ferrite-cementite interfaces in a non-straightforward path. and in this way delayed the micro-cantilever fracture. In this microstructure, a competition between the crack growth with the shear mechanism and the interfacial cracking leads to a curved growth path through the thickness of the micro-cantilever. It can be concluded that in the pearlite microstructure, the lamellar morphology of the cementite phase delays the fracture of the micro-cantilever.

4.2 Paper 2

4.2.1 Introduction

Paper 2, with the title: " Role of cementite morphology on corrosion layer formation of high-strength carbon steels in sweet and sour environments", is published in the Corrosion Science journal and is included in the Appendix [68].

The main objective of this paper was to investigate the characteristics of the corrosion layers formed on four different carbon steels to reveal the role of microstructure and especially the cementite morphology on the corrosion layer formation in both CO_2 and CO_2/H_2S environments. The second objective of this study was to evaluate the role of corrosion layer characteristics in the corrosion behavior of the studied materials. In the second paper, we chose three high-carbon steels and one low-carbon steel. We focused on the high-carbon steels (which have higher than 0.6 w% carbon and are less investigated in the literature), and a low-carbon steel to be compared with the high-carbon steels. The high-carbon steel microstructures included ferrite-pearlite and spheroidite. These materials were exposed to CO_2 and CO_2/H_2S environments in an aqueous solution. The corrosion rate of the studied materials was measured using the LPR technique and weight loss measurements. The corrosion layer formed on the surface of the samples was characterized using SEM, EDS, FIB, and XPS.

4.2.2 Main results and conclusions

The LPR data and the weight loss measurements showed that the corrosion layer formed on all materials in the CO_2/H_2S environment provided significant protection in contrast to the layers formed in the CO_2 environment.

An increasing trend in corrosion rate with the cementite phase fraction increment was observed in the CO_2 environment. The FIB-SEM characterization of the corrosion layers revealed that in the CO_2 environment, the corrosion layer formed on high-carbon steels was thicker than the low-carbon steel. However, the protectivity of these layers was not sufficient to prevent their

high corrosion rates which were escalated by the micro-galvanic effect. The corrosion rate of the material with the ferrite-pearlite microstructure is higher than the material with the spheroidite microstructure, with a similar cementite phase fraction. Besides, the increment in the corrosion rate is higher for ferrite-pearlite microstructures because the micro-galvanic effect is more prominent in ferrite-pearlite microstructures than in the spheroidite microstructure. Moreover, the SEM-FIB results showed that the corrosion layer formed on the high-carbon ferrite-pearlite microstructure is quite porous, while the corrosion layer formed on the low-carbon steel was more closely-packed. In the present study, the Fe^{2+} concentration was kept low (less than 80 ppm) during the corrosion tests. In this condition, in pearlitic microstructures, the remaining cementite network gives rise to the formation of a porous corrosion layer. Since the Fe^{2+} concentration is low, Fe^{2+} and Fe^{3+} compounds (like $FeCO_3$, $Fe(OH)_2$, and Fe_2O_3) as the corrosion products do not cover the porosities in between the remaining cementite layers completely. Moreover, in a pearlitic microstructure with small interlamellar spacing, the acidity prevents the corrosion product precipitation. The ferrite-pearlite microstructure with larger ferrite areas has a non-uniform microstructure. In this microstructure, the crevice corrosion and breakdown of the layer lead to the formation of a rough and thinner corrosion layer. In the spheroidite microstructures, the uniform microstructure causes the formation of a porous layer with lower porosity than the corrosion layers in ferrite-pearlite microstructures. The low-carbon steel showed a more compact corrosion layer and less corrosion rate.

In the CO_2/H_2S environment, no special trend was observed in the corrosion rate based on the cementite phase fraction of the studied materials. The presence of H_2S induced a significant reduction in the corrosion rate in comparison with the CO_2 environment. A substantial reduction in the corrosion layer thickness was also observed in the materials exposed to the H_2S environment compared with the samples in the CO_2 environment. However, the layers showed high protectivity, and unlike the CO_2 environment, the thickness of the layers matters. The higher the layer thickness, the more protection is reached. In the CO_2/H_2S environment, after the maximum protectiveness was reached, the corrosion rate of the studied low-carbon steel stabilized, while there was a slight increase in the corrosion rate of the high-carbon steels with both the spheroidite microstructure and the ferrite-pearlite microstructure. The XPS results showed the presence of FeS, FeS_2, and also Fe^{2+} and Fe^{3+} compounds in all the formed layers regardless of their microstructures in the CO_2/H_2S environment. It was found from the XPS results that with increasing the cementite phase fraction, particularly in ferrite-pearlite

microstructures, the proportion of the Fe^{2+} compound decreased, while the proportion of the Fe^{3+} compound increased.

The delicate differences between the studied materials in the role of cementite morphology on the corrosion layer formation and the consequent effect of the corrosion layer on the corrosion rate are discussed in the paper. A mechanism that explains the role of cementite morphology on corrosion layer formation in the CO_2 environment is proposed for the studied materials.

4.3 Paper 3

4.3.1 Introduction

Paper 3 with the title:" Evaluation of microstructural and environmental effects on the hydrogen uptake and desorption in high-strength carbon steels: a thermal desorption spectroscopy study", is published in the Corrosion Science journal.

The main objective of this paper was to analyze the role of the environment, cementite morphology, and corrosion layers on hydrogen uptake and hydrogen desorption. Hydrogen thermal desorption and hot extraction analysis were performed on three high-strength carbon steels with different cementite morphology and microstructure. These materials were charged in three different environments. They were exposed to modified artificial seawater bubbled once with CO_2 and in another test with CO_2/H_2S at open circuit potential for 21 days. The same materials were also charged cathodically in a 3.5% NaCl solution containing 1 g/l thiourea. All tests were done at room temperature.

The role of the environment on hydrogen uptake was discussed by comparing the hydrogen uptake measurements in different environments for each material. The deconvolution of the TDS spectrum and the calculation of the activation energies for each TDS spectrum peak were used to discuss the role of the microstructure on hydrogen absorption for each material. For analyzing the corrosion layer effect on hydrogen desorption, the corrosion layer that was formed on the surface of the samples in the CO_2 and CO_2/H_2S environment was characterized using FEB-SEM. The corrosion layer effect on hydrogen effusion was discussed based on the TDS spectrum and the corrosion layer characterization.

4.3.2 Main results and conclusions

The hot extraction results revealed that the hydrogen uptake in all the materials showed a higher value in the CO_2/H_2S environment compared with the results in the CO_2 environment. The hydrogen uptake was higher for all the materials which were charged cathodically to their saturation in comparison with the materials exposed to the actual CO_2 and CO_2/H_2S

environments. The hydrogen uptake increased with the cementite phase fraction increment. Materials with ferrite-pearlite microstructures have a significantly higher capability of hydrogen uptake in all charging conditions. Besides, the ferrite-pearlite microstructures showed higher temperature peaks which were not observable in the spheroidite microstructure. The ferrite-pearlite or pearlite-pearlite interfaces act as strong irreversible traps in pearlitic microstructures.

In the CO_2 environment, the hydrogen uptake and the hydrogen desorption were affected by the corrosion layer formed on the steel. In this condition, hydrogen is desorbed with a delay because hydrogen passed through a tortuous corrosion layer containing remaining Fe_3C partially filled with corrosion products that can trap the hydrogen and release it with a delay.

In the CO_2/H_2S environment and cathodic hydrogen charging condition, the tortuosity in the ferrite-pearlite microstructure delays the hydrogen desorption from the traps. This leads to hydrogen desorption continuing at higher temperatures. The thin corrosion layer formed in the CO_2/H_2S environment does not affect the hydrogen desorption rate while based on our previous article it retards the corrosion rate.

5. Conclusions and future works

5.1 Conclusions

This work mainly investigated the effect of cementite morphology on corrosion behavior, hydrogen uptake, and hydrogen embrittlement of armor wire carbon steels. The experiments were performed on four types of carbon steels with different microstructures which are used as armor wires in flexible pipes.

The following conclusions are from the study of the role of cementite morphology on the hydrogen-induced crack nucleation and propagation path using the ECCB method:

- In spheroidite microstructure and under the lower hydrogen concentration, the ferrite-cementite interface delamination mechanism involves a higher volume of the material near the notch area.
- The pearlitic microstructure showed more resistance to delamination and several small cracks appeared just in the area where the material experience stress triaxiality.
- In the spheroidite microstructure, by increasing the hydrogen concentration, the crack initiates from the notch tip and propagates transgranulary through the sample thickness.
- The pearlitic microstructure, by increasing the hydrogen concentration, depicted a competition between the crack growth with the shear mechanism and the interfacial

cracking which leads to a curved growth path through the thickness of the micro-cantilever.

- In pearlitic microstructure, the shear mechanism activates, and the lamellas cause the crack to transact the ferrite-cementite interfaces in a non-straightforward path and in this way delay the fracture of the sample.

The following conclusions are from the investigation of the role of cementite morphology on corrosion behavior and corrosion layer formation of high-strength carbon steels in CO_2 and CO_2/H_2S environments:

- The corrosion layer formed on all microstructures in the CO_2/H_2S environment provided significant protection, in contrast to the layer formed in the CO_2 environment.
- With increasing carbon content and cementite phase fraction, the corrosion rate increased in the CO_2 environment while no special trend was observed in the CO_2/H_2S environment.
- The corrosion rate of the material with ferritic/pearlitic microstructure was higher than the material spheroidite microstructure owing to the more prominent micro-galvanic effect in lamellar microstructures.
- In the CO_2/H_2S environment, the corrosion rate of the low-carbon steel stabilized is the maximum protectiveness is reached.
- For materials with high carbon content and spheroidite or pearlite microstructures, the corrosion rate showed a slight increase until the end of the experiment. The pearlite microstructure with the connected ferrite phase showed the highest corrosion rate increase.
- It was found from XPS results that by increasing the carbon content, particularly in ferritic/pearlitic microstructures, the proportions of Fe^{2+} compounds decreased and the proportions of the Fe^{3+}-related compounds increased.

The following conclusions are from the investigation of the microstructure and environmental effects on hydrogen uptake and desorption using TDS:

- The hydrogen uptake in all studied materials shows a higher value in the CO_2/H_2S environment compared with the results in the pure CO_2 environment.
- The hydrogen uptake is higher for all materials which are charged cathodically to their saturation in comparison with the materials exposed to CO_2 and CO_2/H_2S environments under the actual exposure conditions.

- The hydrogen uptake in the material with the lamellar cementite morphology is significantly higher than the material with the spherical cementite morphology with almost similar carbon content, in the CO_2/H_2S environment, and cathodic hydrogen charging condition.
- In the CO_2 environment, the hydrogen uptake and the hydrogen desorption are affected by the corrosion layer formed on the steel. In this condition, hydrogen desorbs with a delay because hydrogen passes through a tortuous corrosion layer containing remaining Fe_3C partially filled with corrosion products that can trap hydrogen and release it with a delay.
- The pearlite/ferrite and pearlite/pearlite interfaces act as strong irreversible traps in pearlitic microstructures.
- In the CO_2/H_2S environment and cathodic hydrogen charging condition, the tortuosity in the lamellar pearlitic microstructures delays the hydrogen desorption from the traps. This leads to hydrogen desorption continuing at higher temperatures.
- The thin corrosion layer formed in the CO_2/H_2S environment does not affect the hydrogen desorption rate while based on our previous study it retards the corrosion rate.

5.2 Future works

To sum up, the present PhD work comprehensively studied the role of the microstructure and particularly the cementite morphology of different carbon steels with ferrite-pearlite and spheroidite microstructures on the corrosion layer formation, corrosion rate, hydrogen uptake, HE susceptibility, and crack growth path. In this thises novel in situ ECCB and the corrosion tests in the presence of CO_2 and CO_2/H_2S in the environment, TDS, hot extraction, and different measurement techniques were used. SEM, EDS, FIB, XPS, and TEM were used as sample preparation or postmortem analysis tools.

Due to time and technical limitations, some works could not be performed and realized in the present PhD study. Some of the outlooks and future works are listed as follows:

- Grain boundaries are one of the most vulnerable sites for HE. Therefore further studies focusing on the grain boundary behavior need to be done. This can be achieved by performing the Electron back scattered diffraction technique (EBSD) to investigate the distribution of the high-angle and low-angle grain boundaries in different microstructures. This data could be useful in TDS data analysis. Besides, different grain boundaries can be marked using micro-indenter and EBSD, and then the selected grain

boundaries can be tested with the ECCB method to investigate the interaction of different grain boundaries and their effects on the mechanical properties and HE.
The effect of the presence of cementite in the grain boundary can be also investigated by performing the ECCB test on two different micro-cantilevers which both have the same angle, one with cementite and the other without.

- The ECCB method can be used to study the effect of the interlamellar spacing in the pearlitic microstructures on the crack initiation and growth and also on the mechanical degradation in the presence of hydrogen.
  Moreover, milling the micro-cantilevers with different notch orientations in the pearlitic microstructures can be helpful to study the preferential crack growth path when the notch (the stress concentration) is parallel or perpendicular to the cementite lamellae.

- Among the different factors that affect the CO_2 or CO_2/H_2S environments aggressiveness, temperature plays a mutual role. In a corrosion process, an increase in the temperature elevates the corrosion rate, at the same time it might play a catalytic role in the corrosion layer formation [80]. Therefore, the effect of the temperature on the corrosion layer formation and the consequent effect on the corrosion rate in CO_2 or CO_2/H_2S environments for the studied material needs to be investigated in further studies.

- Aggressive environments (i.e., high CO_2 and/or H_2S contents) with high pressures and high temperatures are conditions to be faced by steels used in pipelines. The temperature in subsea pipelines can be higher than 100 °C [80]. The corrosion layer which is formed on the steel surface at high temperature is different from the layer formed at room temperature. The effect of the corrosion layer which is formed on high temperature in CO_2 and CO_2/H_2S environments on hydrogen uptake needs to be studies in future works.

References

[1] X. Li, X. Ma, J. Zhang, E. Akiyama, Y. Wang, and X. Song, "Review of hydrogen embrittlement in metals: hydrogen diffusion, hydrogen characterization, hydrogen embrittlement mechanism and prevention," *Acta Metall. Sin. English Lett.*, vol. 33, no. 6, pp. 759–773, 2020, doi: 10.1007/s40195-020-01039-7.

[2] S. Lynch, "Hydrogen embrittlement phenomena and mechanisms," *Corros. Rev.*, vol. 30, no. 3–4, pp. 105–123, 2012, doi: 10.1515/corrrev-2012-0502.

[3] X. Li and M. A. Vaz, "Analytical estimation on the number of bending cycles to initiate armour wires lateral buckling in flexible pipes," *Ocean Eng.*, vol. 228, no. September 2020, p. 108838, 2021, doi: 10.1016/j.oceaneng.2021.108838.

[4] E. S. Skilbred, S. Palencsár, A. Dugstad, and R. Johnsen, "Hydrogen uptake during active CO2-H2S corrosion of carbon steel wires in simulated annulus fluid," *Corros. Sci.*, vol. 199, no. February, 2022, doi: 10.1016/j.corsci.2022.110172.

[5] A. Dugstad, S. Palencsár, T. Berntsen, and L. Børvik, "Corrosion of steel armour wires in flexible pipes - history effects," *Soc. Pet. Eng. - SPE Int. Oilf. Corros. Conf. Exhib. 2018*, no. June, pp. 18–19, 2018, doi: 10.2118/190907-ms.

[6] M. G. Marinho, D.R. Pipa, C.S. Camerini, G.P. Pires, A.B. Moreira, S.R. Morikawa, J.M. Santos, "New techniques for integrity management of flexible riser-end fitting connection," *Proc. Int. Conf. Offshore Mech. Arct. Eng. - OMAE*, vol. 3, pp. 643–648, 2008, doi: 10.1115/OMAE2008-57929.

[7] N. Desamais and C. Taravel-Condat, "On the beneficial influence of a very low supply of H_2S on the hydrogen embrittlement resistance of carbon steel wires in flexible pipe annulus," In *Offshore Technology Conference*. OnePetro, 2009, doi: 10.4043/otc-19950-ms.

[8] Z. F. Yin, W. Z. Zhao, Z. Q. Bai, Y. R. Feng, and W. J. Zhou, "Corrosion behavior of SM 80SS tube steel in stimulant solution containing H_2S and CO_2," *Electrochimica Acta* 53, vol. 53, no. 10, pp. 3690–3700, 2008, doi: 10.1016/j.electacta.2007.12.039.

[9] S. Zhang *et al.*, "Understanding the synergistic effect of CO_2, H_2S and fluid flow towards carbon steel corrosion," *Vacuum*, vol. 196, no. October 2021, p. 110790, 2022, doi: 10.1016/j.vacuum.2021.110790.

[10] G. A. Zhang, Y. Zeng, X. P. Guo, F. Jiang, D. Y. Shi, and Z. Y. Chen, "Electrochemical corrosion behavior of carbon steel under dynamic high pressure H_2S/CO_2 environment," *Corros. Sci.*, vol. 65, pp. 37–47, 2012, doi: 10.1016/j.corsci.2012.08.007.

[11] T. das Chagas Almeida, M. C. E. Bandeira, R. M. Moreira, and O. R. Mattos, "New insights on the role of CO2 in the mechanism of carbon steel corrosion," *Corros. Sci.*, vol. 120, pp. 239–250, 2017, doi: 10.1016/j.corsci.2017.02.016.

[12] R. Safi, R. K. Agarwal, and S. Banerjee, "Numerical simulation and optimization of CO_2 utilization for enhanced oil recovery from depleted reservoirs," *Chem. Eng. Sci.*, vol. 144, pp. 30–38, 2016, doi: 10.1016/j.ces.2016.01.021.

[13] T. Tran, B. Brown, S. Nesic, "Corrosion of mild steel in an aqueous CO_2 environment – basic electrochemical mechanisms revisited," *NACE - Int. Corros. Conf.*, OnePetro, no. 5671, pp. 1–11, 2015.

[14] B. R. Linter and G. T. Burstein, "Reactions of pipeline steels in carbon dioxide solutions," *Corros. Sci.*, vol. 41, no. 1, pp. 117–139, 1999, doi: 10.1016/S0010-938X(98)00104-8.

[15] S. Nesic, J. Postlethwaite, and S. Olsen, "An Electrochemical model for prediction of corrosion of mild steel in aqueous carbon dioxide solutions," *Corros.*, vol. 52, no. 4, pp. 280–294, 1996, doi: 10.5006/1.3293640.

[16] M. B. Kermani and A. Morshed, "Critical review of corrosion science and engineering carbon dioxide corrosion in oil and gas production-a compendium," *Corrosion* 59, vol. 59, no. 8, pp. 659–683, 2003.

[17] E. Remita, B. Tribollet, E. Sutter, V. Vivier, F. Ropital, and J. Kittel, "Hydrogen evolution in aqueous solutions containing dissolved CO_2: Quantitative contribution of the buffering effect," *Corros. Sci.*, vol. 50, no. 5, pp. 1433–1440, 2008, doi: 10.1016/j.corsci.2007.12.007.

[18] S. N. Esmaeely, G. Bota, B. Brown, and S. Nešić, "Influence of pyrrhotite on the corrosion of mild steel," *Corrosion*, vol. 74, no. 1, pp. 37–49, 2018, doi: 10.5006/2505.

[19] C. De Waard, and D. E. Milliams, "Carbonic Acid Corrosion of Steel.," *Corrosion*, vol. 31, no. 5. pp. 177–181, 1975, doi: 10.5006/0010-9312-31.5.177.

[20] S. Nesic, "Effects of multiphase flow on internal CO_2 corrosion of mild steel pipelines," *Energy and Fuels*, vol. 26, no. 7, pp. 4098–4111, 2012, doi: 10.1021/ef3002795.

[21] S. Nešić, "Key issues related to modelling of internal corrosion of oil and gas pipelines -a review," Corros.Sci., vol.49, no.12, pp.4308-4338, 2007, doi: 10.1016/j.corsci.2007.06.006.

[22] S. Nešić, M. Nordsveen, R. Nyborg, and A. Stangeland, "A mechanistic model for carbon dioxide corrosion of mild steel in the presence of protective iron carbonate films - part 2: a numerical experiment," *Corrosion*, vol. 59, no. 6, pp. 489–497, 2003, doi:

10.5006/1.3277579.

[23] S. Nešić, J. Han, B. N. Brown, and D. Young, “Mesh-capped probe design for direct pH measurements at an actively corroding metal surface,” *J. Appl. Electrochem.*, vol. 40, no. 3, pp. 683–690, 2010, doi: 10.1007/s10800-009-0043-8.

[24] R. Barker *et al.*, “Iron carbonate formation kinetics onto corroding and pre-filmed carbon steel surfaces in carbon dioxide corrosion environments,” *Appl. Surf. Sci.*, vol. 469, no. March 2018, pp. 135–145, 2019, doi: 10.1016/j.apsusc.2018.10.238.

[25] H. Karimi Abadeh and M. Javidi, “Assessment and influence of temperature, NaCl and H_2S on CO_2 corrosion behavior of different microstructures of API 5L X52 carbon steel in aqueous environments,” *J. Nat. Gas Sci. Eng.*, vol. 67, no. April, pp. 93–107, 2019, doi: 10.1016/j.jngse.2019.04.023.

[26] W. Sun, S. Nesic, “A mechanistic model of H_2S corrosion of mild steel,” *NACE - Int. Corros. Conf.*, OnePetro, no. 07655, pp. 1–26, 2007.

[27] K. J. Lee, S. Nesic, “The effect of trace amount of H_2S on CO_2 corrosion investigated by using the EIS technique,” *NACE - Int. Corros. Conf.*, OnePetro, no. 05630, pp. 1–16, 2005.

[28] R. Eustaquio-Rincón, M. E. Rebolledo-Libreros, A. Trejo, and R. Molnar, “Corrosion in aqueous solution of two alkanolamines with CO_2 and H_2S: N-methyldiethanolamine + diethanolamine at 393 K,” *Ind. Eng. Chem. Res.*, vol. 47, no. 14, pp. 4726–4735, 2008, doi: 10.1021/ie071557r.

[29] P. W. Bolmer, “Polarization of iron in H_2S-NaHS buffers,” *Corrosion*, vol. 21, no. 3. pp. 69–75, 1965, doi: 10.5006/0010-9312-21.3.69.

[30] J. Kittel, F. Ropital, F. Grosjean, E. M. M. Sutter, and B. Tribollet, “Corrosion mechanisms in aqueous solutions containing dissolved H_2S. part 1: characterisation of H_2S reduction on a 316L rotating disc electrode,” *Corros. Sci.*, vol. 66, pp. 324–329, 2013, doi: 10.1016/j.corsci.2012.09.036.

[31] A. Kahyarian and S. Nesic, “H_2S corrosion of mild steel: a quantitative analysis of the mechanism of the cathodic reaction,” *Electrochim. Acta*, vol. 297, pp. 676–684, 2019, doi: 10.1016/j.electacta.2018.12.029.

[32] R. Barker, Y. Hua, and A. Neville, “Internal corrosion of carbon steel pipelines for dense-phase CO_2 transport in carbon capture and storage (CCS) – a review,” *Int. Mater. Rev.*, vol. 62, no. 1, pp. 1–31, 2017, doi: 10.1080/09506608.2016.1176306.

[33] D. W. Shoesmith, P. Taylor, M. G. Bailey, and D. G. Owen, “The formation of ferrous monosulfide polymorphs during the corrosion of iron by aqueous hydrogen sulfide at

21°C," *J. Electrochem. Soc.*, vol. 127, no. 5, pp. 1007–1015, 1980, doi: 10.1149/1.2129808.

[34] S. Nesic, H. Li, J. Huang, and D. Sormaz, "An open source mechanistic model for CO_2/H_2S corrosion of carbon steel," In *Corrosion*. OnePetro, no. 09572, pp. 1–19, 2009.

[35] S. Wang, L. Wang, X.Liu, M. Bao, L.Liu, X. Wang, C. Ren, "Influence of CO_2 and H_2S concentration on hydrogen permeation behavior of P110 steel," *Int. J. Electrochem. Sci.*, vol. 12, no. 11, pp. 10317–10337, 2017, doi: 10.20964/2017.11.29.

[36] W.Y. Chu, S.Q. Li, C.M. Haiao, and J.Z. Tien, " Mechanism of stress corrosion cracking of steels in H_2S, " Corrosion 36, no.9 (1980): 475-482.

[37] B. A. Szost, R. H. Vegter, and P. E. J. Rivera-Díaz-Del-Castillo, "Hydrogen-trapping mechanisms in nanostructured steels," *Metall. Mater. Trans. A Phys. Metall. Mater. Sci.*, vol. 44, no. 10, pp. 4542–4550, 2013, doi: 10.1007/s11661-013-1795-7.

[38] K. G. Solheim, J. K. Solberg, J. Walmsley, F. Rosenqvist, and T. H. Bjørnå, "The role of retained austenite in hydrogen embrittlement of supermartensitic stainless steel," *Eng. Fail. Anal.*, vol. 34, no. 4035, pp. 140–149, 2013, doi: 10.1016/j.engfailanal.2013.07.025.

[39] S. Papavinasam, "The main environmental factors influencing corrosion," *Corrosion Control in the Oil and Gas Industry* (2014): 179-247.

[40] E. Wallaert, T. Depover, I. De Graeve, and K. Verbeken, "FeS corrosion products formation and hydrogen uptake in a sour environment for quenched & tempered steel," *Metals (Basel).*, vol. 8, no. 1, 2018, doi: 10.3390/met8010062.

[41] S. Zheng, C. Zhou, P. Wang, C. Chen, and L. Chen, "Effects of the temperature on the hydrogen permeation behaviours of l360ncs pipeline steel in 1 MPa H_2S environments," *Int. J. Electrochem. Sci.*, vol. 8, no. 2, pp. 2880–2891, 2013.

[42] F. Huang, P. Cheng, X. Y. Zhao, J. Liu, Q. Hu, and Y. F. Cheng, "Effect of sulfide films formed on X65 steel surface on hydrogen permeation in H_2S environments," *Int. J. Hydrogen Energy*, vol. 42, no. 7, pp. 4561–4570, 2017, doi: 10.1016/j.ijhydene.2016.10.130.

[43] M. Monnot, R.P. Nogueira, V. Roche, G. Berthome, E. Chauveau, R. Estevez, M. Mantel, "Sulfide stress corrosion study of a super martensitic stainless steel in H_2S sour environments: metallic sulfides formation and hydrogen embrittlement," *Appl. Surf. Sci.*, vol. 394, pp. 132–141, 2017, doi: 10.1016/j.apsusc.2016.10.072.

[44] C. D. Beachem, "A new model for hydrogen-assisted cracking (hydrogen 'embrittlement')," *Metall. Trans.*, vol. 3, no. 2, pp. 441–455, 1972, doi:

10.1007/BF02642048.

[45] A. R. Troiano, “The Role of hydrogen and other interstitials in the mechanical behavior of metals: (1959 Edward De Mille Campbell Memorial Lecture),” *Metallogr. Microstruct. Anal.*, vol. 5, no. 6, pp. 557–569, 2016, doi: 10.1007/s13632-016-0319-4.

[46] M. Hatano, M. Fujinami, K. Arai, H. Fujii, and M. Nagumo, “Hydrogen embrittlement of austenitic stainless steels revealed by deformation microstructures and strain-induced creation of vacancies,” *Acta Mater.*, vol. 67, pp. 342–353, 2014, doi: 10.1016/j.actamat.2013.12.039.

[47] Z. Wang, X. Shi, X. S. Yang, W. He, S. Q. Shi, and X. Ma, “Atomistic simulation of the effect of the dissolution and adsorption of hydrogen atoms on the fracture of α-Fe single crystal under tensile load,” *Int. J. Hydrogen Energy*, vol. 46, no. 1, pp. 1347–1361, 2021, doi: 10.1016/j.ijhydene.2020.09.216.

[48] R. Kirchheim, “Revisiting hydrogen embrittlement models and hydrogen-induced homogeneous nucleation of dislocations,” *Scr. Mater.*, vol. 62, no. 2, pp. 67–70, 2010, doi: 10.1016/j.scriptamat.2009.09.037.

[49] M. Nagumo, “Hydrogen related failure of steels - a new aspect,” *Mater. Sci. Technol.*, vol. 20, no. 8, pp. 940–950, 2004, doi: 10.1179/026708304225019687.

[50] R. Kirchheim, “On the solute-defect interaction in the framework of a defactant concept,” *International journal of materials research* 100, no. 4 (2009): 483-487.

[51] M. Deutges, I. Knorr, C. Borchers, C. A. Volkert, and R. Kirchheim, “Influence of hydrogen on the deformation morphology of vanadium (100) micropillars in the α-phase of the vanadium-hydrogen system,” *Scr. Mater.*, vol. 68, no. 1, pp. 71–74, 2013, doi: 10.1016/j.scriptamat.2012.09.020.

[52] C. Plennevaux, J. Kittel, M. Fregonese, B. Normand, F. Ropital, T. Cassagne, “Contribution of CO_2 on hydrogen evolution and hydrogen permeation in low alloy steels exposed to H_2S environment,” *Electrochem. commun.*, vol. 26, no. 1, pp. 17–20, 2013, doi: 10.1016/j.elecom.2012.10.010.

[53] M. T. Ma, K. J. Li, Y. Si, P. J. Cao, H. Z. Lu, A. M. Guo, G. D. Wang, “Hydrogen embrittlement of advanced high-strength steel for automobile application: a review,” *Acta Metall. Sin. (English Lett.*, no. 0123456789, 2023, doi: 10.1007/s40195-022-01517-0.

[54] W. H. Johnson, “II. On some remarkable changes produced in iron and steel by the action of hydrogen and acids,” *Proceedings of the Royal Society of London* 23, no. 156-163 (1875): 168-179, doi: 10.1098/rspl.1874.0024.

[55] T. Doshida and K. Takai, “Dependence of hydrogen-induced lattice defects and hydrogen embrittlement of cold-drawn pearlitic steels on hydrogen trap state, temperature, strain rate and hydrogen content,” *Acta Mater.*, vol. 79, pp. 93–107, 2014, doi: 10.1016/j.actamat.2014.07.008.

[56] D. Clover, B. Kinsella, B. Pejcic, and R. De Marco, “The influence of microstructure on the corrosion rate of various carbon steels,” *J. Appl. Electrochem.*, vol. 35, no. 2, pp. 139–149, 2005, doi: 10.1007/s10800-004-6207-7.

[57] S. C. da Silva, E. A. de Souza, F. Pessu, Y. Hua, R. Barker, A, Neville, J. A. da Gunha Ponciano Gomes, “Cracking mechanism in API 5L X65 steel in a CO_2 -saturated environment,” *Eng. Fail. Anal.*, vol. 99, no. February, pp. 273–291, 2019, doi: 10.1016/j.engfailanal.2019.02.031.

[58] M. Ueda, and H. Takabe, “Effect of Environmental Factor and Microstructure on morphology of corrosion products in CO_2 environments,” *NACE - Int. Corros. Conf.* OnePetro, 1999.

[59] M. Di Bonaventura, B. Brown, S. Nešić, and M. Singer, “Effect of flow and steel microstructure on the formation of iron carbonate,” *Corrosion*, vol. 75, no. 10, pp. 1183–1193, 2019, doi: 10.5006/3118.

[60] W. H. Schreiner and S. R. De Sa, “The influence of carbon steel microstructure on corrosion layers An XPS and SEM characterization,” *Applied surface science* vol. 207, no. 1-4 (2003): 69-85..

[61] A. Dugstad, H. Hemmer, and M. Seiersten, “Effect of steel microstructure upon corrosion rate and protective iron carbonate film formation,” *NACE - Int. Corros. Conf. Ser.*, vol. 2000-March, no. 4, 2000.

[62] S. Al-Hassan, B. Mishra, D. L. Olson, and M. M. Salama, “Effect of microstructure on corrosion of steels in aqueous solutions containing carbon dioxide,” *Corrosion*, vol. 54, no. 6, pp. 480–491, 1998, doi: 10.5006/1.3284876.

[63] C. A. Palacios and J. R. Shadley, “Characteristics of corrosion scales on steels in a CO_2-saturated NaCl brine,” *Corrosion*, vol. 47, no. 2, pp. 122–127, 1991, doi: 10.5006/1.3585227.

[64] H. W. Pickering, “A review of the mechanism and kinetics of electrochemical hydrogen entry and degradiation of metallic systems,” *College Earth and Mineral Sciences,* no. a216671, 1990.

[65] A. W. Thompson, and I. M. Bernstein, “The Role of metallurgical variables in hydrogen-assisted environmental fracture,” *Adv. Corros. Sci. Technol.*, pp. 53–175, 1980, doi:

10.1007/978-1-4615-9065-1_2.

[66] E. S. Skilbred, M. Kappes, M. Iannuzzi, and R. Johnsen, “Hydrogen uptake and diffusivity in steel armor wires with different chemical composition, carbide distribution, grain size, and degree of deformation,” *Mater. Corros.*, vol. 73, no. 3, pp. 326–345, 2022, doi: 10.1002/maco.202112615.

[67] S. L. I. Chan, “Hydrogen trapping ability of steels with different microstructures,” *J. Chinese Inst. Eng. Trans. Chinese Inst. Eng. A/Chung-kuo K. Ch’eng Hsuch K’an*, vol. 22, no. 1, pp. 43–53, 1999, doi: 10.1080/02533839.1999.9670440.

[68] S. Karimi, I. Taji, T. Hajilou, S. Palencsar, A. Dugstad, A. Barnoush, K. Verbeken, T. Depover, and R. Johnsen, “Role of cementite morphology on corrosion layer formation of high-strength carbon steels in sweet and sour environments,” *Corros. Sci.*, vol. 214, no. February, p. 111031, 2023, doi: 10.1016/j.corsci.2023.111031.

[69] M. Kappes, G. S. Frankel, R. Thodla, M. Mueller, N. Sridhar, and R. M. Carranza, “Hydrogen permeation and corrosion fatigue crack growth rates of X65 pipeline steel exposed to acid brines containing thiosulfate or hydrogen sulfide,” *Corrosion*, vol. 68, no. 11, pp. 1015–1028, 2012, doi: 10.5006/0636.

[70] L. Claeys, T. Depover, I. De Graeve, and K. Verbeken, “Electrochemical hydrogen charging of duplex stainless steel,” *Corrosion*, vol. 75, no. 8, pp. 880–887, 2019, doi: 10.5006/2959.

[71] S. N. Esmaeely, Y. S. Choi, D. Young, and S. Nešić, “Effect of calcium on the formation and protectiveness of an iron carbonate layer in CO_2 corrosion,” *Mater. Perform.*, vol. 53, no. 5, pp. 54–59, 2014.

[72] M. Rhode, T. Schaupp, C. Muenster, T. Mente, T. Boellinghaus, and T. Kannengiesser, “Hydrogen determination in welded specimens by carrier gas hot extraction — a review on the main parameters and their effects on hydrogen measurement,” pp. 511–526, 2019.

[73] E. Malitckii, E. Fangnon, and P. Vilaça, “Evaluation of steels susceptibility to hydrogen embrittlement: a thermal desorption spectroscopy-based approach coupled with artificial neural network,” *Materials (Basel).*, vol. 13, no. 23, pp. 1–14, 2020, doi: 10.3390/ma13235500.

[74] F. J. Castro and G. Meyer, “Thermal desorption spectroscopy (TDS) method for hydrogen desorption characterization (I): Theoretical aspects,” *J. Alloys Compd.*, vol. 330–332, pp. 59–63, 2002, doi: 10.1016/S0925-8388(01)01625-5.

[75] F. Von Zeppelin, M. Haluška, and M. Hirscher, “Thermal desorption spectroscopy as a quantitative tool to determine the hydrogen content in solids,” *Thermochim. Acta*, vol.

404, no. 1–2, pp. 251–258, 2003, doi: 10.1016/S0040-6031(03)00183-7.

[76] R. Gašparac, C. R. Martin, E. Stupnišek-Lisac, and Z. Mandic, “In Situ and Ex Situ Studies of Imidazole and Its Derivatives as Copper Corrosion Inhibitors. II. AC Impedance, XPS, and SIMS Studies,” *J. Electrochem. Soc.*, vol. 147, no. 3, p. 991, 2000, doi: 10.1149/1.1393302.

[77] CASA XPS, "Casa XPS," 2022. [Online]. Available: CASA XPS software. [Accessed 13 march 2023], http://www.casaxps.com/.

[78] S. Karimi, I. Taji, T. Hajilou, A. Barnoush, and R. Johnsen, “Evaluation of the cementite morphology influence on the hydrogen induced crack nucleation and propagation path in carbon steels,” *Int. J. Hydrogen Energy*, vol. 47, no. 30, pp. 14121–14129, 2022, doi: 10.1016/j.ijhydene.2022.01.222.

[79] R. C. Souza *et al.*, “The role of temperature and H_2S (thiosulfate) on the corrosion products of API X65 carbon steel exposed to sweet environment,” *J. Pet. Sci. Eng.*, vol. 180, no. April, pp. 78–88, 2019, doi: 10.1016/j.petrol.2019.05.036.

[80] N. Taylor and A. Ben Gan, “Submarine pipeline buckling-imperfection studies,” *Thin-Walled Struct.*, vol. 4, no. 4, pp. 295–323, 1986, doi: 10.1016/0263-8231(86)90035-2.

Part II

Paper I

Shabnam Karimi, Iman Taji, Tarlan Hajilou, Afrooz Barnoush, Roy Johnsen

Evaluation of the cementite morphology influence on the hydrogen induced crack nucleation and propagation path in carbon steels

International journal of hydrogen energy (2022)
https://doi.org/10.1016/j.ijhydene.2022.01.222

INTERNATIONAL JOURNAL OF HYDROGEN ENERGY 47 (2022) 14121–14129

Available online at www.sciencedirect.com

ScienceDirect

journal homepage: www.elsevier.com/locate/he

Evaluation of the cementite morphology influence on the hydrogen induced crack nucleation and propagation path in carbon steels

Shabnam Karimi [a,*], *Iman Taji* [a], *Tarlan Hajilou* [a], *Afrooz Barnoush* [a,b], *Roy Johnsen* [a]

[a] *Department of Mechanical and Industrial Engineering, Norwegian University of Science and Technology, No. 7491 Trondheim, Norway*

[b] *Qatar Environment and Energy Research Institute, P.O. Box 34110, Doha, Qatar*

HIGHLIGHTS

- Cementite morphology's role on the hydrogen induced crack growth path is studied.
- In low H fugacity, cementite-ferrite interface failed in spheroidite microstructure.
- In pearlite microstructure few H-induced interface cracks formed, In low H fugacity.
- In high H fugacity, crack grows regardless of the interfaces in S microstructure.
- Interfacial cracking and shear mechanisms lead the crack in P microstructure.

ARTICLE INFO

Article history:
Received 8 November 2021
Received in revised form
27 January 2022
Accepted 28 January 2022
Available online 19 March 2022

Keywords:
Hydrogen embrittlement
Carbon steels
Cementite
Spheroidite
Pearlite
Micro-cantilever

ABSTRACT

The effect of cementite morphology on the crack initiation and growth path was studied using in situ electrochem-ical micro-cantilever bending (ECCB) technique under hydrogen (H) charging. Two carbon steels with lamellar cementite morphology (pearlitic micro-structure) and spherical or broken lamellas cementite morphology (spheroidite micro-structure), both with approximately the same carbon equivalent, were used in this study. The ECCB tests were performed in H-free and two H charging steps with −1050 mV and −1550 mV charging potential versus Ag/AgCl reference electrode. The results show that both materials are resistant to crack initiation in the H-free condition while under −1050 mV charging, crack propagates through the grain boundaries in a tortuous path in spheroidite mi-crostructure and the lamellar microstructure displayed a higher strength with small cracks propagating through both the grain boundaries and the lamellas. A drastic load decrease in the load-displacement (L-D) curve happened under −1550 mV charging for both microstructures accompanied by a straight crack growth path in spheroidite microstruc-ture, independent of grain boundaries or ferrite-cementite in-terfaces while a competition between the shear crack growth mechanism and the inter-facial cracking determines the crack growth path in the lamellar microstructure.

* *Corresponding author.*
E-mail address: Shabnam.karimi@ntnu.no (S. Karimi).

https://doi.org/10.1016/j.ijhydene.2022.01.222

Introduction

The mechanical properties of carbon steels are dependent on the different combinations of microstructures and can alter significantly, covering a broad range of strength, toughness, and ductility. Cementite is one of the key phases in carbon steels which has an important function in the mechanical properties [1]. Lamella and spheroidite are examples of two cementite morphologies in ferrite matrix with high strength and drawability for the former [2] and developed ductility and fracture resistance for the latter [3].

The increasing use of carbon steels in offshore and subsea applications necessitates more investigation on the sustainability of their mechanical properties especially due to their exposure to the environments resulting in detrimental effects of hydrogen (H) absorption. The microstructural changes are considered as a way to modify the H interaction with the weak sites like the ferrite-cementite interfaces or grain boundaries [4,5]. The microstructure dependency of hydrogen embrittlement (HE) has been a subject of numerous studies [6–10]. It has been shown that the size of the cementite particles and the interlamellar spacing in a pearlitic microstructure [11–13] could affect the HE. In addition, the orientation of the lamellas versus loading axis can play an important role [14]. The grain boundaries (GB) and pearlite-pearlite boundaries are other affecting parameters [15]. Furthermore, changes in the cementite morphology do significantly alter the diffusivity, permeability, and solubility of H [16,17] which in turn can affect the crack nucleation and the fracture mechanism [12,18–22].

Since there is a complicated correlation between the microstructure and the fracture mechanism in the presence of H, it is required to minimize the influential factors. One of the ways to do so is to miniaturize the test sample and perform micro-mechanical testing. In situ electrochemical micro-cantilever bending test (ECCB) proved to be a successful method to investigate the H-microstructural interactions [23]. In this study effects of the microstructure on the fracture behaviour during the in situ H charging for both lamellar and spheroidite cementite morphologies will be studied using ECCB.

Materials and methods

The studied materials were two types of carbon steels (CS62 and CS65) which are tensile armour wires of the flexible pipes used in oil and gas industry. The chemical compositions provided in Table 1 received in the form of drawn curved strips with the width of 10 mm and the thickness of 3 mm. The equivalent carbon content (CE) in the table was calculated using the American Welding Society formula [24]. In the present study, since the chemical composition of the studied materials are close and similar, the role of alloying elements on the HE is ignored. These materials show a ferrite-cementite microstructure. The morphology of the cementite in material CS62 is the spherical particles or broken lamellas in ferrite matrix while thick lamellas of cementite in a ferrite matrix constitute the microstructure in material CS65 as shown in Fig. 1(a and b). The SEM micrographs of material CS65 were processed using ImageJ and the interlamellar spacing determined by the intercept method is 242 ± 64 nm. Cementite particles are also precipitated in the ferrite-ferrite grain boundaries in material CS62 and ferrite-pearlite or pearlite-pearlite interfaces in material CS65.

To mill the micro-cantilevers, the surface of the specimens was first ground to 4000 grit SiC papers followed by mechanically polished with 3 μm and 1 μm diamond suspensions and finally etched in 2% nital solution. The etching depth differentiation between ferrite and cementite was under 100 nm for both materials. The purpose of etching was to make the microstructural features on the surface visible and locate each micro-cantilever inside the pearlite colonies. Micro-cantilevers were milled by a focused ion beam (Helios Dual Beam FIB, FEI) on the rolling surface of the two studied materials, parallel to the elongation direction of the strips to the dimensions presented in Fig. 1(c). Sharp V-shape notches of almost 700 nm depth with an open angle of ~10°, were milled 1.5 μm away from the cantilever beam root.

The micro-cantilever bending tests were carried out in both H-free and in situ electrochemical H charged conditions using the Hysitron TI950 TriboIndenter system. The H-free tests were used as references. The bending process was performed in displacement control mode with a displacement rate of 2 nm/s using a long shaft conical tip with the nominal tip radius of 500 nm. An integrated miniaturized three-electrode electrochemical cell with a platinum counter electrode was the H generator in H-charged tests. $Hg/HgSO_4$ reference electrode was used to avoid the surface attack which can be made by chloride ions. The potentials were converted and reported versus Ag/AgCl in this paper. Detailed information about the used miniaturized cell is described in Ref. [25]. The micro-cantilevers were potentiostatically charged at −1050 mV and −1550 mV versus Ag/AgCl. The corresponding steady-state current density of CS62 sample was 100 μA/cm^2 and 650 μA/cm^2 and for CS65 sample was 135 μA/cm^2 and 945 μA/cm^2, for −1050 mV and −1550 mV, respectively.

To avoid any local corrosion on the surface of the samples during charging, a glycerol-based solution with the composition of 1.3 Molar borax in glycerol was chosen as the H-charging electrolyte [26]. 1 g/l Thiourea dissolved in 20% distilled water was added to the electrolyte as a poison to increase the efficiency of H absorption [27].

The specimens were pre-charged at least for 165 minutes and all the micro-cantilever were bent up to 5 μm displacement. After bending, to investigate the crack propagation path

Table 1 – Chemical composition of the studied materials.

wt%	C	Al	Si	P	Mo	V	Cr	Mn	Ni	Cu	CE
CS62	0.62	0.26	0.40	0.23	0.46	0.70	0.61	1.36	0.89	0.75	1.37
CS65	0.65	0.30	0.24	0.20	0.35	0.51	0.51	0.96	0.60	0.75	1.21

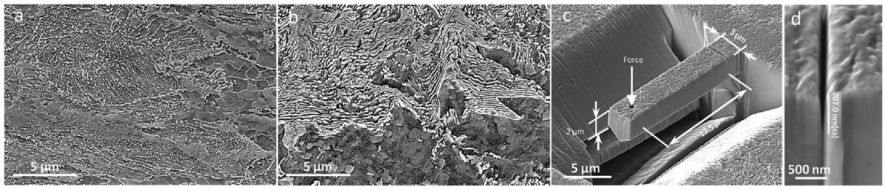

Fig. 1 – SEM images of the longitudinal cross section of the drawn wires used for the micro-bending tests. a) CS62 and b) CS65 c) a FIB milled micro-cantilever before bending d) and the side view of a micro-cantilever at the crack region before bending.

under the notch root, the cross-sections normal to the cantilever directions were milled and sliced by FIB and then observed with SEM. Prior to this process, the notch area was covered by a platinum-carbon layer using FIB deposition to prevent any damage to the crack by the gallium ion beam. After each slicing step which was 100 nm in thickness, an SEM image of the cross-section was taken to follow the crack propagation path. Finally, transmission electron microscopy (TEM) lamella of −1550 mV charged micro-cantilevers were prepared by FIB using a Helios G4 UX dual-beam instrument from FEI. The final thickness of the TEM lamella was around 100 nm. TEM was performed with a double spherical aberration corrected, cold field emission gun JEOL ARM 200FC, operated at 200 kV. This instrument is equipped with a 100 mm^2 Centurio silicon drift detector, covering a GIF Quantum ER for electron energy loss spectroscopy (EELS). EELS and STEM were performed simultaneously in scanning transmission electron microscopy (STEM) mode.

Results and discussion

Fig. 2(a and b) shows the representative (L-D) curves of CS62 and CS65 micro-cantilevers bending tests, respectively. The micro-cantilevers were bent under three different environmental conditions, i.e. in H-free and H-charging potential of −1050 mV and −1550 mV for both materials. The elastic parts of the micro-cantilevers obey a normal linear trend and they are almost similar to each other in different environments except for some small deviations which might be originated from the trivial discrepancy in micro-cantilevers geometrical dimensions.

Material CS65 micro-cantilevers exhibit more strength and higher yield points in all environmental conditions in comparison with material CS62 which is related to the lamellar microstructure of this material with small interlamellar spacing [28].

In material CS62 under the H-free environment, the load is almost steady with the increase in the displacement until 3.8 μm and from this point, there is an increment in the load which can be related to the contact of the micro-cantilever with the redeposited material beneath the beam support. The micro-cantilever on material CS65 which was bent in the H-free environment condition shows a slight decrease in the load with the increase in the displacement until the end of the bending experiment. In material CS62, a continuous decrease of bending load is observed in both −1050 mV and −1550 mV charging conditions, while in material CS65 this decrease

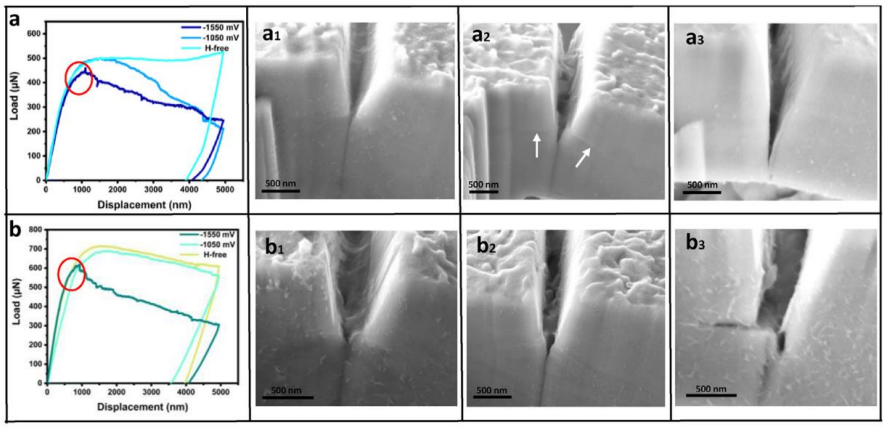

Fig. 2 – Load-displacement relations recorded during the micro-bending tests in H-free and under potentiostatic hydrogen charging in −1050 mV and −1550 mV of a) material CS62 and b) material CS65 $a_1 - a_3$) and $b_1 - b_3$) SEM images from the side view of each of the microcantilevers at the crack region bent under H-free, −1050 mV and −1550 mV conditions respectively.

occurs only under −1550 mV charging condition and no significant decrease was observed for the micro-cantilever charged at −1050 mV compared to H-free condition.

From L-D curves in Fig. 2(a and b), it is deduced that for both materials charged at −1550 mV potential, the crack is initiated before the materials enter the fully plastic deformation region. The increase in H content, is well-known, to reduce the threshold stress intensity factor (K) [29] and lead to crack initiation in lower loads. Decreasing the K factor also leads to the smaller plastic zone ahead of the crack [30,31] which is visible with a very short deviation of the curves from the initial elastic slop in L-D curves of the −1550 mV potential charged cantilevers which are shown inside the red circles in the figure. The maximum force difference between −1550 mV charging and H-free conditions are also worth noticing. For CS62 and CS65 samples, this difference is around 50 μN and 100 μN, respectively. Since the lamellar morphology provides a large number of interfaces which are favorable for hydrogen trapping [32], the higher difference in material CS65 can be originated from the influence of H in this material [33,34].

It is important to mention that the L-D curves of H charged micro-cantilevers for material CS62 in Fig. 2(a) exhibit different slopes in the flow load decreasing segment. Micro-cantilever charged with less negative potential (−1050 mV) displays a sharper gradient. The stress intensity ahead of the notch is dependent on the tolerated force and the geometrical shape of the notch [35]. At the early stages of the plastic deformation, the tolerated load for micro-cantilever bent under −1050 mV charging condition is higher than the micro-cantilever bent in −1550 mV charging condition. Therefore, this micro-cantilever experienced more stress intensity factor ahead of the notch, assuming that both micro-cantilevers have similar notch geometries. As a result, the amount of corresponding surfaces which are opened due to the fracture process is higher under −1050 mV charging condition and bigger volume of the material around the notch area get involved in the fracture process. This phenomenon will be shown and discussed later in Fig. 3.

The post-deformation SEM images of the micro-cantilevers in different environmental testing conditions are shown in Fig. 2 $a_1 - a_3$ and $b_1 - b_3$ for materials CS62 and CS65, respectively. In material CS62, the micro-cantilever tested in H-free condition shows a notch opening with an incremented angle of 14° and only notch blunting was observed without any crack formation in the root of the notch.

For material CS65, in H-free condition, the notch opening angle is incremented by 29° which is larger than material CS62. In addition, a continuous and gradual decrease in the load up to the final displacement for material CS65 compared to the steady flow load for sample CS62 in H-free condition is a confirmation of the crack tip opening angle difference in the tested materials. The load adjustment can be a contribution of two counteracting effects [31]. The eminent plasticity happening at the notch tip leads to strain hardening and blunting, which contributes to increasing the load at the L-D curves. At the same time, the notch opening and propagation result in the reduction of the beam cross-section which in turn leads to the load decrease. The latter phenomena were more prominent in material CS65 causing a decreasing load flow and higher incremented opening angle and material CS62 shows a load plateau due to these opposing effects.

For CS62 micro-cantilever bent under the −1050 mV charging, the notch opened with the same incremented angle as H-free condition (Fig. 2 a_2). As it is visible in this figure there are some micro-voids/cracks which are formed within the notch root. However, in −1550 mV charging condition a relatively sharp crack is propagated throughout the thickness of the cantilever (Fig. 2 a_3). Furthermore in −1050 mV tested sample two visible steps are formed on the micro-cantilever side which are shown by white arrows, while no step nor any slip lines could be distinguished in SEM images of the micro-cantilever bent under −1550 mV charging condition. In the micro-cantilever which was tested in H-free condition the dislocations generated at the notch tip can spread through the material and move away continuously and shield the plasticity [36]. Therefore, the slip lines do not accumulate near the crack tip to form a step on the surface. When H is presented, the slip steps were observed under −1050 mV charging condition. H reduces the formation energy of dislocations near the crack tip and leads to a higher dislocation nucleation and multiplication rate [37,38]. On the other hand, the localized H atoms promotes the slip planarity which causes slip localization and additional slip bands [39,40]. In −1050 mV charging condition, however, the H concentration is not high enough to lock the dislocation movements and weaken the cohesive bond strength sufficiently to form a sharp crack like what happens in micro-cantilever charged under −1550 mV charging condition. With higher H absorption (−1550 mV), the dislocation nucleation enhances at the notch tip but at the same time H atoms segregates to the dislocations and cause enormous interactions between the dislocations and dislocations with H at the notch tip and therefore the dislocations mobility is reduced by H-induced pinning effect [31,41] and leads to a sharp crack growth through the micro-cantilever thickness.

The flow curves in Fig. 2(b) for material CS65 shows that the mechanical response of micro-cantilever bent in −1050 mV charging condition follows the same behaviour as H-free condition. However there are some differences between the post-deformation SEM images of these two micro-cantilevers. Under −1050 mV charging condition a crack developed in the notch root with a sharp tip and the initial notch blunting leaves a mouth opening angle of approximately 23° which is slightly smaller than the one in the H-free condition. Increasing the H-charging potential to −1550 mV caused a significant change in cracking behaviour. The cracks propagate in two different directions and an immense decline in the mechanical properties of the micro-cantilever is observed.

In Fig. 3, the SEM images of the cantilevers cross-section are shown. Each image was taken after a cross-section slicing step and four images of each micro-cantilever are presented. The microstructural difference of CS62 and CS65 can be seen in this figure, a lamellar pearlite morphology for material CS65 and a granular or drawn granular morphology for material CS62 which is in good agreement with the SEM images of the surface microstructures presented in Fig. 1(a and b). Material CS62 with the broken lamella or particles of cementite is considered as spheroidite [42] and a lamellar cementite-ferrite constitutes the pearlitic microstructure of

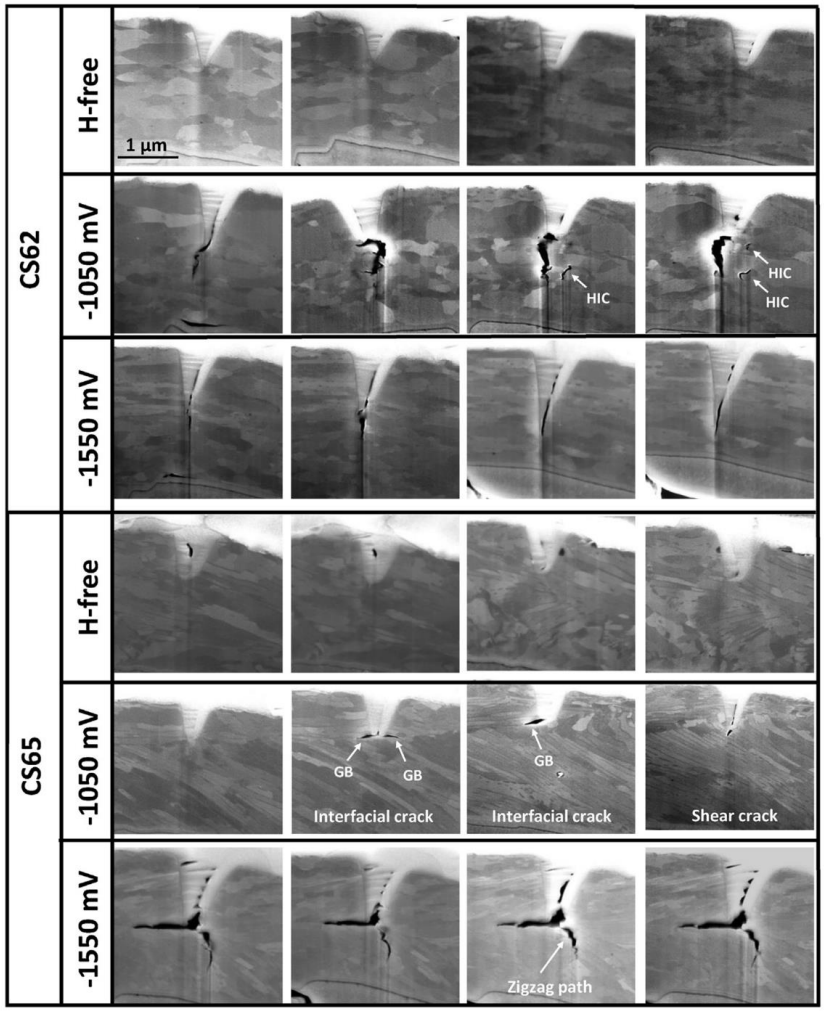

Fig. 3 – Representative SEM images of the cross-sections of each micro-cantilever after bending.

material CS65. Different gray colors of grains in material CS62, Fig. 3, represent the ferrite grains and the spheroidite cementite particles are smaller in size and distributed over the ferrite matrix. The particles with the green color in the EELS chemical composition map of material CS62 display the cementite phase (Fig. 4a_2). In material CS65, on the other hand, the cementite phase is visible as the narrow green lamellas which separate the elongated ferrite parts (Fig. 4b_2). It should be noted that the green color which is visible inside the crack is due to the platinum-carbon deposition which was done to cover and protect the notch area before slicing the micro-cantilever.

In H-free condition, no crack initiation is observed in the notch root for both materials, and as is discussed before, only the notch opening and blunting happened during the bending process. H is well-known to cause reduction in binding energy between the atoms and cohesive strength of the interfaces (HEDE mechanism) [43]. Therefore the presence of H in the microstructure can accelerate crack formation. In carbon steels containing cementite phase, H is likely to precipitate in interfacial boundaries, like GBs and ferrite-cementite interfaces [29,44–47]. Cementites themselves could be deep trap sites for H [48]. However, the first principal studies showed that at least in low fugacities, the activation energy of H is not high enough to enter the cementite phase [49]. Besides, the cementite-ferrite interfaces are the most probable segregation sites for H. Their study showed that even for low bulk concentrations of H, the concentration of H at the interface can be close to saturation. Therefore it is expected that the initiation and propagation of the cracks under the H charging take place in interfaces where the H is accumulated [50]. This is the case for −1050 mV charging condition. The cross-sectional images

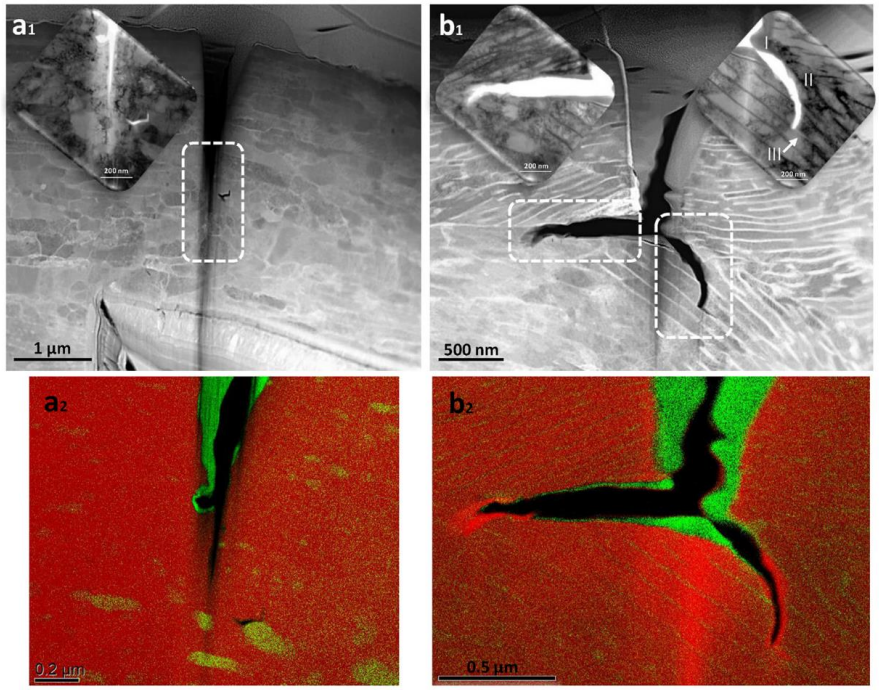

Fig. 4 – a_1 and b_1) TEM images of the crack region from the micro-cantilevers bent under −1550 mV in material CS62 and CS65 respectively. a_2 and b_2) EELS chemical composition maps of the crack region from the micro-cantilevers bent under −1550 mV in material CS62 and CS65 respectively (The green color which is visible inside the crack is due to the platinum-carbon deposition which was done to cover and protect the notch area before slicing the micro-cantilever.). (For interpretation of the references to colour in this figure legend, the reader is referred to the Web version of this article.)

show that the propagation of the crack follows the interfaces for CS62 micro-cantilevers bent under the −1050 mV charging condition as shown in Fig. 3. The crack initiated from the notch root which bears a high stress intensity and propagates towards the perpendicular direction to the tensile axis in a tortuous intergranular path. There are some H induced cracks (HIC) that are formed within the bulk of the micro-cantilever shown by arrows in the figure. These micro-cracks are also formed at the GBs.

In the CS65 sample bent under −1050 mV charging condition, the crack is propagated through the GBs which is parallel to the tensile axis [20]. It should be noted that from the results of the L-D curves and subsequent post-deformation SEM micrographs in Fig. 2, the presence of these cracks was not distinguishable. However, by slicing the micro-cantilever and going forward through, intergranular cracks appeared which is related to the stress triaxiality in the center of the micro-cantilever width. The material experiences a high degree of stress triaxiality in a restrictive plane strain condition in the center of the micro-cantilever width, while plane stress condition exists on the edges [31]. It is interesting to see that the formed crack is propagated horizontally while the stress constraints dictate the crack to grow vertically down to the notch root. The presence of longitudinal cracking along the tensile axis is also observed by Enos and Scully [14] who studied high-strength carbon steels. They demonstrated that extremely weak interfaces could be a path of crack propagation, even though they may not be aligned favorably to the high normal stress direction.

The elongated pearlite lamellas are reported to prevent the crack propagation if they are aligned perpendicularly to the cracking direction [11]. However, it is also reported that cracks can be initiated within the pearlite lamellas by shear mechanism [42,51]. This kind of crack formation is depicted in Fig. 3 (CS65, −1050 mV) labeled by shear crack but this crack which is formed by shear mechanism cannot propagate furthermore and is blocked by the pearlite lamellas while the crack which is formed at the GB, had the opportunity to propagate without any hindrance. As can be seen from Fig. 3 (CS65, −1050 mV) the GBs which exist on the two sides of the notch root, were suitable paths for crack propagation while in the next SEM image the crack did not grow on the right-hand side of the notch root because there is not any interface there and besides, the pearlite lamellas in this side are perpendicular to the probable crack growth direction. Therefore the crack just moved in the left-hand side through the GB. By comparing the cross-sectional SEM images of two materials bent under −1050 mV charging condition it can be deduced that a larger volume of the micro-cantilever in material CS62 involves in crack formation than in material

CS65. This is in line with the L-D curve results where the load drop in material CS62 is significantly obvious and for material CS65 just a trivial difference between the load flow in H-free and in −1050 mV charging can be seen. In fact, in material CS62 under −1050 mV charging condition, the H concentration at the crack tip is not sufficient to cause the main crack to continue transgranularly through the micro-cantilever thickness. Therefore, the combination of the high stress field and H accumulation in the weak sites near the notch tip, like grain boundaries, lead to the formation of micro-cracks in the area around the notch which are not connected to the notch and the main crack and a higher volume of the material involved in the crack growth process (Figs. 2 and 3) which in turn causes the decreasing trend observed in the load-displacement curve in material CS62. While in material CS65, micro-cracks formed mainly in the pearlite colonies interfaces which are connected to the notch (3). These cracks formed in the middle of the micro-cantilever width where material experiences triaxiality stress and with further slicing towards the micro-cantilever edges, they disappear. In fact, under −1050 mV charging condition in material CS65, the lamellas prevent the crack to propagate, and the load-displacement curve does not show a significant drop in comparison with H-free condition curve. But by increasing the H charging potential to −1550 mV the crack intersects the lamellas and grow through the lamellar microstructure. It can be inferred that under the studied test conditions and in low H concentration (−1050 mV), the cementite lamellar morphology in CS65 microstructure is more resistant to HE compared with spherical morphology in material CS62.

In the second stage of charging with increasing the potential to −1550 mV, material CS62 represents a straight crack propagation path unlike the behaviour seen in the micro-cantilever bent under −1050 mV charging condition. Increasing the fugacity of H favors the crack propagation transgranularly. In other words, the H role dominates the microstructure effects and the crack grows without targeting the GBs and ferrite-cementite interfaces. This crack is finally stopped when it reaches a cementite particle which is located in the crack propagation path (Fig. 4a_2).

But in material CS65, the lamellar microstructure affects the fracture paths. Cracking occurred and spread in two distinct directions. One crack grows through the GB as discussed before and the other one propagates through a zigzag path and crosses the ferrite-cementite lamellas Fig. 3 (CS65, −1550 mV). Based on the TEM characterization which is shown in the high magnification inset in Fig. 4b_1, the latter crack path can be divided into three stages. In stage I, the crack starts propagating from the notch root towards the GB. However, due to the tensile load which forces the crack to propagate perpendicular to the tensile axis, it deviates from the GB path and crossed the pearlite lamellas following the shear mechanism phenomena [51]. Others have also shown that H promotes shearing mechanism, especially by facilitating void formation from sheared steps [14,20]. Ogawa et al. introduce this type of crack propagation as the pearlite-tearing when the crack propagation transects the ferrite-cementite lamellas aligned almost perpendicular to the crack plane [11]. At the last stage when the load is not high enough to induce shear cracking, the crack finds its way through the cementite-ferrite interface which is already a prone path for delamination due to H induces interface decohesion. This mechanism in a pearlitic microstructure which is known as pearlite-delamination is considered as a negative and detrimental aspect of pearlite in comparison with the positive impact of pearlite-tearing which function as barriers and arrest the crack propagation [11].

From the above-mentioned two crack propagation path, it can be deduced that the GBs and the interfaces between the pearlite colonies are the highly sensitive sites in the presence of H and they provide a favorable path for crack propagation. Besides, the ferrite-cementite interface is the other sensitive and weak site in Pearlitic microstructures and the crack continue to propagate towards these interfaces especially in the presence of high H fugacity and when stress is not high enough to lead the crack growth path at the end of the test as it is shown in both Fig. 4b_1 and Fig. 3 (CS65, −1550 mV). However, by increasing the effect of either H or the load, the shear mechanism is more probable to take place.

Summary

In summary, to investigate the microstructure effect on the H assisted cracking and fracture, micro-cantilevers with sharp notches were fabricated on two carbon steels with different microstructures (spheroidite (CS62) and pearlite (CS65)) by FIB, and in-situ electrochemical micro-cantilever bending tests were conducted in H-free and during the two steps cathodic H charging (−1050 mV and −1550 mV). The load reduction by the indenter displacement in material CS62 occurred under both −1050 mV and −1550 mV charging. In material CS65, a slight load decrease in H-free and −1050 mV charging conditions occurred, and a large reduction was observed under −1550 mV charging. In spheroidite microstructure (CS62) and under the lower H concentration (−1050 mV), the ferrite-cementite interface delamination mechanism involves a higher volume of the material near the notch area while the pearlitic microstructure (CS65) showed more resistance to delamination and several small cracks appeared just in the middle of the width of the micro-cantilever where the material experience stress triaxiality. By increasing the H concentration (−1550 mV), the crack initiates from the notch tip and propagates transgranulary through the micro-cantilever thickness in the spheroidite microstructure while the pearlitic microstructure depicted a competition between the crack growth with the shear mechanism and the interfacial cracking which leads to a curved growth path through the thickness of the micro-cantilever. In this microstructure the shear mechanism activates, and the lamellas cause the crack to transact the ferrite-cementite interfaces in a non-straightforward path and in this way delay the fracture of the micro-cantilever.

Data availability statement

The raw and processed data required to reproduce these findings cannot be shared at this moment due to technical and time limitations.

Declaration of competing interest

The authors declare that they have no known competing financial interests or personal relationships that could have appeared to influence the work reported in this paper.

Acknowledgment

Per Erik Vullum from the Department of Physics, NTNU, is gratefully acknowledged for contributing the TEM images.

The Research Council of Norway is also acknowledged for the support to the Norwegian Micro- and Nano-Fabrication Facility, NorFab, project number 295 864.

The authors would like to thank the sponsors of the KFC-I project (Kjeller Flexible Cracking project-I) for technical and financial support and for permission to publish results: 4Subsea, Baker Hughes, Chevron, Equinor, NOV, OKEA, Petrobras, Shell, TechnipFMC and the Research Council of Norway (PETROMAKS 2 programme, project no. 280 760).

REFERENCES

[1] Umemoto M, Todaka Y, Tsuchiya K. Mechanical properties of cementite and fabrication of artificial pearlite. Mater Sci Forum 2003;426:859–64.
[2] Xu Y, Umemoto M, Tsuchiya K. Comparison of the characteristics of nanocrystalline ferrite in fe-0.89 c steels with pearlite and spheroidite structure produced by ball milling. Mater Trans 2002;43(9):2205–12.
[3] Toribio J, González B, Matos J-C. Influence of the microstructure of eutectoid steel on the cyclic crack propagation: pearlite and spheroidite. Int J Fract 2011;171(2):209–15.
[4] Sun Y, Fujii H. Improved resistance to hydrogen embrittlement of friction stir welded high carbon steel plates. Int J Hydrogen Energy 2015;40(25):8219–29.
[5] Ohaeri E, Eduok U, Szpunar J. Hydrogen related degradation in pipeline steel: a review. Int J Hydrogen Energy 2018;43(31):14584–617.
[6] Egels G, Fussik R, Weber S, Theisen W. On the role of nitrogen on hydrogen environment embrittlement of high-interstitial austenitic crmnc (n) steels. Int J Hydrogen Energy 2019;44(60):32323–31.
[7] Egels G, Roncery LM, Fussik R, Theisen W, Weber S. Impact of chemical inhomogeneities on local material properties and hydrogen environment embrittlement in aisi 304l steels. Int J Hydrogen Energy 2018;43(10):5206–16.
[8] Skjellerudsveen M, Akselsen OM, Olden V, Johnsen R, Smirnova A. Effect of microstructure and temperature on hydrogen diffusion and trapping in x70 grade pipeline steel and its weldments. 2010.
[9] Shvachko V. Cold cracking of structural steel weldments as reversible hydrogen embrittlement effect. Int J Hydrogen Energy 2000;25(5):473–80.
[10] Saeki Y, Yamada Y, Ishikawa K. Relationship between hydrogen permeation and microstructure in nb–tini two-phase alloys. Int J Hydrogen Energy 2014;39(23):12024–30.
[11] Ogawa Y, Nishida H, Nakamura M, Olden V, Vinogradov A, Matsunaga H. Dual roles of pearlite microstructure to interfere/facilitate gaseous hydrogen-assisted fatigue crack growth in plain carbon steels. Int J Fatig 2021:106561.
[12] Loureiro RdCP, Beres M, Masoumi M, de Abreu HFG. The effect of pearlite morphology and crystallographic texture on environmentally assisted cracking failure. Eng Fail Anal 2021;126:105450.
[13] Hui W, Xu Z, Zhang Y, Zhao X, Shao C, Weng Y. Hydrogen embrittlement behavior of high strength rail steels: a comparison between pearlitic and bainitic microstructures. Mater Sci Eng, A 2017;704:199–206.
[14] Enos D, Scully J. A critical-strain criterion for hydrogen embrittlement of cold-drawn, ultrafine pearlitic steel. Metall Mater Trans 2002;33(4):1151–66.
[15] Takakuwa O, Ogawa Y, Okazaki S, Nakamura M, Matsunaga H. A mechanism behind hydrogen-assisted fatigue crack growth in ferrite-pearlite steel focusing on its behavior in gaseous environment at elevated temperature. Corrosion Sci 2020;168:108558.
[16] Bott A, Dos Santos D, De Miranda P. Influence of cementite morphology on the hydrogen permeation parameters of low-carbon steel. J Mater Sci Lett 1993;12(6):390–3.
[17] Ramunni V, Coelho TDP, de Miranda PV. Interaction of hydrogen with the microstructure of low-carbon steel. Mater Sci Eng, A 2006;435:504–14.
[18] Sun J, Jiang T, Sun Y, Wang Y, Liu Y. A lamellar structured ultrafine grain ferrite-martensite dual-phase steel and its resistance to hydrogen embrittlement. J Alloys Compd 2017;698:390–9.
[19] Koyama M, Yu Y, Zhou J-X, Yoshimura N, Sakurada E, Ushioda K, Noguchi H. Elucidation of the effects of cementite morphology on damage formation during monotonic and cyclic tension in binary low carbon steels using in situ characterization. Mater Sci Eng, A 2016;667:358–67.
[20] Ogawa Y, Hino M, Nakamura M, Matsunaga H. Pearlite-driven surface-cracking and associated loss of tensile ductility in plain-carbon steels under exposure to high-pressure gaseous hydrogen. Int J Hydrogen Energy 2021;46(9):6945–59.
[21] Wang JJ-A, Ren F, Tan T, Liu K. The development of in situ fracture toughness evaluation techniques in hydrogen environment. Int J Hydrogen Energy 2015;40(4):2013–24.
[22] Pinson M, Springer H, Depover T, Verbeken K. Qualification of the in-situ bending technique towards the evaluation of the hydrogen induced fracture mechanism of martensitic fe–c steels. Mater Sci Eng, A 2020;792:139754.
[23] Hajilou T, Taji I, Christien F, He S, Scheiber D, Ecker W, Pippan R, Razumovskiy VI, Barnoush A. Hydrogen-enhanced intergranular failure of sulfur-doped nickel grain boundary: in situ electrochemical micro-cantilever bending vs. dft. Mater Sci Eng, A 2020;794:139967.
[24] Dearden J. A guide to the selection and welding of low alloy structural steels, vol. 3. Institute of Welding Transactions; 1940. p. 203.
[25] Barnoush A, Vehoff H. Recent developments in the study of hydrogen embrittlement: hydrogen effect on dislocation nucleation. Acta Mater 2010;58(16):5274–85.
[26] Hajilou T, Hope MS, Zavieh AH, Kheradmand N, Johnsen R, Barnoush A. In situ small-scale hydrogen embrittlement testing made easy: an electrolyte for preserving surface integrity at nano-scale during hydrogen charging. Int J Hydrogen Energy 2018;43(27):12516–29.
[27] Drexler A, Depover T, Verbeken K, Ecker W. Model-based interpretation of thermal desorption spectra of fe-c-ti alloys. J Alloys Compd 2019;789:647–57.
[28] Gensamer M, Pearsall E, Pellini W, Low J. The tensile properties of pearlite, bainite, and spheroidite. 2012.
[29] Jiang Y, Zhang B, Wang D, Zhou Y, Wang J, Han E-H, Ke W. Hydrogen-assisted fracture features of a high strength ferrite-pearlite steel. J Mater Sci Technol 2019;35(6):1081–7.

[30] Tvergaard V, Hutchinson JW. The relation between crack growth resistance and fracture process parameters in elastic-plastic solids. J Mech Phys Solid 1992;40(6):1377–97.
[31] Deng Y, Barnoush A. Hydrogen embrittlement revealed via novel in situ fracture experiments using notched micro-cantilever specimens. Acta Mater 2018;142:236–47.
[32] Shen X, Song W, Sevsek S, Ma Y, Hüter C, Spatschek R, Bleck W. Influence of microstructural morphology on hydrogen embrittlement in a medium-mn steel fe-12mn-3al-0.05 c. Metals 2019;9(9):929.
[33] Hardie D, Charles E, Lopez A. Hydrogen embrittlement of high strength pipeline steels. Corrosion Sci 2006;48(12):4378–85.
[34] Nanninga N, Grochowsi J, Heldt L, Rundman K. Role of microstructure, composition and hardness in resisting hydrogen embrittlement of fastener grade steels. Corrosion Sci 2010;52(4):1237–46.
[35] Liu M, Gan Y, Hanaor DA, Liu B, Chen C. An improved semi-analytical solution for stress at round-tip notches. Eng Fract Mech 2015;149:134–43.
[36] Chen X, Gerberich W. The kinetics and micromechanics of hydrogen assisted cracking in fe-3 pct si single crystals. Metall Trans A 1991;22(1):59–70.
[37] Kirchheim R. Reducing grain boundary, dislocation line and vacancy formation energies by solute segregation. i. theoretical background. Acta Mater 2007;55(15):5129–38.
[38] Pundt A, Kirchheim R. Hydrogen in metals: microstructural aspects. Annu Rev Mater Res 2006;36:555–608.
[39] Bae D, Lee J, Jeong J, Seol JB, Sung H, Kim JG. Hydrogen-induced ordering on the deformation mechanism of the as-cast high-mn steel. Mater Sci Eng, A 2021;825:141923.
[40] Abraham DP, Altstetter CJ. Hydrogen-enhanced localization of plasticity in an austenitic stainless steel. Metall Mater Trans 1995;26(11):2859–71.
[41] Deng Y, Hajilou T, Wan D, Kheradmand N, Barnoush A. In-situ micro-cantilever bending test in environmental scanning electron microscope: real time observation of hydrogen enhanced cracking. Scripta Mater 2017;127:19–23.
[42] Chattopadhyay S, Sellars C. Kinetics of pearlite spheroidisation during static annealing and during hot deformation. Acta Metall 1982;30(1):157–70.
[43] Lynch S. Hydrogen embrittlement phenomena and mechanisms. Corrosion Rev 2012;30(3–4):105–23.
[44] Cialone H, Asaro RJ. Hydrogen assisted fracture of spheroidized plain carbon steels. Metall Mater Trans 1981;12(8):1373–87.
[45] Islam MM, Zou C, Van Duin AC, Raman S. Interactions of hydrogen with the iron and iron carbide interfaces: a reaxff molecular dynamics study. Phys Chem Chem Phys 2016;18(2):761–71.
[46] Hanada H, Otsuka T, Nakashima H, Sasaki S, Hayakawa M, Sugisaki M. Profiling of hydrogen accumulation in a tempered martensite microstructure by means of tritium autoradiography. Scripta Mater 2005;53(11):1279–84.
[47] Jiang Y, Zhang B, Zhou Y, Wang J, Han E-H, Ke W. Atom probe tomographic observation of hydrogen trapping at carbides/ferrite interfaces for a high strength steel. J Mater Sci Technol 2018;34(8):1344–8.
[48] Song Y, Han Z, Chai M, Yang B, Liu Y, Cheng G, Li Y, Ai S. Effect of cementite on the hydrogen diffusion/trap characteristics of 2.25 cr-1mo-0.25 v steel with and without annealing. Materials 2018;11(5):788.
[49] McEniry EJ, Hickel T, Neugebauer J. Ab initio simulation of hydrogen-induced decohesion in cementite-containing microstructures. Acta Mater 2018;150:53–8.
[50] Maeda M, Shimamura J, Suzuki S. Effect of cementite dispersion on void formation process in spheroidize-annealed steels. ISIJ Int 2018;58(8):1490–9.
[51] Park Y, Bernstein I. The process of crack initiation and effective grain size for cleavage fracture in pearlitic eutectoid steel. Metall Trans A 1979;10(11):1653–64.

Paper II

Shabnam Karimi, Iman Taji, Tarlan Hajilou, Simona Palencsar, Arne Dugstad, Afrooz Barnoush, Kim Verbeken, Tom depover, Roy Johnsen

Role of cementite morphology on corrosion layer formation of high-strength carbon steels in sweet and sour environments

Corrosion Science Journal (2023)
https://www.sciencedirect.com/science/article/pii/S0010938X23000732

Corrosion Science 214 (2023) 111031

Contents lists available at ScienceDirect

Corrosion Science

journal homepage: www.elsevier.com/locate/corsci

Role of cementite morphology on corrosion layer formation of high-strength carbon steels in sweet and sour environments

Shabnam Karimi [a,*], Iman Taji [a], Tarlan Hajilou [a], Simona Palencsár [b], Arne Dugstad [b], Afrooz Barnoush [a,c], Kim Verbeken [d], Tom Depover [d], Roy Johnsen [a]

[a] Department of Mechanical and Industrial Engineering, Norwegian University of Science and Technology (NTNU), N-7491 Trondheim, Norway
[b] Institute for Energy Technology (IFE), P.O. Box 40, NO-2027, Kjeller, Norway
[c] Qatar Environment and Energy Research Institute (QEERI), Hamad Bin Khalifa University (HBKU), P.O. Box 34110, Doha, Qatar
[d] Department of Materials, Textiles and Chemical Engineering, Ghent University (UGent), Technologiepark 46, B-9052 Ghent, Belgium

ARTICLE INFO

Keywords:
Cementite morphology
Ferritic/pearlitic microstructure
Carbon steel corrosion
CO_2 environment
CO_2/H_2S environment

ABSTRACT

The effect of cementite morphology on the corrosion layer formation of four high-strength carbon steels was studied in an aqueous solution containing CO_2 and CO_2/H_2S. The linear polarization resistance and weight loss data reveal that as the cementite phase fraction is increased, the corrosion rate increases in CO_2 environment, while no trend is observed in the CO_2/H_2S environment. The results indicate that a porous and, non protective corrosion layer forms in the CO_2 environment, whereas a protective layer forms in the CO_2/H_2S environment. A mechanism that explains the role of cementite morphology on corrosion layer formation in a CO_2 environment is proposed for the studied materials.

1. Introduction

In the oil and gas industry, carbon steels are the most commonly used materials for pipe lines because of their excellent mechanical properties, availability, and cost. In a flexible pipe used as a riser, the armor wires are an integrated part of the multi-layer structure of the pipe, bearing the weight of the entire pipe [1]. Armor wires are typically made of high-strength carbon steels to sustain tensile loads owing to high tension and dynamic motions on flexible pipes [2,3]. Carbon steel used in the oil and gas industry experiences severe environmental conditions owing to the presence of corrosive elements and reactions that produce hydrogen in the environment. CO_2 and H_2S contained in gas and oil dissolve in water, produce H^+ ions, and lower the pH accordingly to create an acidic environment [4,5]:

$$CO_2 + H_2O \rightleftarrows H_2CO_3 \quad (1)$$

$$H_2CO_3 \rightleftarrows H^+ + HCO_3^- \quad (2)$$

$$HCO_3^- \rightleftarrows H^+ + CO_3^{2-} \quad (3)$$

$$H_2S \rightleftarrows H^+ + HS^- \quad (4)$$

$$HS^- \rightleftarrows H^+ + S^{2-} \quad (5)$$

The ions (HCO_3^-, CO_3^{2-}, HS^-, S^{2-}) can react with the released Fe^{2+} ions and control the corrosion process through the formation of an iron carbonate ($FeCO_3$) layer in a CO_2 environment and an iron sulfide layer in a H_2S environment [6,7]:

$$Fe^{2+} + 2HCO_3^- \rightleftarrows Fe(HCO_3)_2 \quad (6)$$

$$Fe(HCO_3)_2 \rightleftarrows FeCO_3 + CO_2 + H_2O \quad (7)$$

$$Fe^{2+} + CO_3^{2-} \rightleftarrows FeCO_3 \quad (8)$$

$$FeHS^+ \rightleftarrows FeS_{1-x} + xHS^- + (1-x)H^+ \quad (9)$$

$$Fe^{2+} + S^{2-} \rightleftarrows FeS \quad (10)$$

In the coexistence system of CO_2/H_2S, the corrosion layers that formed on the carbon steel surface are more complex. The environmental effects on the corrosion layer formation in a CO_2/H_2S environment have been extensively investigated, such as the effect of the H_2S partial pressure on corrosion layer [8–15], the effect of fluid flow on corrosion layer formation and dissolution [16,17], the dependence of corrosion product formation and morphology on the pH [18–20], the role of temperature on the corrosion products [21–24], and the relation between the corrosion layer and solution chemistry [25–27].

* Corresponding author.
E-mail address: shabnam.karimi@ntnu.no (S. Karimi).

https://doi.org/10.1016/j.corsci.2023.111031
Received 6 September 2022; Received in revised form 1 February 2023; Accepted 6 February 2023
Available online 9 February 2023

The corrosion rate of pipe line steels in a CO_2/H_2S brine system significantly depends on the H_2S partial pressure that accelerates the formation of the protective iron sulfide layer and decreases the corrosion [11]. Wang et al. [8] investigated the effect of H_2S partial pressure on the corrosion products formed in high-strength sulfur-resistant steel in oilfield-produced water under supercritical CO_2 conditions. The results of their study indicated that the structure of the corrosion product evolved from monolayer to bilayer with an increase in the H_2S partial pressure. The inner layer of the bilayer consisted of iron sulfide and $FeCO_3$ and the outer layer was $FeCO_3$. The density of the corrosion layer increased with an increase in the H_2S partial pressure, which reduced steel corrosion. The CO_2/H_2S ratio in their study was greater than 1500. It has been reported elsewhere that no $FeCO_3$ were detected in the corrosion products formed at CO_2/H_2S ratios below 1500 [15]. Wang et al. [28] reported that in the presence of H_2S, the corrosion layer exhibited a three-layer structure in a corrosive environment. Because H_2S can prevent the formation of iron oxides, the middle and inner layers are enriched with iron sulfides and iron oxides, respectively, and the outer layer is composed of hydroxides. In another study, the competitive formation of $FeCO_3$ and FeS layers on $API\ X65$ steel exposed to sweet and sour environments was investigated. The results indicated that a protective corrosion layer formed at 120 °C regardless of the H_2S presence. In the absence of H_2S, a steady and dense $FeCO_3$ layer was formed. In the presence of H_2S, the formation of the FeS film decreased the CO_2 corrosion process and hindered the $FeCO_3$ precipitation. Hesketh et al. [9] suggested that in an aqueous CO_2/H_2S system at high H_2S partial pressures, a protective and, dense sulfide layer forms on the metal surface, which limits the steel dissolution and transport of H_2S on the surface of the metal and prevents pit development.

The other important environmental factor that can affect the corrosion product formation is pH. In general, the literature confirms that at high pH values, and in the presence of H_2S, iron sulfide can precipitate on the metal surface [20]. Sardisco et al. [18] studied the protectiveness of the corrosion layer formed on Armco iron in a $CO_2/H_2S/H_2O$ environment with pH values ranging from 3 to 11. They reported that the corrosion layer showed the least protection in the pH range of 6.5 to 8.

In a study by Abelev et al. [21], the effect of temperature and different H_2S concentrations on the corrosion layer formed on iron with exposure to the CO_2-saturated 3 wt% NaCl solution was investigated. The results revealed that a protective layer, including $Fe(II)$ bonded to O and S, forms with the addition of 5 ppm H_2S at ambient temperature. At high H_2S concentrations, a thick porous, and inhomogeneous corrosion layer is formed, which is less protective. At a high temperature, 85 °C with the addition of 50 ppm H_2S, a dense protective corrosion layer of FeS_2, $FeCO_3$, and Fe_3O_4, is formed. The temperature can also affect the structure of the iron sulfide product, which forms in the presence of H_2S. Shi et al. [22] argued that the formation of mackinawite on $X60$ steel occurs at low temperatures and H_2S partial pressures, whereas pyrrhotite forms at high temperatures and H_2S partial pressures.

As reported in the literature, fluid flow prevents the formation of a protective scale [17]. Zhang et al. [16] studied the synergistic effects of fluid flow, CO_2, and H_2S on the corrosion layer formation on low-carbon steel. They concluded that in the absence of H_2S, the fluid flow can facilitate the transport of Fe^{2+} ions and decrease Fe^{2+} concentration between the Fe_3C remaining layers. Therefore, the formation of a porous and loose corrosion layer occurs that can easily break in some regions under the action of fluid flow. In the presence of H_2S, the $FeCO_3$ formation can be prevented by preferential adsorption of $FeHS^+$ ions, which forms an iron sulfide film.

In addition to the environmental conditions, carbon steel alloying elements [29–31] and microstructure influence the corrosion behavior and the corrosion layer formation. Palacios et al. [32] identified that under CO_2 exposure in an aqueous environment, the adherence of the corrosion layer to the steel as well as the thickness of the layer are influenced by the microstructure of the steel. They revealed that the $FeCO_3$ layer formed on the normalized specimen was thicker and better attached to steel than the quenched and tempered specimen layers. They explained that the $FeCO_3$ formation on a normalized specimen with a pearlitic microstructure was dependent on the remaining cementite distribution. As the iron between the cementite layers corroded away, a cementite phase was left behind with cavities between the cementite layers, and the local concentration of Fe^{2+} ions increased in these cavities. Local flow stagnation and high Fe^{2+} concentrations in the cavities allowed the formation of $FeCO_3$ between the remaining cementite layers. Dugstad et al. [33] discussed the effect of various heat treatments on corrosion layer formation in chromium-containing and unalloyed steels in a CO_2 environment. In unalloyed steels, they found that the adherence of the protective corrosion layer decreased with increasing tempering temperature, while a protective corrosion layer formed on the chromium-containing steels, and no mesa attack was observed regardless of their heat treatment. Kim et al. [34] reported iron sulfide layer precipitation on steel to be significantly dependent on the steel microstructure and cementite distribution. They mentioned that differences in the shape and distribution of the cementite phase can influence the mechanical attachment of the iron sulfide layer to the steel. Lopez et al. [35] discussed the effect of the steel microstructure on the corrosion layer properties, such as morphology and different chemical compound proportions. Ueda et al. [36] proposed that the lamellar morphology of cementite promotes more efficient adherence of the corrosion products to the steel substrate. This correlation between the lamellar cementite and corrosion layer adherence has also been presented in other studies [37,38]. According to Anyanwu et al. [37], the presence of cementite promotes the precipitation of iron sulfide in the pearlite regions in an H_2S environment. In general, the favored precipitation of iron sulfide in the pearlite areas of ferritic/pearlitic steel has been previously reported [39,40].

Considering the substantial investigation of the environmental factors affecting the corrosion rate (CR) and corrosion layer, the corrosion behavior in CO_2 and CO_2/H_2S environments requires detailed investigation on the effects of the microstructure of carbon steels. The environmental effects coupled with the role of carbon steel microstructure on corrosion allow for a more elaborate understanding of the corrosion of carbon steels in CO_2 and CO_2/H_2S environments.

Most studies that investigated the role of the microstructure or cementite morphology on the corrosion behavior of steels have been conducted on low or medium carbon steels, and they have generally compared different microstructures such as pearlites with martensites, or bainites. Moreover, few studies have focused on the effect of cementite morphology on corrosion layer formation. The present study investigated the effects of cementite morphology on the corrosion behavior and corrosion layer formation of three high-carbon steels and one low-carbon steel, which are all applied as tensile armor wires. The carbon steel microstructures included ferrite/pearlite and spheroidite, and they have delicate differences. Therefore, detailed microstructural characterizations were conducted to reveal the role of cementite morphology on corrosion layer formation in both CO_2 and CO_2/H_2S environments.

2. Experimental

2.1. Materials and sample preparation

Four carbon steels with different carbon contents and microstructures are investigated in this study. Carbon steels are tensile armor wires of flexible pipes, received in the form of drawn curved wires with widths of 9 to 12 mm and a thickness of 3 mm. Their chemical compositions and mechanical properties [41,42] are summarized in Table 1.

Table 1
Chemical composition and the mechanical properties (yield strength, YS, and ultimate tensile strength, UTS) of the studied materials [41].

Material (wt%)	C	Al	Si	P	Mo	V	Cr	Mn	Ni	Cu	YS (GPa)	UTS (GPa)
$CS28$	0.28	0.32	0.32	0.20	0.20	0.40	0.42	0.72	0.46	0.62	0.8	0.85
$CS62$	0.62	0.26	0.40	0.23	0.46	0.70	0.61	1.36	0.89	0.75	1.1	1.3
$CS65$	0.65	0.30	0.24	0.20	0.35	0.51	0.51	0.96	0.60	0.75	1.25	1.4
$CS83$	0.83	0.19	0.35	0.30	0.35	0.54	0.55	1.07	0.69	0.59	1.4	1.6

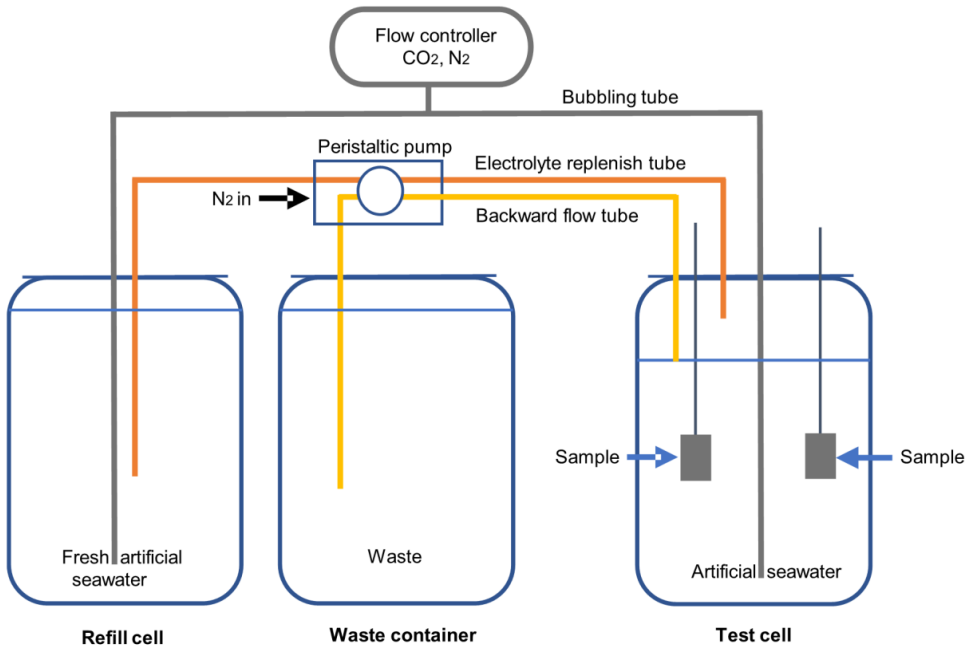

Fig. 1. Schematic of the corrosion test setup used for the CO_2 exposure. The test cell is replenished by fresh artificial seawater in CO_2 environment experiment, while in CO_2/H_2S environment experiment the precipitation of FeS kept the concentration of the dissolved Fe^{2+} ions low and therefore the test cell is not replenished by fresh artificial seawater.

For corrosion testing, the studied materials were cut into rectangular specimens with a length of 12 mm and the same widths and thickness as those of the wires. All surfaces of the specimens were ground with 320 grit SiC paper, washed in acetone and isopropanol in an ultrasound bath, and dried.

Another set of samples was prepared for microstructural analysis by grinding abrasive papers up to 4000 grit SiC, followed by mechanical polishing with 3 μm and 1 μm diamond suspensions, and finally etching in 2% nital solution.

2.2. Corrosion tests

Modified $ASTM\ D1141$-90 [43] seawater (without calcium chloride to avoid the formation of calcium carbonate ($CaCO_3$) [44]) was used as the corrosion test electrolyte. Its chemical composition is presented in Table 2. A schematic of the corrosion test setup is shown in Fig. 1. The corrosion tests were performed in a setup comprising two parts: the test cell, where the test specimens were immersed in the test electrolyte, and the refill cell, which contained the fresh electrolyte required to replenish the electrolyte in the test cell. The test cell was filled with the test electrolyte and continuously purged with the required gas mixture. The electrolyte was gently stirred and maintained at 25 °C in a water bath. To achieve the required gas composition and feed the test cell, a gas-dosing system based on *Bronkhorst* mass flow controllers was used to blend N_2, CO_2, and H_2S. The refill cell was maintained at room temperature and purged with the same gas composition as that of the test cell.

Table 2
Chemical composition of the corrosion test electrolyte [43].

Compound	NaCl	$MgCl_2$	Na_2SO_4	KCl	$NaHCO_3$	H_3BO_3	$SrCl_2$
Content (g/l)	24.53	5.2	4.09	0.695	0.201	0.027	0.025

The electrolyte was circulated between the test cell and refill cell using a peristaltic pump equipped with $Tygon$ and PVC tubes. The flow rates were controlled by the tubing diameter and the rotation speed of the pump. To avoid oxygen contamination, the pump was placed in a chamber purged with N_2. When the peristaltic pump was on, the flow of liquid into the test cell was continuous and had a maximum rate of 4 ml/min (using a 1.143 mm tubing diameter). The backward flow had a maximum rate of 18 ml/min (using a 3.175 mm tubing diameter) and was self-regulated by draw-off to eliminate the risk of overflowing the test cell. The backward flow was directed to a waste container. The pH value was continuously recorded. The pH increased slightly (between 5.77 and 6.08) during both the CO_2 and CO_2/H_2S exposure experiments. The test cell electrolyte was sampled frequently during exposure to analyze its Fe^{2+} ion concentration. The Fe^{2+} ions were converted to a colored Fe complex, which was photometrically quantified. The electrolyte was continuously replaced by fresh electrolyte (with no dissolved corrosion products) at a flow rate of ca. 0.8–1.6 l/day to ensure a low concentration of Fe^{2+} (less than 80 ppm in the test cell).

Two sets of experiments were performed in the above-mentioned setup: first, the test cell was purged with 0.2 bar CO_2, and second,

with 0.2 bar CO_2 and 1 mbar H_2S, with a total flow rate of 200 ml/min. In the second test set, because the precipitation of FeS kept the concentration of the dissolved Fe^{2+} ions low, no electrolyte replacement was required. Each set of experiments was performed in three rounds, and the duration of both sets of tests was 504 h (21 d). Thus, the experimental setup used for the CO_2/H_2S exposure consisted of only the test cell and the corresponding gas flow line, see Fig. 1.

2.3. Corrosion rate measurements

The corrosion rates of all the studied materials in both experimental sets were measured using the linear polarization resistance (LPR) and were determined by weight-loss method. LPR measurements were performed using a regular 3-electrode electrochemical setup, with a titanium spiral as the counter electrode and a carbon steel cylindrical specimen as the pseudo-reference electrode. A *Gamry PC3/750* potentiostat with $ECM8$ multiplexer and $CMS105$ software were used for the LPR measurements. The procedure used to interpret LPR data is generally based on the methodology described in the literature [45–47]. A linear potential sweep was applied to the working electrode from −5 mV to 5 mV vs. the OCP. Within this restricted potential range, the resulting current response can be considered linear, allowing the polarization resistance (R_p) to be calculated as the slope of the potential (E) vs. current (I) plot:

$$R_p = \frac{\delta E}{\delta I} \tag{11}$$

The corrosion current density (i_{corr}) was subsequently calculated using the Stern–Geary equation [45,48], where B is the Stern–Geary coefficient and A is the specimen area.

$$i_{corr} = 10^6 \frac{B}{R_p A} \tag{12}$$

The Stern–Geary coefficient (B) is related to the Tafel slopes of the anodic and cathodic half-reactions, that is, β_a and β_c:

$$B = \frac{\beta_a \beta_c}{2.3(\beta_a + \beta_c)} \tag{13}$$

In the absence of Tafel slopes, the B coefficient was determined from the weight loss data. The corrosion current density, steel density, and Fe molar mass were then used to calculate the corrosion rate (CR) or penetration rate using Faraday's law. All relevant constants were included, which simplifies to:

$$CR\ (\mathrm{mm/y}) = 1.16 i_{corr}\ (\frac{\mathrm{A}}{\mathrm{m}^2}) \tag{14}$$

To perform the weight-loss method, the samples were weighed using an analytical balance with an accuracy of $\pm 10^{-4}$ g before and after the corrosion test. After the corrosion products were removed by immersing the samples in *Clarke's* solution (inhibited hydrochloric acid, that is 36% HCl containing 50 g/l $SnCl_2$ and 30 g/l $SbCl_3$) for 1 min according to $ASTM$ standard G 1-03 [49]. The weight loss of the samples was used to calculate the average corrosion rate of each carbon steel sample using the following equation:

$$CR\ (\mathrm{mm/y}) = 8.76 \times 10^4 \frac{\mathrm{W}}{\rho \mathrm{A} t} \tag{15}$$

where W is the weight loss of the sample in grams, A is the total area of the sample in cm^2, t is the immersion time in hours, ρ is the density of the material in g/cm^3, and 8.76×10^4 is the unit conversion constant [50,51]. It should be noted that using this method, a corrosion rate that is averaged over the entire exposed area is obtained for a specific sample.

2.4. Cross-sectional characterization of corrosion layers

To observe the morphology and thickness of the corrosion layers formed on the specimens exposed to the CO_2 environment, the samples were embedded in *DuroCit−3kit*, an acrylic resin that is suitable for the protection of the corrosion layers. After the curing time, the embedded samples were cut. Then, the cross-sectioned samples were ground up to 4000 grit with SiC abrasive paper and polished with 3 μm and 1 μm diamond suspensions.

The corrosion layers formed on the specimens exposed to the CO_2/H_2S environment were on the nanometer scale, and the embedding process could damage the layer. Therefore, a focused ion beam (FIB) was employed to characterize the cross-sections of the specimens exposed to the CO_2/H_2S environment. Prior to the cross-sectional observation by ion beam-induced secondary electron imaging, two platinum protection layers with thicknesses of 1 μm using an electron beam and 1.5 μm using an ion beam were applied on a selected area on the sample surfaces to protect the corrosion layer from potential damage by the ion beam.

2.5. X-ray photoelectron spectroscopy analysis

The chemical composition of the corrosion layers was determined using X-ray photoelectron spectroscopy (XPS) performed on a VG $Escalab$ 220i-XL spectrometer. The samples were transferred for XPS analysis inside a desiccator to minimize exposure to the open environment. XPS analysis was performed using a *Kratos Axis Ultra DLD*. A monochromatic Al $K\alpha$ source (12 mA, 12 KV) was used for spectrometry. The sample analysis chamber pressure was 1×10^{-9} Torr (0.13 μPa) during the operation. Elemental maps were collected with a pass energy of 120 V using two sweeps. High-resolution regional acquisitions were performed with a pass energy of 20 V using ten sweeps and 0.1 eV step size for each element. The analysis area was 300 × 700 μm^2, and five areas were analyzed for each sample. Argon sputtering with an energy of 4 KV was used for 30 s to remove surface contamination before the start of the XPS analysis. Regional peaks were fitted by Shirley background subtraction Using *Casa XPS* software. For curve fitting, evaluation, and quantification, *Gaussian/Lorentzian* asymmetry was used, and the full width at half maximum ($FWHM$) was kept constant for the oxide components.

3. Results

3.1. Materials characterization

Fig. 2 shows SEM micrographs from the surface view of the studied materials at two magnifications. Material $CS28$ is a low-carbon steel (Table 1) with both large and small drawn ferritic grains, including different types of small ferrite sub grains. The cementite particles continuously precipitated mainly along the grain boundaries, while a small fraction of cementite particles was dispersed inside the ferrite grains. The ferrite grains were oriented along the drawing direction.

Materials $CS62$ and $CS65$ are high-carbon steels that exhibited a ferrite–cementite microstructure with small fractions of ferrite. The morphology of the cementite in material $CS62$ consisted of spherical particles or broken lamellae in a ferrite matrix, whereas material $CS65$ showed a pearlite microstructure with thick lamellae of cementite in a ferrite matrix (Fig. 2). The ferrite grain size and connection network between the ferritic grains were larger in material $CS65$ than in material $CS62$. Material $CS83$ was a hypereutectoid high-carbon steel that exhibited a predominantly lamellar pearlite microstructure with a lower fraction of ferrite than the other materials.

The ferrite, cementite, and pearlite phase fractions for all materials were determined by image analysis using ImageJ $Fiji$, and the data are listed in Table 3. The pearlite colonies had different interlamellar spacings in the materials $CS65$ and $CS83$. The average interlamellar spacing measured by $Fiji$ shows that material $CS83$ had finer pearlite with an average interlamellar spacing of 117±30 nm than material $CS65$ with an average interlamellar spacing size of 242 ± 64 nm (Table 3).

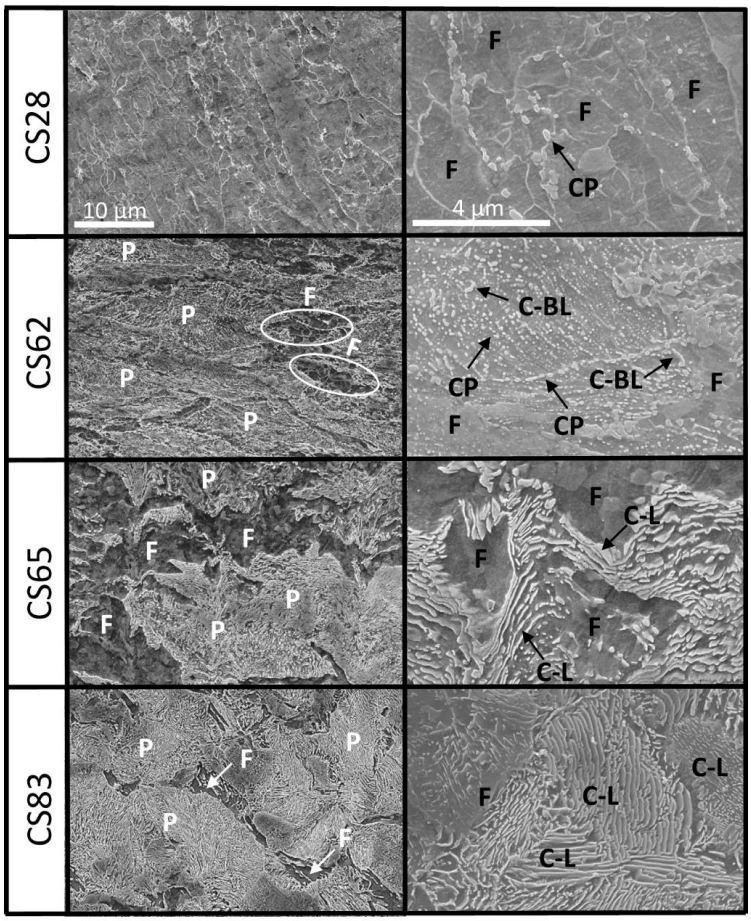

Fig. 2. *SEM* micrographs of the studied materials surface. The right column shows the high magnification images of the microstructure of the materials. The magnification of the *SEM* images in each column is the same for all materials. The ferrite and pearlite phases are marked by F and P, respectively. The cementite particles, cementite lamellae, and broken lamella of cementite are marked by C-P, C-L, and C-BL, respectively.

Table 3
Microstructures phase fraction and interlamellar spacing.

Material	Ferrite (%)	Cementite (%)	Pearlite (%)	Interlamellar spacing (nm)
*CS*28	96	4	35	-
*CS*62	91	9	81	-
*CS*65	90	10	85	242-±64
*CS*83	88	12	98	117-±30

3.2. Corrosion rate measurements

The results of the *LPR* measurements for all materials in both CO_2 and CO_2/H_2S environments are summarized in Fig. 3. The curves obtained from the *LPR* measurements were fitted using a polynomial equation. Fig. 3a shows that the corrosion rate in the presence of CO_2 continuously increases with time for all materials, and the curves did not stabilize during the experiments. The corrosion rate increment is high for the materials *CS*65 and *CS*83, both of which have a pearlitic microstructure.

No clear corrosion rate-carbon content/cementite phase fraction relationship is observed in the CO_2/H_2S environment. It can be seen that material *CS*28, which has the lowest corrosion rate in CO_2 environment, showed the highest corrosion rate in the CO_2/H_2S environment, whereas material *CS*83 exhibits the lowest corrosion rate among the studied materials.

Fig. 4 shows the average corrosion rates obtained from the weight loss data for all the studied materials exposed to the CO_2 and CO_2/H_2S environments for 21 d. Error bars represent the standard deviation of the mean value of the weight loss data of the three samples for each material. The weight loss corrosion rate results show that the average corrosion rate of the studied materials increases with the carbon content or cementite phase increment in the CO_2 environment. However, this trend is not observed in CO_2/H_2S environment. As shown in Fig. 4, material *CS*28 had the lowest corrosion rate in the CO_2 environment, and has the highest corrosion rate in the CO_2/H_2S environment. Materials CS62 and CS83 displayed almost the same corrosion rate, while the corrosion rate of material CS65 was higher than both. Therefore, the corrosion rates of the studied materials in the CO_2/H_2S environment does not exhibit a specified trend.

As is shown in Fig. 3b, and Fig. 4b, the presence of H_2S induced a significant reduction in the corrosion rate by one order of magnitude compared to the CO_2 environment. In Fig. 3b, all materials display a high corrosion rate during the first hours of the experiment, when

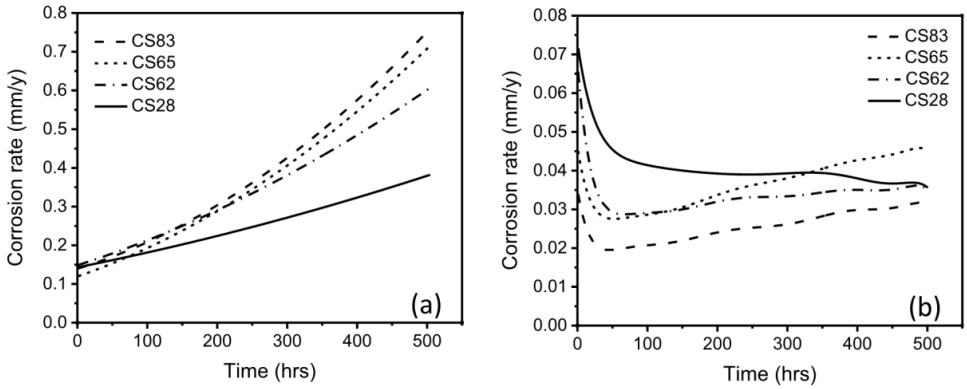

Fig. 3. *LPR* corrosion rates versus exposure time in the 0.2 bar CO_2 environment (a) and the 0.2 bar CO_2/1 mbar H_2S environment (b).

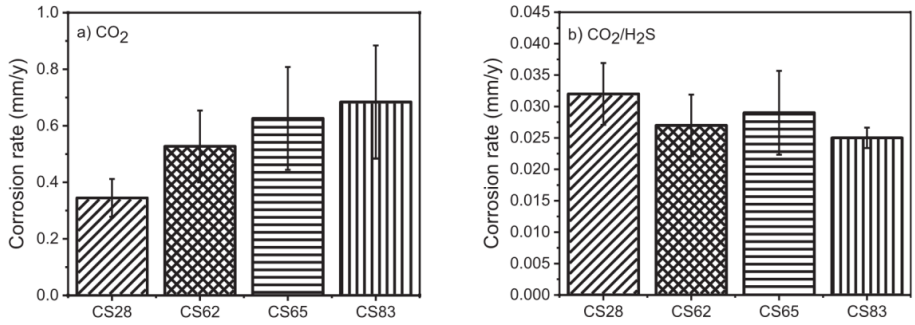

Fig. 4. Corrosion rates calculated from weight loss data after exposure to the 0.2 bar CO_2 environment (a) and the 0.2 bar CO_2/1 mbar H_2S environment (b) for 21 d. The columns show the mean value of three tests and the bars represent the standard deviation of the mean value.

the corrosion layer is not yet protective, and ions can transfer freely through it. Then, the corrosion rate decreases with time until approximately 40 h. Hereafter, the corrosion rate of material *CS*28 is almost stabilized, while the corrosion rates of materials *CS*62, *CS*65, and *CS*83, show a slight increase, with the highest corrosion rate increase in material *CS*65. It should be noted that these data are based on the results obtained in the performed experiments' time frame (21 d). The corrosion rates of all the studied materials can be changed over a longer period of time.

3.3. Corrosion layer characterization

To provide satisfactory protection, the corrosion layer should exhibit good adhesion and full coverage of the sample surface. In addition, the corrosion layer thickness, porosity, and composition, are important criteria for creating a protective layer that can significantly affect the corrosion rate [52–54]. The results that demonstrate and evaluate these criteria are presented in the following sections.

3.3.1. Corrosion layer morphology and thickness

Fig. 5 shows the surface morphology of the corrosion layers formed on all materials after 21 d of exposure in the CO_2 and CO_2/H_2S environments. In the CO_2 environment, by comparing the *SEM* images, the surface of the corrosion layer formed on material *CS*28 seems to have an uneven and rough appearance. This roughness is low for materials *CS*62 and *CS*65, whereas for material *CS*83 the corrosion layer exhibits a more compact and uniform appearance. The differences between the corrosion layer interface appearances are more evident in the cross-sectional *SEM* images shown in Fig. 6. Both the corroded sample surface/corrosion layer interface (shown by the green line (1) in Fig. 6 *CS*28) and the surface of the corrosion layer (shown by the red line (2) in Fig. 6 *CS*28) are quite uneven for material *CS*28, whereas they are almost uniform for materials *CS*62 and *CS*83. Material *CS*65 exhibits some localized corrosion at the corroded sample surface/corrosion layer interface.

A substantial reduction in the corrosion layer thickness was observed in the materials exposed to the environment containing 1 mbar H_2S compared with the samples in the pure CO_2 environment. By comparing the corrosion layer thicknesses of different materials, an increase in thickness was observed with increasing carbon content in both the CO_2 and CO_2/H_2S environments, as shown in Fig. 6. Materials *CS*62 and *CS*65 show almost similar corrosion layer thicknesses in the CO_2 environment, and the corrosion layer thickness of material *CS*65 is slightly lower than that of material *CS*62. In the CO_2/H_2S environment, the same trend is observed, which means that the corrosion layer thickness increases with increasing carbon content; however, the corrosion layer thickness of material *CS*65 is significantly lower than that of the other two high-carbon materials, *CS*62 and *CS*83, and it is closer to that of material *CS*28.

3.3.2. Corrosion layer chemical composition

The chemical compositions of the surface and cross-section of the corrosion layer were analyzed using *XPS* and *EDS*, respectively. Fig. 7 represents the entire range of binding energies from 0 to 1200 eV of the material *CS*65 corrosion layer (the full spectrum of all materials is similar). The peaks for Fe 2*p*, O 1*s*, and C 1*s*, are visible in all the carbon steel surfaces in both the CO_2 and CO_2/H_2S environments, whereas the S 2*p* peak is only observed in the CO_2/H_2S environment.

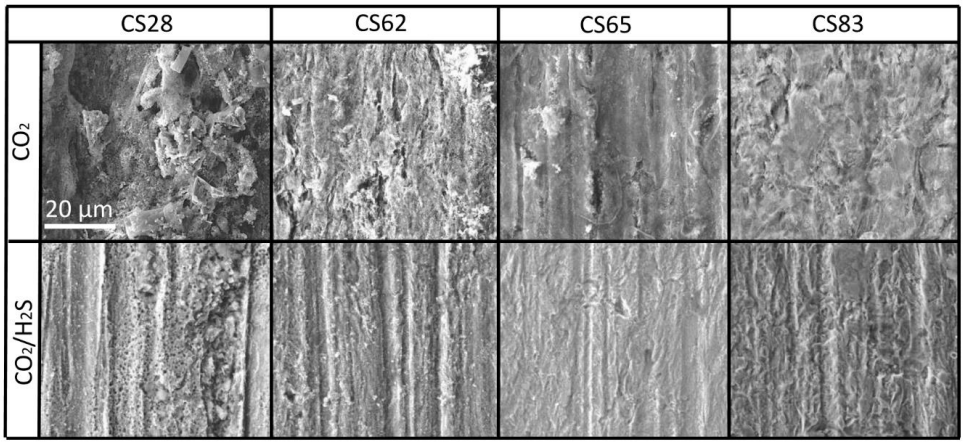

Fig. 5. *SEM* micrographs of the surface morphology of carbon steel samples after exposure to the 0.2 bar CO_2 environment (first row) and the 0.2 bar CO_2/1 mbar H_2S environment (second row) for 21 d.

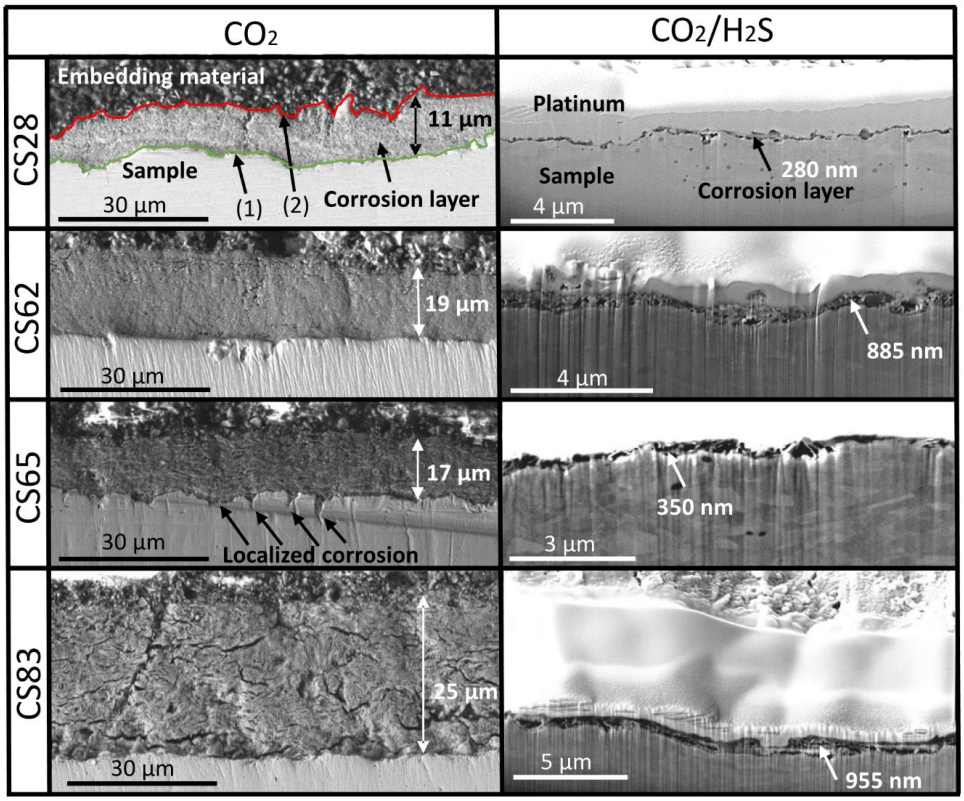

Fig. 6. Cross-section morphologies of the corrosion layers of the studied materials exposed to 0.2 bar CO_2 (left column) and the 0.2 bar CO_2/1 mbar H_2S (right column) environments for 21 d. The surface of the samples, exposed to the 0.2 bar CO_2/1 mbar H_2S environment, were covered with platinum before milling to protect the nano-scale corrosion layers. The numbers written in each image denote the average thickness of the corrosion layers of two samples for each material and environment. For CO_2 exposure, the thicknesses are shown by double arrows. For CO_2/H_2S exposure, the thicknesses are pointed by arrows because they are thin.

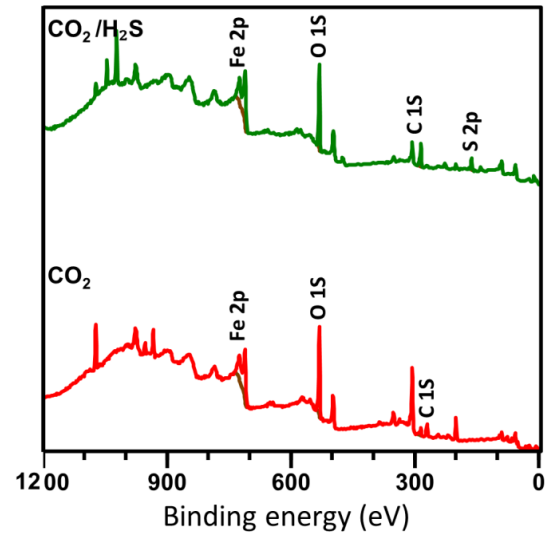

Fig. 7. *XPS* overview spectrum obtained from the surface of the material *CS*65 after 21 d exposure to the 0.2 bar CO_2 and 0.2 bar CO_2/1 mbar H_2S environments.

Table 4
Relative intensities (in atomic percent) of the C 1*s* signals for the corrosion layers formed in the 0.2 bar CO_2 environment.

Material	$FeCO_3$	C–Cl	C–C
*CS*28	4.56	15.54	79.89
*CS*62	10.56	18.67	70.76
*CS*65	11.64	9.05	79.29
*CS*83	9.01	19.44	71.54

Table 5
Relative intensities (in atomic percent) of the *O*1*s* signals for the corrosion layers formed in the 0.2 bar CO_2 environment.

Material	$FeCO_3$	Fe_2O_3
*CS*28	86.27	13.72
*CS*62	70.59	29.4
*CS*65	56.94	43.05
*CS*83	55.58	44.41

The regional spectrum of the carbon 1*s* is shown in Fig. 8 for all materials exposed to the CO_2 environment. All spectra were deconvoluted into three evident peaks around 284.5–285.5 eV, 286–287 eV, and 288–290 eV. The first peak at 284.5–285.5 eV corresponds to adventitious carbon, which is always introduced to the samples from the environment. The second peak at 286–287 eV can be attributed to a compound of carbon with chlorine or carbon with oxygen [55]. The third small peak at 288–290 eV displays the presence of $FeCO_3$ [56]. The relative intensities of the C 1*s* signals for each peak are listed in Table 4 for all materials. The $FeCO_3$ peak exhibits a high intensity in the materials *CS*65, *CS*62, and *CS*83, and material *CS*28 shows the lowest $FeCO_3$ intensity.

The second column of Fig. 8 presents the deconvoluted peaks of the *XPS* spectrum of oxygen 1*s* for each material. The first peak at 530–530.5 eV is specified as ferric oxide (Fe_2O_3), and the second peak at 531.7–532 eV is attributed to $FeCO_3$ [55]. The relative intensities corresponding to each peak are presented in Table 5.

The *XPS* spectrum for the Fe 2*p* region of each material is presented in the third column of Fig. 8 and the relative intensities of the deconvoluted peaks are listed in Table 6. The Fe^{2+} peak which is

Table 6
Relative intensities (in atomic percent) of the Fe2*p* signals for the corrosion layers formed in the 0.2 bar CO_2 environment.

Material	Fe^{2+}	Fe^{3+}	Fe
*CS*28	57.39	39.16	3.44
*CS*62	44.05	50.78	5.15
*CS*65	36.42	60.46	3.1
*CS*83	26.09	70.19	3.7

Table 7
Relative intensities (in atomic percent) of the Fe2*p* signals for the corrosion layers formed in the 0.2 bar CO_2 1 mbar H_2S environment.

Material	Fe^{2+}	FeS	Fe^{3+}	FeS_2
*CS*28	6.91	52.12	25.05	5.91
*CS*62	21.45	46.43	15.49	16.61
*CS*65	10.87	56.51	3.4	29.2
*CS*83	6.64	66.47	11.11	15.76

present at 712–714 eV is obvious in all materials. This peak can be attributed to the presence of $FeCO_3$ on the top surface of the corrosion layer [57,58]. However, this can also be related to $Fe(OH)_2$ [59]. Two other peaks around 709.5–710.5 eV and 706.5–707.5 eV are related to Fe^{3+} iron compounds, such as ferric oxide (Fe_2O_3) and pure iron, respectively [58]. According to the peak intensities of different materials shown in Table 5 for O 1*s* and Table 6 for Fe 2*p*, the intensity of Fe^{2+} decreases and the intensity of Fe^{3+} iron compounds increases with increasing carbon content. Material *CS*83 exhibits the highest amount of Fe^{3+} iron compounds and the lowest amount of Fe^{2+} compounds. The presence of iron metal at 706.5 to 707.5 eV, observed for all materials, can be the result of Ar^+ sputtering, and it cannot be related to the uncorroded ferrite [35]. Ion bombardment can cause physical and chemical changes, and reduce Fe_3O_4, Fe_2O_3, and FeO, on the surface. This reduction can be attributed to the shift in intensity from the Fe^{3+} position at 711.2 eV to low binding energies in the present study *XPS* results (709.5- 710.5 eV), and even to a mixture of Fe^{3+}, Fe^{2+}, and iron metal [60,61].

Fig. 9 presents the *XPS* spectra of S 2*p* and Fe 2*p* for the corrosion layer formed on each material after exposure to the CO_2/H_2S environment. The two peaks at 710.5–711.5 eV and 708–709 eV correspond to mackinawite (FeS) and pyrite (FeS_2), respectively, in the Fe 2*p* scan for all materials in Fig. 9 [7,62]. FeS and FeS_2 peaks in the S 2*p* spectrum at approximately 163.3 and 161.6 eV confirm the presence of these two compounds in the corrosion layers formed in the CO_2/H_2S environment. Moreover, *XPS* analysis revealed the presence of Fe^{2+} and Fe^{3+} iron compounds in the CO_2/H_2S environment.

The relative intensities of the deconvoluted FeS and FeS_2 peaks for Fe 2*p* are listed in Table 7. The sum of FeS and FeS_2 intensities for each material reveals that the mackinawite and pyrite intensity increase with increased carbon content, and materials with pearlitic microstructures (*CS*65 and *CS*83) exhibit almost similar FeS and FeS_2 intensities (85 and 81, respectively). The corrosion layers of materials *CS*62 and *CS*28 are richer in Fe^{2+} and Fe^{3+}-related compounds compared to materials *CS*65 and *CS*83.

It should be noted that the *XPS* data were collected from the surface of the corrosion layer at a depth of approximately 5 nm. Therefore, *EDS* was performed on the cross-sections of the *CS*28 and *CS*83 corrosion layers to verify the presence of the main elements that are recognized by *XPS*. Because the corrosion layers formed on the materials exposed to the CO_2/H_2S environment are quite thin (less than 1 μm), the conditions for performing the *EDS* analysis on their corrosion layer cross-sections are not ideal, and the *EDS* analysis is only performed on the materials that are exposed to the CO_2 environment. The presence of the main elements of the corrosion layers, Iron, Oxygen and Carbon, was verified in *EDS* results in Fig. 10. The scan shows the *EDS* elemental concentration profile along the yellow line

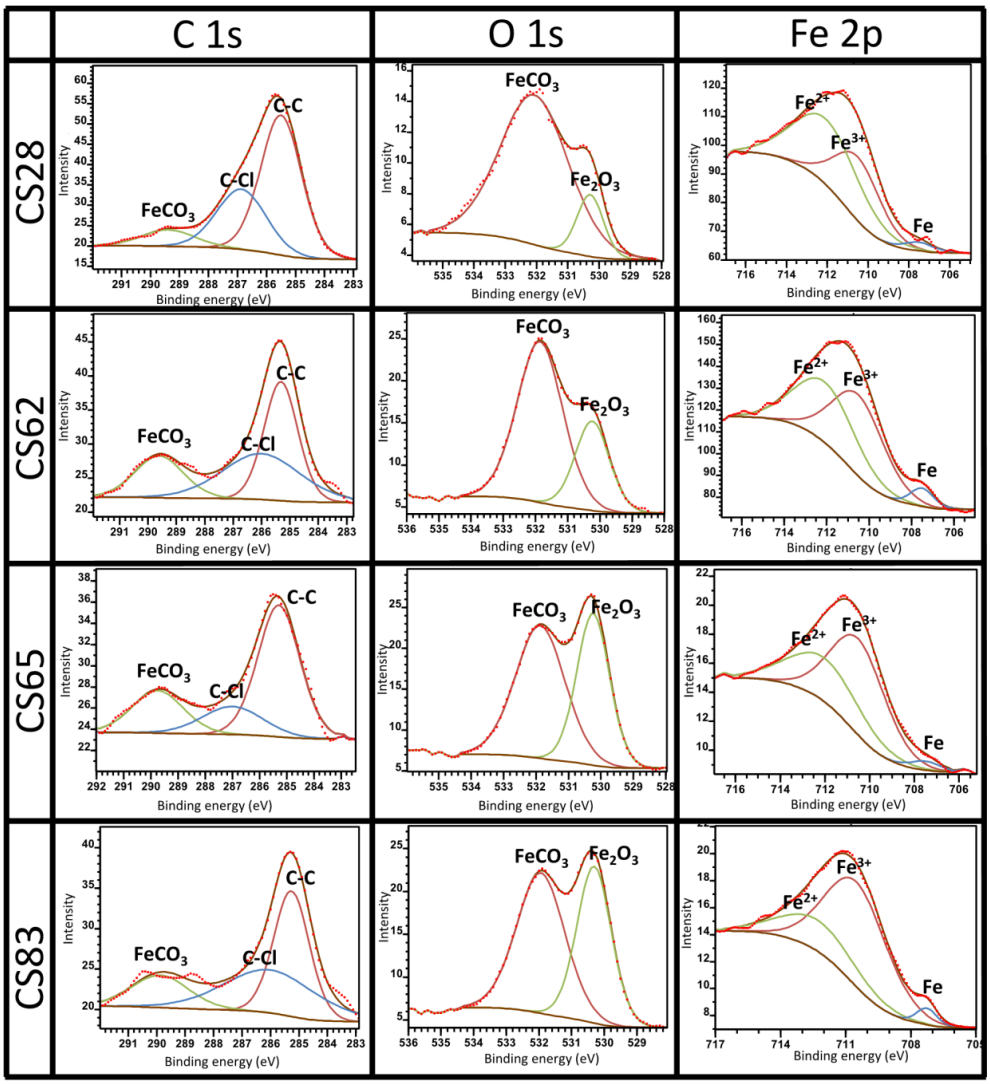

Fig. 8. Regional *XPS* spectrum of C, O, and Fe for the corrosion layer formed on the surface of all materials exposed to the 0.2 bar CO_2 environment.

for each material. The iron intensity (green line in the graphs) is at a high density where the scan line passes the material; then, it decreases to a high extent where the corrosion layer appears. In material *CS*28 the iron intensity was higher in the corrosion layer area than in material *CS*83. In addition, material *CS*28 presents a high oxygen intensity in the corrosion layer, while carbon has the highest intensity in the corrosion products of material *CS*83. As the embedding material begins to appear, the carbon and oxygen intensities are quite high (because an acrylic mounting system is used to embed the samples), and the iron intensity decreases to zero.

3.3.3. Corrosion layer porosity

Porosity is a crucial factor in determining the protective role of the corrosion layer by facilitating ion migration. *FIB* was used to investigate the porosity to obtain a more obvious view of the corrosion layer cross-section. The *SEM* images of the cross-sections prepared using *FIB* are shown in Fig. 11. By comparing material *CS*28 with materials *CS*65 and *CS*83, it is obvious that the corrosion layer formed on the lamellar and high-carbon microstructure (Fig. 11b and c) is quite porous, and the cross-sectional appearance of the corrosion layer formed on material *CS*28 (Fig. 11a) is more closely-packed. Interestingly, the corrosion layer formed on the pearlitic materials consisted of two zones: the combination of iron carbide (Fe_3C) and corrosion product on top (Fig. 11b and c). The corrosion product can be a combination of $FeCO_3$, $Fe(OH)_2$, Fe_2O_3, and other Fe^{2+} and Fe^{3+} compounds. In material *CS*65 (Fig. 11b), the porosity of the corrosion layer was high in the vicinity of the sample surface, and decreases through the thickness of the corrosion layer towards the surface of the corrosion layer. However, for material *CS*83 (Fig. 11c), the porosity is almost evenly distributed throughout the thickness until the second layer,

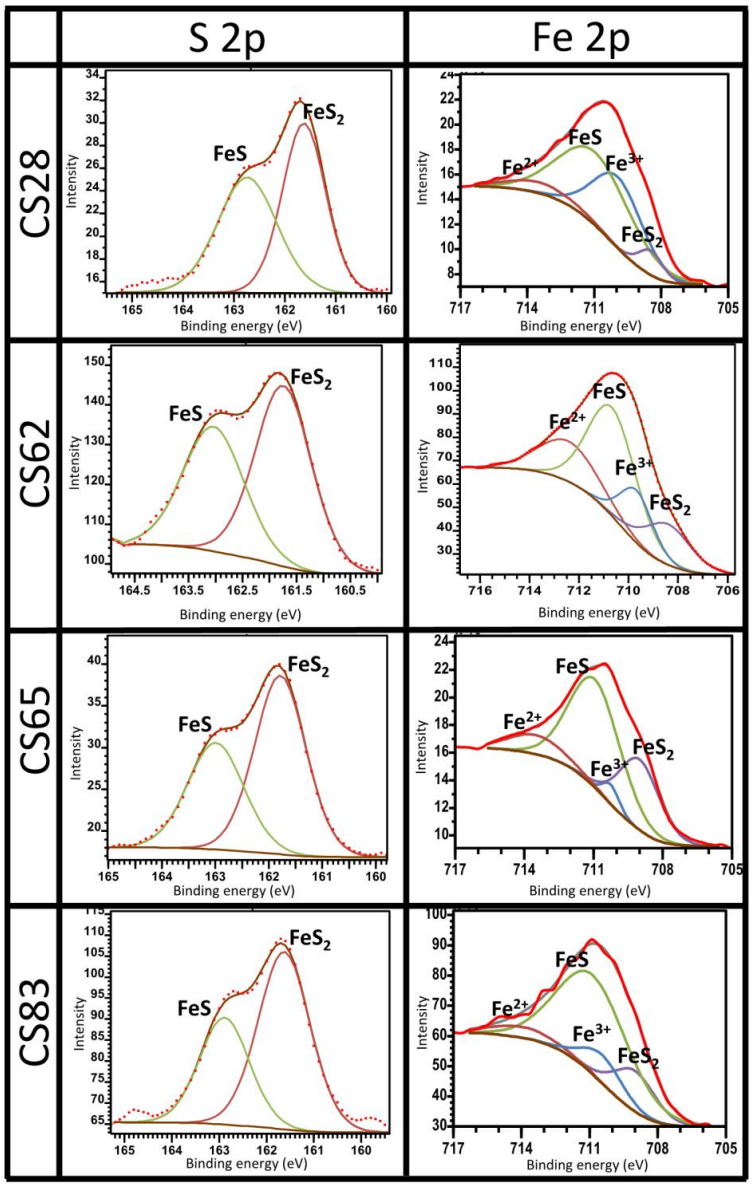

Fig. 9. Regional XPS spectrum of S and Fe from the corrosion layer formed on all materials in the 0.2 bar CO_2/1 mbar H_2S environment.

and its thicker corrosion layer corresponds to a high concentration of porosity and inhomogeneity in the corrosion layer compared with the appearance of the corrosion layer on material *CS*65.

4. Discussion

4.1. CO_2 environment

4.1.1. Corrosion rates

Fig. 3a, and Fig. 4a show the corrosion rate obtained from the LPR measurements and the weight loss data in the CO_2 environment, respectively. A comparison between the different materials showed that the corrosion rate increased with increasing carbon content and cementite phase fraction. As discussed in previous studies [63–66], the presence of cementite and ferrite in carbon steels can accelerate the corrosion rate because cementite is more corrosion-resistant than iron [65]. Therefore, cementite functions as a cathodic site, and a galvanic couple is formed between the cementite region and ferrite matrix, which leads to a high ferrite corrosion rate. The effect of cementite as the cathodic area is reported to be significant in carbon steels with carbon content higher than 0.15 wt% [67]. In this study, all steels had a carbon content higher than 0.15 wt%.

In carbon steels with pearlitic microstructures, such as materials *CS*65 and *CS*83, the cementite phase is arranged in layers. When the

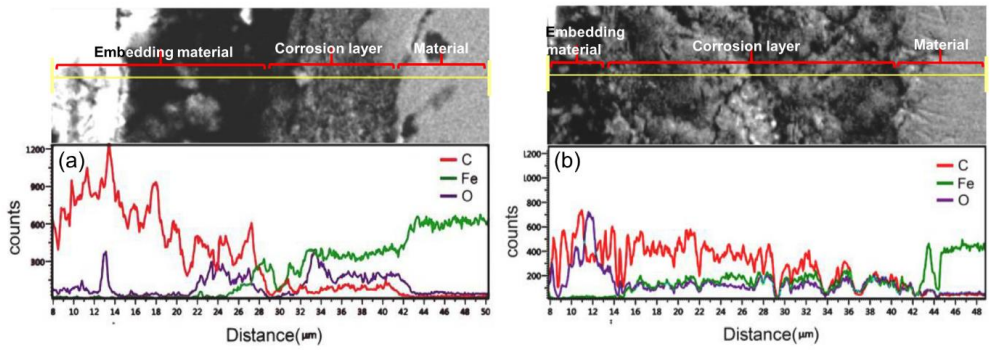

Fig. 10. EDS line Scan through the corrosion layers formed on materials $CS28$ (a) and $CS83$ (b) after exposure to the 0.2 bar CO_2 environment.

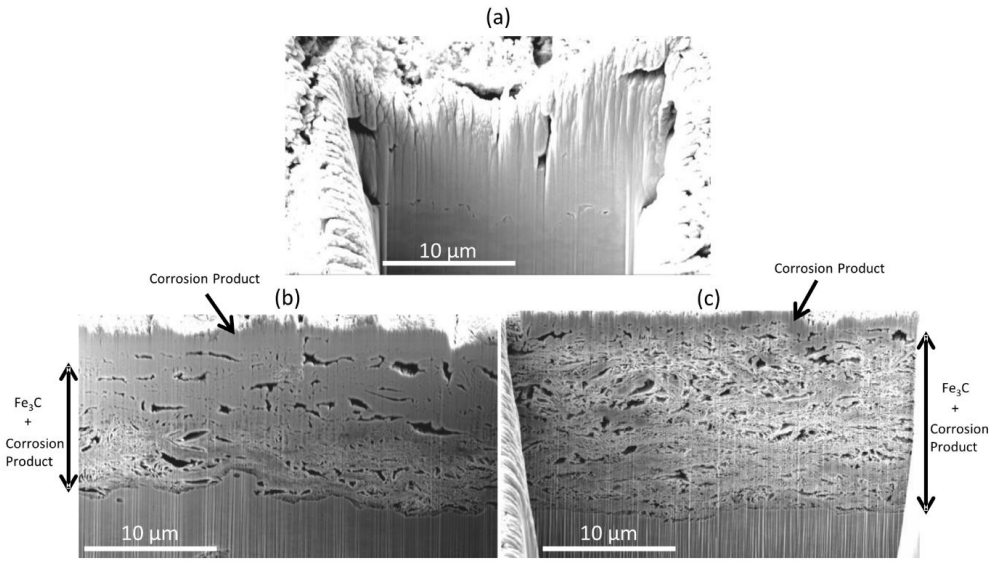

Fig. 11. $FIB-SEM$ micrographs of the corrosion layers formed in the 0.2 bar CO_2 environment on materials $CS28$ (a), $CS65$ (b), and $CS83$ (c). The scale bars show the surface dimensions not the cross-sections.

ferrite phase between the cementite layers is dissolved, the corrosion products can be trapped between the remaining cementite layers to form a physical hindrance between the ferrite and electrolyte, which in turn can decrease the corrosion rate [68]. However, the role of cementite in anchoring the corrosion layer and creating a barrier between the steel surface and the electrolyte can be ineffective in this study because of the low concentration of Fe^{2+}, which causes non-uniform coverage of the corrosion layer. The LPR measurements (Fig. 3a) show that the corrosion rates continuously increased with time, and the curves did not stabilize during the experiments. Furthermore, LPR measurements in the CO_2 environment displayed an increment in the gradient of the curves with increased carbon content, and the lamellar microstructures ($CS65$ and $CS83$) showed the highest slopes. This is attributed to the large area of cementite owing to the increase in carbon content and the galvanic effect of cementite, which is in good agreement with the study performed by Gulbrandsen et al. on $X65$ and $St52$ carbon steels exposed to the CO_2 environment [69].

In addition to the role of cementite in accelerating the corrosion of the ferrite phase, the volume fraction, distribution, and morphology of cementite, can play a crucial role in the corrosion layer formation and consequently affect the corrosion rate [33,52–54]. For instance, the carbon content of material $CS65$ is close to that the carbon content of material $CS62$ (Table 1), while its microstructure is similar to that of material $CS83$'s (since both have the pearlitic microstructure Fig. 2) and its corrosion rate is also more close to the corrosion rate of material $CS83$ than material $CS62$ (Fig. 3a). It can be deduced from this comparison that the microstructure and cementite morphology can have a more critical role in the corrosion rate than the carbon content or cementite fraction. To study the cementite morphology effect on the formation of corrosion products, the XPS, EDS, SEM and FIB results were analyzed.

4.1.2. Chemical characterization of corrosion layers

The XPS results from the top surface of the corrosion layer, as shown in Fig. 8 show that the corrosion products formed in all the studied materials in CO_2 environment contain Fe^{2+} iron compounds. Based on the C $1s$, O $1S$ spectrum analysis, the Fe^{2+} peak is related to the presence of $FeCO_3$. In the analysis of Fe $2p$ spectrum, this peak is at 712–714 eV for all the studied materials, which is as approximately identical to the $FeCO_3$ peak range shown in the XPS Hand book.

However, because the binding energies of different iron compounds in the Fe 2*p* spectrum are very close, it is noted in the previous sections that this peak can also be related to other Fe^{2+} compounds, such as iron hydroxide ($Fe(OH)_2$). $FeCO_3$ is a common corrosion product formed on steels in CO_2 environments. The key factor for the formation of $FeCO_3$ is the supersaturation of Fe^{2+} and CO_3^{2-} ions (Eq. (8)) [70]. In this study, to simulate worst-case corrosion (i.e., when the formation of protective corrosion layers is hindered), the Fe^{2+} concentration was kept low (less than 80 ppm which is a critical point for $FeCO_3$ formation based on the experimental conditions in this study [71]) during the exposure, and this condition is not favorable for $FeCO_3$ scale formation. It is important to emphasize that the *XPS* is a surface analysis technique that exhibits data from the top surface (5–10 nm) of the corrosion layer. Therefore, the presence of $FeCO_3$ in the corrosion layer bulk and between the remaining Fe_3C layers or particles cannot be proven by *XPS* in this study. Nešic et al. [70] discussed in their study that in CO_2 corrosion, the chemical conditions on the surface of the steel can be completely different than the conditions in the bulk solution. Because of the corrosion process, Fe^{2+} ions are produced, whereas H^+ ions are consumed on the surface of the corroding steel. This process results in a higher *pH* at the surface of the metal than in the bulk solution. The inverse dependence of H_2CO_3 reduction on *pH* [72] causes an increase in CO_3^{2-} concentration at the surface because of the high local *pH*. This means that at the surface of the metal, a lower Fe^{2+} concentration is required to reach the saturation limit of $FeCO_3$ [73]. Therefore, $FeCO_3$ can also exist in the bulk of the corrosion layer owing to the different chemical conditions at the surface of the metals.

However, as discussed by Rémazeilles et al. when the Fe^{2+} or carbonate dissolved species concentrations are insufficient, $Fe(OH)_2$ is the most probable compound that can be precipitated as corrosion products [74]. It can be assumed that although the *XPS* analysis of the top layer of the corrosion products demonstrates the presence of $FeCO_3$, because the bulk solution chemistry is not favorable for $FeCO_3$ formation, the corrosion layer can be $FeCO_3$ and/or $Fe(OH)_2$. These are formed between the remaining Fe_3C layers or particles in the bulk of the corrosion layers.

Because all the studied materials contained cementite (Fe_3C) in their microstructures (Table 3), and considering that Fe_3C was not dissolved during the corrosion process because of the galvanic effect between ferrite and cementite, it was expected that the corrosion layer contained the remaining Fe_3C. However, the *XPS* results did not display the Fe_3C peak for any of the studied materials. According to Fig. 11b and c, the first few micrometers of the corrosion layer surface consisted of $FeCO_3$ and/or other Fe^{2+} and Fe^{3+} compounds, and no peaks corresponding to Fe_3C were observed in the *XPS* analysis. Since the *XPS* data were collected from the corrosion layer surface, the inner corrosion layer composition was not detected by this technique. Therefore, the inner corrosion layer that is marked by Fe_3C + corrosion product in Fig. 11b and c is based on the *EDS* line scan (Fig. 10) and the similar results in the previous studies [52,59]. Lopez et al. [35] showed in their study that only after 10 min of Ar^+ sputtering, a new peak indicating the presence of Fe_3C appeared at approximately 283 eV. The *EDS* line scan from the cross-sections of the corrosion layers formed on materials *CS*28 and *CS*83 in Fig. 10 confirms the presence of carbon, iron, and oxygen in the corrosion products. The high carbon intensity in the corrosion products of material *CS*83 can be explained by the presence of a high amount of Fe_3C in its corrosion product. In the corrosion layer of material *CS*28, the oxygen intensity was higher than that of carbon. More $FeCO_3$ and/or hydroxides such as $Fe(OH)_2$ were likely present in the corrosion layer than Fe_3C. This observation is in accordance with the *XPS* results for the O 1*s* and Fe 2*p* regions for each material shown in Table 5 and Table 6, respectively, where the intensity of $FeCO_3$ or Fe^{2+} decreases with increasing carbon content in the materials. To explain this trend, it should be noted that the micro-galvanic corrosion due to the contact between cementite and ferrite was low in material *CS*28 owing to its low cementite fraction, and also in material *CS*62 because of the small contact area between the spherical-shaped cementite and ferrite phase [75]. The high micro-galvanic corrosion in the pearlitic microstructures (materials *CS*65 and *CS*83) was accompanied by high H^+ amounts released between the remaining Fe_3C layers, and led to a lower *pH*. Thus, the conditions for $FeCO_3$ and Fe^{2+} compounds formation were not favorable. Therefore, the $FeCO_3$ and Fe^{2+} compounds intensity was low in pearlitic microstructures that contained high carbon content in this study.

4.1.3. Corrosion layer morphology and thickness

The sample surface/corrosion layer and the corrosion layer/embedding material interfaces (green and red lines, respectively) in material *CS*28 were more uneven and have a rough appearance compared to the other materials (Fig. 6, left column). To explain this difference, the process of corrosion layer formation was considered. In the CO_2 environment, the $FeCO_3$ precipitation process on the carbon steel surface consisted of two steps: nucleation and growth [76]. In the first step, nucleation occurs near the steel surface or in the solution. After nucleation, the $FeCO_3$ grains start to grow, and all Fe^{2+} and CO_3^{2-} ions predominantly participate in the growth process. The nucleation process almost stops at this stage. The original and primary nucleation step can be accelerated if the carbon steel surface has more of the cementite phase, which can provide some points on the surface for ferrous and carbonate ions to nucleate [77,78]. Hence, the high fraction of the cementite phase in materials *CS*62, *CS*65, and *CS*83 provided more nucleation sites for $FeCO_3$ precipitation than material *CS*28. However, the high corrosion rates in materials *CS*62, *CS*65 and *CS*83 led to a high release of Fe^{2+} from the carbon steel surface, which caused a higher nucleation rate. Therefore, it can be inferred that the nucleation rates in materials *CS*62, *CS*65, and *CS*83, were high, and which may have affected the growth rate and caused the precipitation of small particles of $FeCO_3$ [76,79]. The points and areas that can provide favorable nucleation sites on the surface were few in material *CS*28 because of its low cementite phase fraction and therefore, lowered induced nucleation. Consequently, the growth step was more dominant in this material, which created large particles of $FeCO_3$ and large spaces between the $FeCO_3$ particles [76]. The spaces between the $FeCO_3$ particles provided direct contact between the sample surface and solution, resulting in an accelerated Fe dissolution rate and localized corrosion, which gave rise to a bumpy sample surface/corrosion layer interface (green line). The high concentrations of Fe^{2+} and HCO_3^- ions in the localized corrosion areas between the large carbonate grains led to the precipitation of $FeCO_3$ in these areas, and the large spaces between the first precipitated $FeCO_3$ particles were filled [16,80]. The outcome was the rough sample surface/corrosion layer and the consequent corrosion layer/embedding material interfaces in material *CS*28, can be observed in Fig. 6 (green and red lines) (*CS*28) in the CO_2 environment.

The *SEM* images in Fig. 6 show that the thickness of the corrosion layers increased as the carbon content increased. The only exception is material *CS*65 which shows a slightly lower thickness than material *CS*62. The difference between the corrosion layer thicknesses of these two materials is only 2 μm. Because these thicknesses are the average values measured from the two samples for each material, the 2 μm difference can be ignored. However, this difference may be worth being considering in this study because the same trend in the corrosion layer thicknesses was observed in the CO_2/H_2S environment (Fig. 6(right column)). This means that the corrosion layer thickness of material *CS*65 was lower than that of material *CS*62 in both the CO_2 and the CO_2/H_2S environments. The general thickness increase with carbon content in this study can be attributed to the high Fe^{2+} concentration on the surface of the materials with high carbon content, and consequently the increasing corrosion layer accumulation rate with the increase in carbon content, as shown in Fig. 13. In addition, as it can be seen in Fig. 2 which shows the microstructure of the materials, the cementite phase in material *CS*62 is broken lamella or spheroidite, whereas the cementite morphology in materials *CS*65 and *CS*83 is

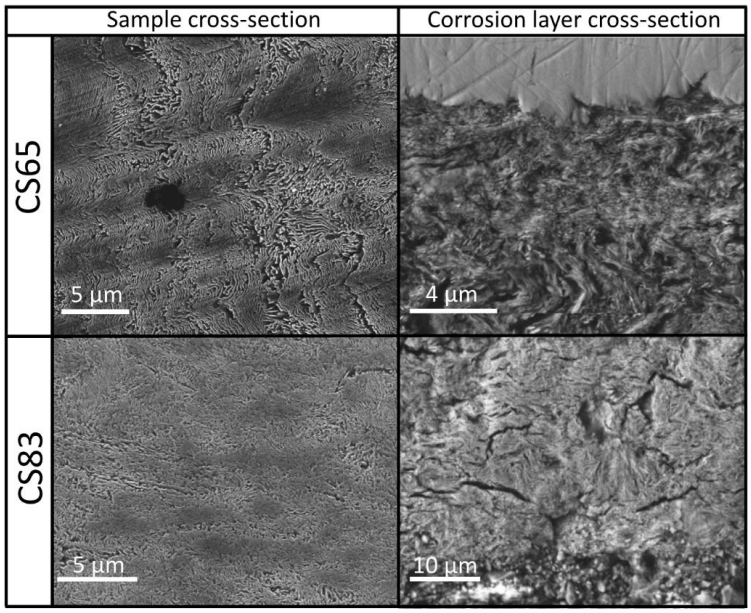

Fig. 12. *SEM* micrographs which show the resemblance of cross-sectional morphologies of the sample microstructure (left column) and the corrosion layer formed on materials *CS*65 and *CS*83 (right column) in the 0.2 bar CO_2 environment.

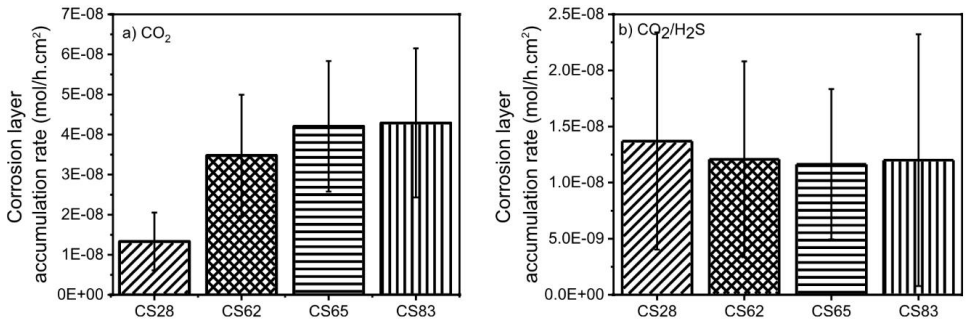

Fig. 13. Corrosion layer accumulation rate for the materials exposed to (a) the 0.2 bar CO_2 environment and (b) the 0.2 bar CO_2/1 mbar H_2S environment for 21 d, respectively. (The columns show the mean value of three tests and the bars represent the standard deviation of the mean value.)

lamellar. These two materials, *CS*65 and *CS*83, had a denser cementite network, which consequently provided more connectable ground for the corrosion products to adhere to the surface and protect it from mechanical breakdown. However, as discussed earlier, the corrosion layer in material *CS*65 was slightly thinner than that in material *CS*62, despite its high corrosion rate and lamellar microstructure. Although material *CS*65 had a lamellar cementite morphology, its microstructure showed that the ferrite areas were larger and connected, whereas small and disconnected ferrite grains constituted the ferritic areas in material *CS*62. A group of small ferrite grains was surrounded by ferrite/cementite grains, and this pattern was repeated throughout the material (Fig. 2). Therefore, material *CS*62 had a more uniform microstructure, which consequently provided a more uniform linking substrate for corrosion products during the corrosion process. In material *CS*65, the connected and big ferrite grains hampered the formation of a uniform remaining Fe_3C network for corrosion product attachment in this material. Consequently, the corrosion layer thickness in this material was lower than that of material *CS*62.

In general, under these study conditions, it seems that the corrosion layers formed in the CO_2 environment were not sufficiently protective to prevent further corrosion; therefore, the high corrosion layer thickness in high-carbon steels did not prevent the corrosion process. Material *CS*28, with the lowest corrosion rate, demonstrated the thinnest layer, whereas the thickest corrosion layer was formed on material *CS*83 which had the highest corrosion rate.

4.1.4. Corrosion layer porosity

Another characteristic of a corrosion layer that can affect the corrosion rate is porosity. As can be observed from the *SEM* images in Fig. 6 (left column), the corrosion layer cross-sections of materials *CS*65 and *CS*83 with the pearlitic microstructure show more porosity than the corrosion layer cross-section of materials *CS*62 and *CS*28. To obtain a clearer image of the corrosion layers porosity, the cross-sections of the corrosion layers of materials *CS*28, *CS*65 and *CS*83, were cut in *FIB* by gallium ions. Based on the *FIB- SEM* images shown in Fig. 11a, material *CS*28 exhibits a compact corrosion layer, whereas materials

*CS*65 and *CS*83 with pearlitic microstructures show porosity in their corrosion layers.

The porous layer formed on materials *CS*65 and *CS*83 with a pearlitic microstructure shown in Fig. 11b and c consist of the remaining Fe_3C lamellae. The hollow spaces between the remaining Fe_3C lamellae are filled with corrosion products in some areas, but there is still a large fraction of hollow spaces between the remaining lamellae, which gives rise to a porous film. There is a resemblance between the corrosion layer morphology and the cross-sectional microstructure of the bare samples in materials *CS*65 and *CS*83 with lamellar microstructures, as shown in Fig. 12. This resemblance clearly shows that the Fe_3C layers remained on the steel surface after the mid-ferrite phases were dissolved, and the corrosion layer adopted almost the same morphology as the original material microstructures. Therefore, the high porosity observed in the corrosion layer of materials *CS*65 and *CS*83 was due to their lamellar microstructure and the presence of remaining Fe_3C in the corrosion layer, as well as the spaces between the remaining Fe_3C layers not being completely filled with corrosion products due to the low Fe^{2+} concentration in the bulk solution in this study. A porous corrosion layer cannot effectively prohibit the permeation of ions at solution [81]. The *LPR* corrosion rate curves in Fig. 3a shows that the corrosion rates increase continuously with time for all materials, and the curve gradient increases with the corrosion layer porosity. That is, the corrosion rate increases faster for materials *CS*65 and *CS*83 which presented more porosity in their corrosion layers, than for materials *CS*28 and *CS*62.

During the first stages of corrosion, when the uncovered sample surface was in contact with the CO_2-containing solution, the micro-galvanic couple of Fe and Fe_3C, and consequently, the remaining Fe_3C, lead to the formation of a corrosion layer that grew with a similar morphology and structure as the sample microstructure. As Crolet et al. [82, 83] noted, after the first stage of corrosion, an empty Fe_3C formed and internal acidification due to micro-galvanic coupling impeded the precipitation of $FeCO_3$ in contact with the carbon steel surface. In this case, the corrosion layer was not protective even if the outer layer was obstructed [84]. The unprotective Fe_3C + corrosion product layer is shown in Fig. 11b and c for materials *CS*65 and *CS*83, respectively. However, in material *CS*65 this layer was more porous in the vicinity of the carbon steel surface because the acidification prevents the corrosion product precipitation in this region. At a further distance from the interface, the remaining cementite layers were partially filled with corrosion product, and far from the top of the corrosion layer, Fe^{2+} and Fe^{3+} compounds covered the surface. However, in material *CS*83, the small interlamellar spaces compared with material *CS*65 (Table 3) gave rise to more hydrogen occlusion [85]. Because the H^+ ions can hamper the corrosion product precipitation by decreasing the pH [86–89], the unfilled pores and hollow spaces between the remaining Fe_3C layers can be observed all over the corrosion layer cross-section. Hence, the appearance of the cross-sectional morphology and porosity of the corrosion layer was more uniform compared to material *CS*65.

4.2. Proposed mechanisms for the corrosion layer formation in CO_2 environment

A schematic is shown in Fig. 14 to clarify the cementite morphology role in the corrosion layer formation mechanism in the studied materials. As mentioned previously, material *CS*28 with dispersed spherical cementite offered few favorable sites on the surface for $FeCO_3$ nucleation, and the low $FeCO_3$ nucleation rate resulted in the formation of large $FeCO_3$ grains and large spaces between them (Fig. 14 *CS*28 (a) and (b)). The sample surface between the $FeCO_3$ grains corroded at a higher rate than that at the other sites. The resultant high Fe^{2+} concentration in these corroded areas led to the formation of $FeCO_3$, which filled the spaces between the first precipitated $FeCO_3$ layers. The result was a rough metal surface/corrosion layer interface, and the consequent rough corrosion layer/embedding material interface (Fig. 14 *CS*28 (c) and Fig. 6).

In material *CS*62, the uniform microstructure was due to the spherical and broken lamella cementite particles, which were evenly distributed throughout the material, and the repeated surrounding ferrite regions which were several microns in size. As shown in the schematic in Fig. 14 *CS*62 (a), this microstructure provided more sites for $FeCO_3$ nucleation. The micro-galvanic effect between cementite and ferrite caused ferrite phase dissolution. Because the cementite phase consisted of spherical and broken lamella, dissolution of the ferrite phase caused the cementite phase to be released and dissolved into the electrolyte. Only a small fraction of cementite remained on the surface, and corrosion product formed between the remaining cementite Fig. 14 *CS*62 (b). It has been previously mentioned that the corrosion layer formed in the CO_2 environment showed an inefficient protectiveness and, therefore, the sample surface corroded continuously during the test. This gave rise to a porous corrosion layer. At a distance from the metal surface towards the corrosion layer and electrolyte interface, a compact layer of $FeCO_3$ formed (Fig. 14 *CS*62 (c)).

The microstructure of material *CS*65 consisted of lamellar cementite phase and connected ferrite regions. Two distinct features in this material microstructure contributed to the morphology, thickness, and surface roughness of the corrosion layer formation: pearlite colonies and a connected ferrite phase. As discussed, the ferrite regions are favorable places for corrosion and dissolution sooner than the pearlite regions. This resulted in the formation of a non-uniform and uneven corroded surface, as shown in Fig. 14 *CS*65 (b). This can lead to the break down of the remaining Fe_3C and formed $FeCO_3$, which caused the formation of a rough corrosion layer, Fig. 14 *CS*65 (c).

Material *CS*83 had the highest carbon content and cementite fraction among the studied materials. The pearlite colonies with very small and confined ferrite regions constituted the material *CS*83 microstructure, and its interlamellar spacing was lower than of material *CS*65 (Fig. 14 *CS*83 (a) and Table 3). Material *CS*83 exhibited a more uniform microstructure than material *CS*65. The micro-galvanic effect between ferrite and cementite led to the dissolution of ferrite and a connected stable network of the remaining Fe_3C in the formed corrosion layer. The high micro-galvanic corrosion owing to the high cementite fraction in this material was accompanied by a high H^+ release, which led to a low pH and high acidity between the remaining Fe_3C layers. In addition, the small interlamellar spacing, which led to a slow process of hydrogen ion diffusion from the interlamellar spaces towards the electrolyte, gave rise to high acidity at this material surface. This resultant acidity was not a favorable condition for corrosion product formation, and the high porosity was the result of incomplete coverage of corrosion product between the Fe_3C layers (Fig. 14 *CS*83 (b) and (c)). A compact corrosion layer of $FeCO_3$ was formed on top of the corrosion layer/electrolyte interface.

4.3. CO_2/H_2S environment

The corrosion behavior of carbon steels in H_2S-containing solutions has been extensively studied, and the results revealed that H_2S accelerates both anodic iron dissolution and cathodic hydrogen evolution in most cases [6,18,39,90–96]. However, it has been reported that under low concentrations of H_2S (up to approximately 0.908 mbar) and special conditions (pH range of 3–5, and long exposure time, i.e., 2 h or more), H_2S has a strong inhibiting effect on the corrosion of iron [18,97,98]. As is shown in Fig. 3b, the addition of 1 mbar H_2S induced a significant reduction in the corrosion rate by one order of magnitude compared to the CO_2 environment. This retardation was first mentioned by Shoesmith et al. [99] as the effect of the very rapid formation of a thin FeS_{ads} film in a solid-state process by the direct reaction of H_2S and Fe. This film can displace the adsorbed H_2O and OH^- from the carbon steel surface and affect the surface double layer [100], which in turn slows the kinetics of the electrochemical reactions including

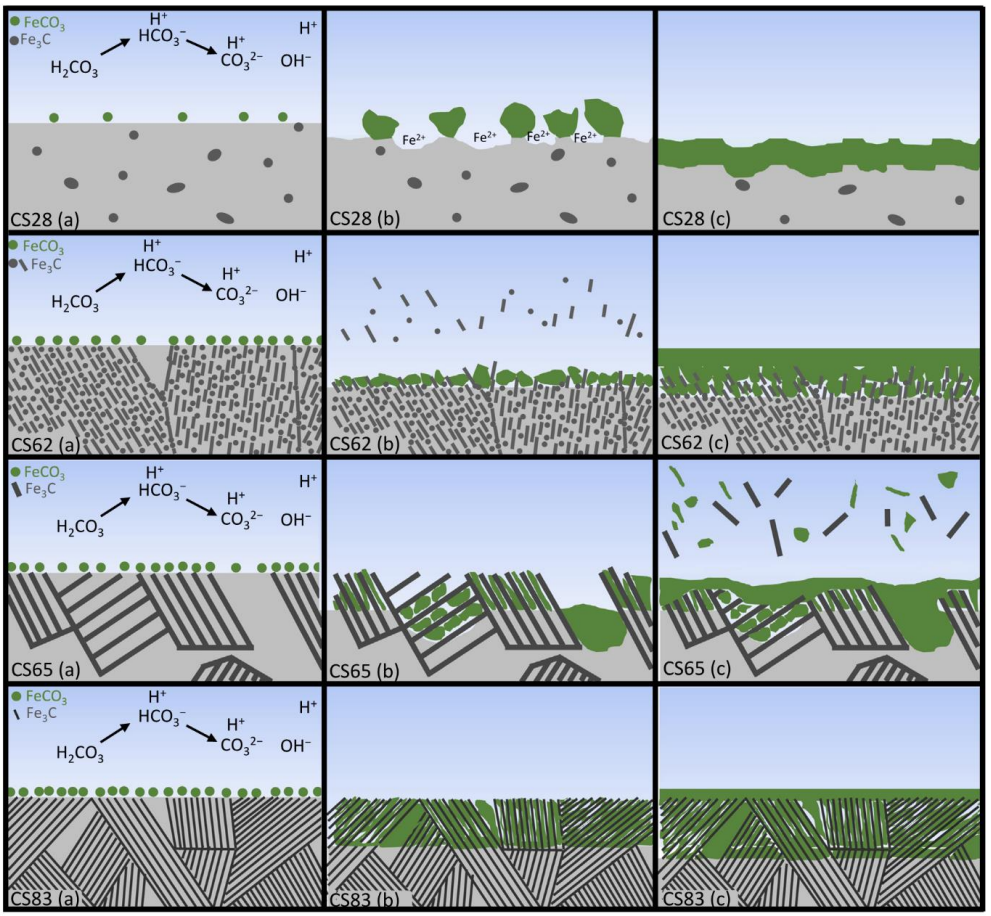

Fig. 14. Schematic representations of the evolution mechanism of $FeCO_3$ corrosion layer in the 0.2 bar CO_2 environment for all materials.

anodic Fe dissolution, H_2O reduction (by an order of magnitude), and HCO_3^- reduction (by a factor of 3) [101].

Previous studies have shown that as long as thermodynamics permit, by considering the kinetics formation of different FeS phases, the initial phase that forms on the carbon steel surface in a CO_2/H_2S environment is mackinawite (FeS) in a direct solid-state reaction between H_2S and the carbon steel surface [102–104]. The carbon steel surface reacts with the dissolved H_2S and $FeHS^+_{ads}$ is formed on the surface. This ion directly participates in making the mackinawite film (*eq*.9) [99,105]. $FeHS^+_{ads}$ can also migrate from the carbon steel surface towards the solution. The formation rate of mackinawite is much faster than $FeHS^+_{ads}$ migration and dissolution, and it can be formed even when the bulk solution is under the saturation level [106]. Pessu et al. [107] showed that the corrosion potential increases quickly at 1000 *ppm* of H_2S compared with high H_2S concentrations (10000 and 1000000 *ppm*) in a CO_2/H_2S mixed solution, whereas after 60 *h*, it starts to decrease towards a more negative potential. They concluded that a fast process of iron sulfide formation occurred on the carbon steel surface at low H_2S concentration (1000 *ppm*, which is almost the same as the H_2S concentration used in the present study). As mentioned previously, the immediate drop in the *LPR* corrosion rates in Fig. 3b can be attributed to the fast formation of the FeS layer at a low concentration of H_2S used in the present study. According to Woollam et al. [71] who investigated the effect of various parameters on a thermodynamically stable film in the presence of CO_2 and H_2S, the formation of mackinawite is favored under the present study test conditions. $FeCO_3$ does not have the same formation kinetics as mackinawite, but can be formed within the mackinawite layer through the diffusion of H_2CO_3. Because H_2S reacts very quickly with Fe^{2+} ions diffusing from the carbon steel surface towards the solution, it is not expected that H_2S will diffuse through the developing layer. However, H_2CO_3 which is slow to react, can diffuse through the layer and react with Fe^{2+} ions to form $FeCO_3$ or other Fe^{2+} compounds [108]. As discussed in the previous section, the Fe_3C residues on the corroding carbon steel surface can significantly improve the mechanical attachment of the corrosion product to the metal surface. Bonaventura et al. [109] showed that even $FeCO_3$ formation could be prevented if the remaining Fe_3C layer is damaged. Therefore, because of the significant decrease in the corrosion rate in the presence of H_2S and the fast formation of the FeS layer, the corrosion process does not leave a large amount of Fe_3C on the surface, which consequently leads to a substantial reduction in the corrosion layer thickness in comparison with the layer thicknesses in the CO_2 environment (Fig. 6).

The *XPS* results (Fig. 9) confirm the formation of two iron sulfides which are FeS (mackinawite) and FeS_2 (pyrite) and Fe^{2+} and Fe^{3+} compounds, such as iron oxide (Fe_2O_3) in the CO_2/H_2S environment in

the corrosion layers of all the studied materials. Based on the relative intensities in Table 7, it can be seen that the iron sulfides intensities in pearlitic microstructures (materials *CS*65 and *CS*83) are high, whereas the sum of Fe^{2+} and Fe^{3+} compounds is higher in the corrosion layers of materials *CS*28 and *CS*62. Because mackinawite and pyrite form a more protective surface layer [110], the corrosion rates of materials *CS*65 and *CS*83, which have layers rich in iron sulfide species, are low in the CO_2/H_2S environment (during the initial hours of exposure for material *CS*65, and until the end of the exposure for material *CS*83). Material *CS*65 showed a slightly higher intensity of iron sulfide species than material *CS*83; however, it showed a higher corrosion rate and a continuous increase in the corrosion rate during the test. The role of the microstructure on the corrosion layer morphology and thickness, which in turn results in its unusual corrosion behavior, will be discussed in the following paragraphs. This behavior is discussed here from the perspective of the corrosion layer composition. As observable in Table 7, the relative intensity of pyrite is 29.2 and 15.7 in materials *CS*65 and *CS*83, respectively. The formation of pyrite is accompanied by the evolution of hydrogen, as identified using mass spectroscopy by Taylor et al. [111]. Hydrogen can be produced as follows:

$$FeS + H_2S \rightarrow FeS_2 + H_2 \quad (16)$$

In fact, pyrite formation on steels in an aqueous H_2S solution produces disulfide anions at the anodic sites and hydrogen at the cathodic sites [112,113]. As such, the reaction between the generated S_2^{2-} and dissolved Fe^{2+} leads to the crystallization of pyrite at the anodic sites [111]:

$$2HS^- \rightarrow S_2^{2-} + 2H^+ + 2e^- \quad (17)$$

$$2H^+ + 2e^- \rightarrow H_2 \quad (18)$$

$$Fe^{2+} + S_2^{2-} \rightarrow FeS_2 \quad (19)$$

The formation mechanism of pyrite which is accompanied by a cathodic reaction, can boost the corrosion rate [114]; therefore, the high relative intensity of pyrite in material *CS*65 in comparison with material *CS*83 can be a reason for its high and increased corrosion rate. Rickard [115] indicated that pyrite generally forms approximately after one week. The *LPR* curve of material *CS*65 in Fig. 3b shows a small change in the gradient at approximately 152 *h* (almost one week). After this point, the corrosion rate rises at an increased rate, which can be attributed to the formation of pyrite in this material. The pyrite proportion in the other studied materials was not sufficiently high to cause a change in the corrosion rate gradient.

According to Fig. 3b, the corrosion layer formed in the CO_2/H_2S solution shows better protection characteristics than the layer formed in the CO_2 environment. The *LPR* corrosion rate curves show that the corrosion layer formed on material *CS*28 reaches its peak protectiveness after 80 h, whereas the peak protectiveness is obtained after 57, 54, and 41 h, for materials *CS*62, *CS*65, and *CS*83, respectively. This trend shows that the corrosion layer protectiveness increased with an increase in the carbon content and cementite phase fraction. After the maximum protectiveness was reached, the corrosion rate stabilized for material *CS*28, whereas there was a slight increase in the corrosion rates of materials *CS*62 and *CS*83, and an increased increment was observed for material *CS*65 (Fig. 3b). The corrosion rates in materials *CS*62 and *CS*65 were the same between 85 and 152 h, however after that, material *CS*65 exhibited a considerably higher corrosion rate than material *CS*62. Because the carbon content and the cementite fraction were very close in materials *CS*62 and *CS*65, it can be inferred that the carbon steel microstructure was a pertinent factor in controlling the corrosion rate and corrosion layer protectiveness. Anyanwu et al. [37] reported the preferential development of an iron sulfide layer above pearlite regions in a ferritic/pearlitic microstructure. They showed that a thin and continuous layer of iron sulfide, which was formed on the pure iron material in the CO_2/H_2S environment with 0.1 bar H_2S was loosely attached in comparison with the iron sulfide layer formed on the ferrite/pearlite sample. Bai et al. [116] reported a high precipitation rate of the iron sulfide layer on the pearlite regions in a ferrite/pearlite microstructure exposed to an H_2S environment. Their studies showed that the iron sulfide layer formed on the ferrite/pearlite microstructure was more protective than the layer formed on a bainitic microstructure. In the H_2S environment, hydrogen ion (H^+) reduction and hydrogen sulfide reduction reactions occurred in the cementite phase as cathodic reactions, owing to the local micro-galvanic cell between the ferrite and cementite in the pearlitic microstructure. These cathodic reactions caused a decrease in the hydrogen ion concentration. The high iron dissolution in the ferrite phase, along with the reduced hydrogen ion concentration and the consequently raised pH, generated favorable conditions for iron sulfide formation above the pearlite regions. Furthermore, the presence of the remaining iron carbide, notwithstanding its low amount, promoted the structural attachment of the iron sulfide layer. Despite the pearlitic microstructure of material *CS*65, it showed a higher corrosion rate than material *CS*62 with a spheroidite microstructure. Kim et al. [34] investigated the effects of the pearlitic and bainitic microstructures on sulfide scale formation. They concluded that the distance from ferrite to cementite, which was 10 μm in the pearlite/ferrite microstructure, could lead to a high *pH* gradient on the surface of the sample, whereas it was unlikely for a bainite microstructure with few μm or less between ferrite and cementite, resulting in *pH* gradient. In the studied materials with pearlitic microstructures, *CS*65 and *CS*83, the lamellar spaces were at the nanoscale; therefore, we can consider that when the *pH* above the cementite phase increases, the entire pearlitic area experiences an increased *pH*. In the microstructures of these two materials, there are pure ferrite grains between the pearlite colonies, which can also cause a *pH* gradient. In material *CS*83, the size of the ferritic grains between the ferrite/cementite colonies was a few μm (less than 10 μm), and the *pH* gradient formation was improbable. In material *CS*65, the ferrite grain size was approximately 10 μm or more, and the *pH* gradient that occurred on the material surface resulted in the formation of an uneven iron sulfide film. Moreover, the connected ferrite grains impeded the formation of a uniform remaining Fe_3C structure for iron sulfide attachment in this material. In Fig. 15, a hollow space within the remaining Fe_3C network is marked on the corrosion layer of the material *CS*65. This discontinuity is observed less in materials *CS*83 and *CS*62. The uniform cementite dispersion on these two materials provided a more uniform Fe_3C structural base for the attachment of the protective iron sulfide film. Therefore, material *CS*65 exhibited a higher corrosion rate (Fig. 3b and Fig. 4b).

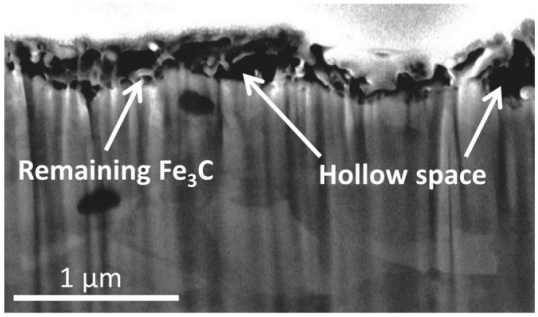

Fig. 15. *SEM* micrograph of the morphology of the corrosion layer formed on material *CS*65 in the 0.2 bar CO_2/1 mbar H_2S environment.

According to Fig. 6, material *CS*28, with the lowest carbon content, displays the thinnest corrosion layer among the studied materials. This

material had the lowest fraction of Fe_3C. However, Fig. 13b shows that all materials have almost identical corrosion layer accumulation rate, considering the large error bars. This implies that the corrosion layer formed on material $CS28$ was more compact than that on other materials, whereas the loose attachment of the corrosion layer of this material to the metal substrate, owing to the less connected Fe_3C network, can be a reason for its low thickness. The other three high-carbon steel materials, $CS62$, $CS65$, and $CS83$, exhibited a porous corrosion layer because of the presence of the remaining Fe_3C in the layer.

5. Conclusions

Corrosion tests in the modified $ASTM\ D1141$-90 electrolyte in the 0.2 bar CO_2 and 0.2 bar CO_2/1 mbar H_2S environments were performed on four carbon steels with different microstructures for 21 d. After exposure, the corrosion layers were characterized with $SEM-EDS$, FIB, and XPS to reveal the effect of microstructures on layer formation and the corresponding corrosion properties. The results revealed the following:

- The corrosion layer formed on all materials in the CO_2/H_2S environment provided significant protection, in contrast to the layer formed in the CO_2 environment.
- By comparing the behavior of different carbon steels, it can be observed that with increasing carbon content and cementite phase fraction, the corrosion rate increased in the CO_2 environment while no special trend was observed in the CO_2/H_2S environment.
- Despite the thick corrosion layers formed on materials with high carbon content and cementite fraction in the CO_2 environment, their protectivity was insufficient to prevent the high corrosion rates which were escalated by the micro-galvanic effect. This was due to the high porosity observed in their corrosion layers. The corrosion rate of the material $CS65$ with a ferritic/pearlitic microstructure was higher than the material $CS62$ with a spheroidite microstructure owing to the more prominent micro-galvanic effect in lamellar microstructures.
- After the materials in the CO_2/H_2S environment reached their maximum protectiveness, the corrosion rate of material $CS28$ with the lowest carbon content, stabilized, while there was a slight increase in the corrosion rates for materials $CS62$ (spheroidite microstructure) and $CS83$ (lamellar microstructure). The material $CS65$ (lamellar microstructure with connected ferrite phase) demonstrated a high increase until the end of the test. The higher proportion of pyrite in the corrosion layer of the material $CS65$ in comparison with other materials can be a reason for the higher corrosion rate experienced by this material in the CO_2/H_2S environment.
- In the CO_2 environment, the corrosion layers contained the remaining Fe_3C, and the porosity between the Fe_3C layers or particles was partially filled by the corrosion products. EDS analysis showed the presence of iron, carbon and oxygen elements in the corrosion products.
- The XPS analysis of the top surface of corrosion layers indicated that all corrosion products in both environments contained Fe^{2+} and Fe^{3+} related compounds such as ferric oxide regardless of their microstructures.
- It was found from XPS results that increasing the carbon content, particularly in ferritic/pearlitic microstructures, the proportions of Fe^{2+} compounds decreased and the proportions of the Fe^{3+} related compounds increased.

CRediT authorship contribution statement

Shabnam Karimi: Conceptualization, Data curation, Investigation, Methodology, Visualization, Writing – original draft, Writing – review & editing. **Iman Taji:** Conceptualization, Data curation, Investigation, Methodology, Writing – review & editing. **Tarlan Hajilou:** Conceptualization, Data curation, Investigation, Methodology, Writing – review & editing. **Simona Palencsár:** Conceptualization, Data curation, Investigation, Methodology, Writing – review & editing. **Arne Dugstad:** Conceptualization, Data curation, Investigation, Methodology, Writing – review & editing. **Afrooz Barnoush:** Funding acquisition, Supervision, Writing – review & editing. **Kim Verbeken:** Supervision, Writing – review & editing. **Tom Depover:** Supervision, Writing – review & editing. **Roy Johnsen:** Conceptualization, Funding acquisition, Supervision, Writing – review & editing.

Declaration of competing interest

The authors declare the following financial interests/personal relationships which may be considered as potential competing interests: Shabnam Karimi reports financial support was provided by Norwegian University of Science and Technology.

Data availability

Data will be made available on request.

Acknowledgments

This work was performed as part of the KPN project "Environmental Cracking of Flexible Pipe Armour Wires", Research Council of Norway project no. 280760 within the $PETROMAKS$ 2 program. The authors would like to thank the following project participants for financial and technical support: The Research Council of Norway, Equinor, Norway, Shell, Chevron, Petrobras, Norway, *OKEA*, Norway, Technip*FMC*, *NOV*, Baker Hughes, Norway and 4Subsea, Norway.

References

[1] Y. Bai, Q. Bai, Subsea Pipelines and Risers, Elsevier, 2005.
[2] A. Rubin, S. Overby, T.S. Nielsen, M.H. Haarh, J. Gudme, Corrosion rates of carbon steel in confined environments, in: Corrosion 2012, OnePetro, 2012.
[3] C. Taravel-Condat, N. Desamais, Qualification of high strength carbon steel wires for use in specific annulus environment of flexible pipes containing CO_2 and H_2S, in: International Conference on Offshore Mechanics and Arctic Engineering, Vol. 47489, 2006, pp. 585–591.
[4] P.C. Singer, W. Stumm, The solubility of ferrous iron in carbonate-bearing waters, J.-Am. Water Works Assoc. 62 (3) (1970) 198–202.
[5] I. Shabalov, Y. Matrosov, A. Kholodnyi, M. Matrosov, V. Velikodnev, Effect of hydrogen sulfide-containing media on pipe steels, in: Pipeline Steels for Sour Service, Springer, 2019, pp. 1–28.
[6] H. Vedage, T.A. Ramanarayanan, J. Mumford, S. Smith, Electrochemical growth of iron sulfide films in H_2S-saturated chloride media, Corrosion 49 (2) (1993) 114–121.
[7] W. Liu, S.-L. Lu, Y. Zhang, Z.-C. Fang, X.-M. Wang, M.-X. Lu, Corrosion performance of 3% Cr steel in CO_2-H_2S environment compared with carbon steel, Mater. Corros. 66 (11) (2015) 1232–1244.
[8] Y. Wang, B. Wang, S. He, L. Zhang, X. Xing, H. Li, M. Lu, Unraveling the effect of H_2S on the corrosion behavior of high strength sulfur-resistant steel in $CO_2/H_2S/Cl$- environments at ultra high temperature and high pressure, J. Nat. Gas Sci. Eng. (2022) 104477.
[9] J. Hesketh, E. Dickinson, M. Martin, G. Hinds, A. Turnbull, Influence of H_2S on the pitting corrosion of 316L stainless steel in oilfield brine, Corros. Sci. 182 (2021) 109265.
[10] J. Sardisco, W.B. Wright, E. Greco, Corrosion of iron in on H_2S-CO_2-H_2O system: corrosion film properties on pure iron, Corrosion 19 (10) (1963) 354t–359t.
[11] T. Murata, R. Matsuhashi, T. Taniguchi, K. Yamamoto, The evaluation of H_2S containing environments from the viewpoint of OCTG and linepipe for sour gas applications, in: Offshore Technology Conference, OnePetro, 1979.
[12] P. Narayan, J. Anderegg, C. Chen, An ESCA study of Iron Sulfidation in H_2S, J. Electron Spectrosc. Relat. Phenom. 27 (3) (1982) 233–242.

[13] S. Smith, E. Wright, Prediction of minimum H_2S levels required for slightly sour corrosion, Tech. rep., NACE International, Houston, TX (United States), 1994.

[14] R.A. Berner, Stability fields of iron minerals in anaerobic marine sediments, J. Geol. 72 (6) (1964) 826–834.

[15] J. Kvarekval, R. Nyborg, M. Seiersten, Corrosion product films on carbon steel in semi-sour CO_2/H_2S environments, in: CORROSION 2002, OnePetro, 2002.

[16] S. Zhang, Y. Li, B. Liu, L. Mou, S. Yu, Y. Zhang, X. Yan, Understanding the synergistic effect of CO_2, H_2S and fluid flow towards carbon steel corrosion, Vacuum 196 (2022) 110790.

[17] P. Sui, C. Sun, Y. Hua, J. Sun, Y. Wang, The influence of flow rate on corrosion behavior of $X65$ carbon steel in water-saturated supercritical CO_2/H_2S system, in: CORROSION 2019, OnePetro, 2019.

[18] J. Sardisco, R. Pitts, Corrosion of iron in an H_2S-CO_2-H_2O system composition and protectiveness of the sulfide film as a function off pH, Corrosion 21 (11) (1965) 350–354.

[19] W.F. Rogers, A. Rowe, 3. Corrosion effects of hydrogen sulphide and carbon dioxide in oil production, in: 4th World Petroleum Congress, OnePetro, 1955.

[20] S.P. Ewing, Electrochemical studies of the hydrogen sulfide corrosion mechanism, Corrosion 11 (11) (1955) 51–55.

[21] E. Abelev, J. Sellberg, T. Ramanarayanan, S. Bernasek, Effect of H_2S on Fe corrosion in CO_2-saturated brine, J. Mater. Sci. 44 (22) (2009) 6167–6181.

[22] F. Shi, L. Zhang, J. Yang, M. Lu, J. Ding, H. Li, Polymorphous FeS corrosion products of pipeline steel under highly sour conditions, Corros. Sci. 102 (2016) 103–113.

[23] R. Souza, B. Santos, M. Gonçalves, E.M. Júnior, T. Simões, J. Oliveira, G. Vaz, L. Caldeira, J. Gomes, A. Bueno, The role of temperature and H_2S (thiosulfate) on the corrosion products of API $X65$ carbon steel exposed to sweet environment, J. Pet. Sci. Eng. 180 (2019) 78–88.

[24] R. Elgaddafi, A. Naidu, R. Ahmed, S. Shah, S. Hassani, S.O. Osisanya, A. Saasen, Modeling and experimental study of CO_2 corrosion on carbon steel at elevated pressure and temperature, J. Nat. Gas Sci. Eng. 27 (2015) 1620–1629.

[25] B. Pound, G. Wright, R. Sharp, The anodic behavior of iron in hydrogen sulfide solutions, Corrosion 45 (5) (1989) 386–392.

[26] D.W. Shannon, Role of chemical components in geothermal brine on corrosion, CORROSION/78, Paper (57) (1978).

[27] C. Ding, K.-w. Gao, C.-f. Chen, Effect of Ca^{2+} on CO_2 corrosion properties of $X65$ pipeline steel, Int. J. Miner. Metall. Mater. 16 (6) (2009) 661–666.

[28] Z. Wang, L. Zhang, Z. Zhang, M. Lu, Combined effect of pH and H2S on the structure of passive film formed on type 316L stainless steel, Appl. Surf. Sci. 458 (2018) 686–699.

[29] S.J. Kim, H.G. Jung, G.T. Park, K.Y. Kim, Effect of Cu and Ni on sulfide film formation and corrosion behavior of pressure vessel steel in acid sour environment, Appl. Surf. Sci. 313 (2014) 396–404.

[30] S. Koh, J. Lee, B. Yang, K. Kim, Effect of molybdenum and chromium addition on the susceptibility to sulfide stress cracking of high-strength, low-alloy steels, Corrosion 63 (3) (2007) 220–230.

[31] H. Inagaki, M. Tanimura, I. Matsushima, T. Nishimura, Effect of Cu on the hydrogen induced cracking of the pipe line steel, Trans. Iron Steel Inst. Japan 18 (3) (1978) 149–156.

[32] C. Palacios, J. Shadley, Characteristics of corrosion scales on steels in a CO_2-saturated $NaCl$ brine, Corrosion 47 (2) (1991) 122–127.

[33] A. Dugstad, H. Hemmer, M. Seiersten, Effect of steel microstructure on corrosion rate and protective iron carbonate film formation, Corrosion 57 (04) (2001).

[34] S.J. Kim, J.H. Park, K.Y. Kim, Effect of microstructure on sulfide scale formation and corrosion behavior of pressure vessel steel in sour environment, Mater. Charact. 111 (2016) 14–20.

[35] D. Lopez, W.d. Schreiner, S. De Sánchez, S. Simison, The influence of carbon steel microstructure on corrosion layers: an XPS and SEM characterization, Appl. Surf. Sci. 207 (1–4) (2003) 69–85.

[36] M. Ueda, H. Takabe, Effect of environmental factor and microstructure on morphology of corrosion products in CO_2 environments, Tech. rep., NACE International, Houston, TX (United States), 1999.

[37] E. Anyanwu, B. Brown, M. Singer, Effect of iron carbide on the morphology and protectiveness of iron sulfide layer, in: CORROSION 2020, OnePetro, 2020.

[38] F. Farelas, B. Brown, S. Nešić, Iron carbide and its influence on the formation of protective iron carbonate in CO_2 corrosion of mild steel, in: CORROSION 2013, OnePetro, 2013.

[39] H.-H. Huang, W.-T. Tsai, J.-T. Lee, Electrochemical behavior of the simulated heat-affected zone of $A516$ carbon steel in H_2S solution, Electrochim. Acta 41 (7–8) (1996) 1191–1199.

[40] A.M. Zimer, E.C. Rios, P.d.C.D. Mendes, W.N. Gonçalves, O.M. Bruno, E.C. Pereira, L.H. Mascaro, Investigation of $AISI$ 1040 steel corrosion in H_2S solution containing chloride ions by digital image processing coupled with electrochemical techniques, Corros. Sci. 53 (10) (2011) 3193–3201.

[41] E.S. Skilbred, M. Kappes, M. Iannuzzi, R. Johnsen, Hydrogen uptake and diffusivity in steel armor wires with different chemical composition, carbide distribution, grain size, and degree of deformation, Mater. Corros. (2021).

[42] S. Karimi, I. Taji, T. Hajilou, A. Barnoush, R. Johnsen, Evaluation of the cementite morphology influence on the hydrogen induced crack nucleation and propagation path in carbon steels, Int. J. Hydrogen Energy 47 (30) (2022) 14121–14129.

[43] American Society for Testing and Materials, Standard Practice for the Preparation of Substitute Ocean Water, ASTM International, 2013.

[44] S. Navabzadeh Esmaeely, Y.-S. Choi, D. Young, S. Nešić, Effect of calcium on the formation and protectiveness of iron carbonate layer in CO_2 corrosion, Corrosion 69 (9) (2013) 912–920.

[45] M. Stern, A.L. Geary, Electrochemical polarization: I. a theoretical analysis of the shape of polarization curves, J. Electrochem. Soc. 104 (1) (1957) 56.

[46] M. Stern, A method for determining corrosion rates from linear polarization data, Corrosion 14 (9) (1958) 60–64.

[47] G. Astm, Standard test method for conducting potentiodynamic polarization resistance measurements, in: Annual Book of ASTM Standards, Vol. 3, 2009, pp. 237–239.

[48] M. Stern, E. Weisert, Experimental observations on the relation between polarization resistance and corrosion rate, in: Proc. Am. Soc. Test. Mater, vol. 59, 1959, p. 1280.

[49] American Society for Testing and Materials (Filadelfia, Pennsylvania), ASTM G1-03: Standard Practice for Preparing, Cleaning, and Evaluating Corrosion Test Specimens, ASTM, 2004.

[50] C. Sun, Y. Wang, J. Sun, X. Lin, X. Li, H. Liu, X. Cheng, Effect of impurity on the corrosion behavior of X65 steel in water-saturated supercritical CO_2 system, J. Supercrit. Fluids 116 (2016) 70–82.

[51] X. Dou, D. Zhang, B. Li, H. Jing, H. Xu, Electrochemical studies on local corrosion behavior mechanism of super ferrite stainless steel in low-temperature geothermal water environment, in: IOP Conference Series: Materials Science and Engineering, Vol. 493, (1) IOP Publishing, 2019, 012081.

[52] T. Berntsen, M. Seiersten, T. Hemmingsen, Effect of $FeCO_3$ supersaturation and carbide exposure on the CO_2 corrosion rate of carbon steel, Corrosion 69 (6) (2013) 601–613.

[53] A. Dugstad, P.-E. Dronen, Efficient corrosion control of gas condensate pipelines by pH-stabilization, in: CORROSION 99, OnePetro, 1999.

[54] M. Shayegani, M. Ghorbani, A. Afshar, M. Rahmaniyan, Modelling of carbon dioxide corrosion of steel with iron carbonate precipitation, Corros. Eng. Sci. Technol. 44 (2) (2009) 128–136.

[55] J. Chastain, R.C. King Jr., Handbook of X-ray photoelectron spectroscopy, Perkin-Elmer Corporation 40 (1992) 221.

[56] J. Heuer, J. Stubbins, An XPS characterization of $FeCO_3$ films from CO_2 corrosion, Corros. Sci. 41 (7) (1999) 1231–1243.

[57] X. Yue, L. Zhang, Y. Wang, S. Xu, C. Wang, M. Lu, A. Neville, Y. Hua, Evolution and characterization of the film formed on super $13Cr$ stainless steel in CO_2-saturated formation water at high temperature, Corros. Sci. 163 (2020) 108277.

[58] M.C. Biesinger, B.P. Payne, A.P. Grosvenor, L.W. Lau, A.R. Gerson, R.S.C. Smart, Resolving surface chemical states in XPS analysis of first row transition metals, oxides and hydroxides: Cr, Mn, Fe, Co and Ni, Appl. Surf. Sci. 257 (7) (2011) 2717–2730.

[59] M. Rogowska, J. Gudme, A. Rubin, K. Pantleon, R. Ambat, Effect of fe ion concentration on corrosion of carbon steel in CO2 environment, Corros. Eng. Sci. Technol. 51 (1) (2016) 25–36.

[60] G. Carter, J.S. Colligon, Ion Bombardment of Solids, American Elsevier Publishing CO., New York, 1968, p. 446.

[61] K. Wandelt, Photoemission studies of adsorbed oxygen and oxide layers, Surf. Sci. Rep. 2 (1) (1982) 1–121.

[62] R. King, J. Miller, J. Smith, Corrosion of mild steel by iron sulphides, Br. Corros. J. 8 (3) (1973) 137–141.

[63] F. Farelas, M. Galicia, B. Brown, S. Nešić, H. Castaneda, Evolution of dissolution processes at the interface of carbon steel corroding in a CO_2 environment studied by EIS, Corros. Sci. 52 (2) (2010) 509–517.

[64] D. Staicopolus, The role of cementite in the acidic corrosion of steel, J. Electrochem. Soc. 110 (11) (1963) 1121.

[65] K. Videm, J. Kvarekval, T.E. Perez, G. Fitzsimons, Surface effects on the electrochemistry of iron and carbon steel electrodes in aqueous CO_2 solutions, in: CORROSION 96, OnePetro, 1996.

[66] S. Al-Hassan, B. Mishra, D. Olson, M. Salama, Effect of microstructure on corrosion of steels in aqueous solutions containing carbon dioxide, Corrosion 54 (06) (1998).

[67] E. Van Hunnik, E. Hendriksen, B.F. Pots, The formation of protective $FeCO_3$ corrosion product layers in CO_2 corrosion, in: CORROSION 96, OnePetro, 1996.

[68] D. Clover, B. Kinsella, B. Pejcic, R. De Marco, The influence of microstructure on the corrosion rate of various carbon steels, J. Appl. Electrochem. 35 (2) (2005) 139–149.

[69] E. Gulbrandsen, A. Stangeland, T. Burchardt, S. Nešić, S. Morten Hesjevik, S. Skjfrve, B. Sundfer, Effect of precorrosion on the performance of inhibitors for CO_2 corrosion of carbon steel, in: CORROSION 98, OnePetro, 1998.

[70] S. Nešic, M. Nordsveen, R. Nyborg, A. Stangeland, A mechanistic model for carbon dioxide corrosion of mild steel in the presence of protective iron carbonate films—part 2: a numerical experiment, Corrosion 59 (6) (2003) 489–497.

[71] R. Woollam, K. Tummala, J. Vera, S. Hernandez, Thermodynamic prediction of $FeCO_3/FeS$ corrosion product films, in: CORROSION 2011, OnePetro, 2011.

[72] S. Nešić, J. Postlethwaite, S. Olsen, An electrochemical model for prediction of corrosion of mild steel in aqueous carbon dioxide solutions, Corrosion 52 (4) (1996) 280–294.

[73] R. Barker, I. Al Shaaili, R. De Motte, D. Burkle, T. Charpentier, S. Vargas, A. Neville, Iron carbonate formation kinetics onto corroding and pre-filmed carbon steel surfaces in carbon dioxide corrosion environments, Appl. Surf. Sci. 469 (2019) 135–145.

[74] C. Rémazeilles, P. Refait, Fe (II) hydroxycarbonate Fe2 (OH) 2CO3 (chukanovite) as iron corrosion product: Synthesis and study by Fourier Transform Infrared Spectroscopy, Polyhedron 28 (4) (2009) 749–756.

[75] D. Bairagi, V. Munukuti, P. Bhuyan, R. Saha, S. Mandal, Effect of spheroidized microstructure on the impact toughness and electrochemical performance of a high-carbon steel, Mater. Corros. 72 (5) (2021) 829–838.

[76] M. Gao, X. Pang, K. Gao, The growth mechanism of CO_2 corrosion product films, Corros. Sci. 53 (2) (2011) 557–568.

[77] J.C. Brice, J.C. Brice, The Growth of Crystals from Liquids, Vol. 12, North-Holland Publishing Company Amsterdam, 1973.

[78] G.A. Schmitt, N. Stradmann, Wettability of steel surfaces at CO_2 corrosion conditions. I. effect of surface active compounds in aqueous and hydrocarbon media, in: CORROSION 98, OnePetro, 1998.

[79] A. Abdal-Hay, A.S. Hamdy, J.H. Lim, Facile preparation of titanium dioxide micro/nanofibers and tubular structures by air jet spinning, Ceram. Int. 40 (10) (2014) 15403–15409.

[80] H. Wang, C. Yu, X. Gao, L. Du, H. Wang, Corrosion behavior of ferrite-pearlite steel exposed to H_2S/CO_2 environment, Int. J. Electrochem. Sci. 15 (2020) 6737–6747.

[81] R. Nyborg, A. Dugstad, Mesa corrosion attack in carbon steel and 0.5% chromium steel, in: CORROSION 98, OnePetro, 1998.

[82] J.L. Crolet, N. Thevenot, S. Nešić, Role of conductive corrosion products on the protectiveness of corrosion layers, in: CORROSION 96, OnePetro, 1996.

[83] J. Crolet, S. Olsen, W. Wilhelmsen, Influence of a layer of undissolved cementite on the rate of the CO_2 corrosion of carbon steel, Tech. rep., NACE International, Houston, TX (United States), 1994.

[84] J. Crolet, W. Wilhelmsen, S. Olsen, Observations of multiple steady states in the CO_2 corrosion of carbon steel, Revue de Métallurgie 92 (1995).

[85] S. Chan, J. Charles, Effect of carbon content on hydrogen occlusivity and embrittlement of ferrite–pearlite steels, Mater. Sci. Technol. 2 (9) (1986) 956–962.

[86] D. Burkle, R. De Motte, W. Taleb, A. Kleppe, T. Comyn, S. Vargas, A. Neville, R. Barker, In situ $SR-XRD$ study of $FeCO_3$ precipitation kinetics onto carbon steel in CO_2-containing environments: The influence of brine pH, Electrochim. Acta 255 (2017) 127–144.

[87] T. Tanupabrungsun, B. Brown, S. Nešić, Effect of pH on CO_2 corrosion of mild steel at elevated temperatures, in: CORROSION 2013, OnePetro, 2013.

[88] M. Kermani, A. Morshed, Carbon dioxide corrosion in oil and gas production compendium, Corrosion 59 (08) (2003).

[89] W. Li, B. Brown, D. Young, S. Nešić, Investigation of pseudo-passivation of mild steel in CO_2 corrosion, Corrosion 70 (3) (2014) 294–302.

[90] H. Ma, X. Cheng, S. Chen, C. Wang, J. Zhang, H. Yang, An ac impedance study of the anodic dissolution of iron in sulfuric acid solutions containing hydrogen sulfide, J. Electroanal. Soc. 451 (1–2) (1998) 11–17.

[91] X. Cheng, H. Ma, J. Zhang, X. Chen, S. Chen, H. Yang, Corrosion of iron in acid solutions with hydrogen sulfide, Corrosion 54 (5) (1998) 369–376.

[92] H. Ma, X. Cheng, S. Chen, G. Li, X. Chen, S. Lei, H. Yang, Theoretical interpretation on impedance spectra for anodic iron dissolution in acidic solutions containing hydrogen sulfide, Corrosion 54 (8) (1998) 634–640.

[93] D. Shoesmith, P. Taylor, M. Bailey, B. Ikeda, Electrochemical behaviour of iron in alkaline sulphide solutions, Electrochim. Acta 23 (9) (1978) 903–916.

[94] B.D. Craig, The nature of iron sulfides formed on steel in an H_2S-O_2 environment, Corrosion 35 (3) (1979) 136–138.

[95] Y.-S. Choi, S. Nešić, S. Ling, Effect of H_2S on the CO_2 corrosion of carbon steel in acidic solutions, Electrochim. Acta 56 (4) (2011) 1752–1760.

[96] M. Lucio-Garcia, J. Gonzalez-Rodriguez, M. Casales, L. Martinez, J. Chacon-Nava, M. Neri-Flores, A. Martinez-Villafañe, Effect of heat treatment on H_2S corrosion of a micro-alloyed $C-Mn$ steel, Corros. Sci. 51 (10) (2009) 2380–2386.

[97] H. Ma, X. Cheng, G. Li, S. Chen, Z. Quan, S. Zhao, L. Niu, The influence of hydrogen sulfide on corrosion of iron under different conditions, Corros. Sci. 42 (10) (2000) 1669–1683.

[98] K. Videm, J. Kvarekvål, Corrosion of carbon steel in carbon dioxide-saturated solutions containing small amounts of hydrogen sulfide, Corrosion 51 (04) (1995).

[99] D.W. Shoesmith, P. Taylor, M.G. Bailey, D.G. Owen, The formation of ferrous monosulfide polymorphs during the corrosion of iron by aqueous hydrogen sulfide at 21 C, J. Electrochem. Soc. 127 (5) (1980) 1007.

[100] P. Marcus, E. Protopopoff, Potential-pH diagrams for adsorbed species: Application to sulfur adsorbed on iron in water at 25 and 300 C, J. Electrochem. Soc. 137 (9) (1990) 2709.

[101] Y. Zheng, J. Ning, B. Brown, S. Nešić, Electrochemical model of mild steel corrosion in a mixed H_2S/CO_2 aqueous environment in the absence of protective corrosion product layers, Corrosion 71 (3) (2015) 316–325.

[102] M.J. Cancio, M.L. Latino, T.E. Perez, Corrosion and hydrogen insertion in UNS $G41300$ steels in brine acid solutions saturated with hydrogen sulfide, in: CORROSION 2012, OnePetro, 2012.

[103] S.N. Smith, J.L. Pacheco, Prediction of corrosion in slightly sour environments, in: CORROSION 2002, OnePetro, 2002.

[104] W. Sun, S. Nešić, A mechanistic model of H_2S corrosion of mild steel, in: CORROSION 2007, OnePetro, 2007.

[105] E. Wallaert, T. Depover, I. De Graeve, K. Verbeken, FeS Corrosion products formation and hydrogen uptake in a sour environment for quenched & tempered steel, Metals 8 (1) (2018) 62.

[106] S.N. Smith, Current understanding of corrosion mechanisms due to H_2S in oil and gas production environments, in: CORROSION 2015, OnePetro, 2015.

[107] F. Pessu, Y. Hua, R. Barker, A. Neville, A study of the pitting and uniform corrosion characteristics of $X65$ carbon steel in different H_2S-CO_2-containing environments, Corrosion 74 (8) (2018) 886–902.

[108] B. Brown, D. Young, S. Nešić, Localized corrosion in an H_2S/CO_2 environment, in: The 17th International Corrosion Congress, NACE International, Houston, TX, 2009.

[109] M.D. Bonaventura, B. Brown, S. Nešić, M. Singer, Effect of flow and steel microstructure on the formation of iron carbonate, Corrosion 75 (10) (2019) 1183–1193.

[110] Z. Yin, L. Liu, Y. Wang, T. Yang, Y. Chen, Study on iron sulphide inhibition and corrosion of $80S$ and $110S.S$ steels in acid solutions containing H_2S and CO_2, Int. J. Electrochem. Sci. 15 (2020) 10825–10843.

[111] P. Taylor, T. Rummery, D. Owen, Reactions of iron monosulfide solids with aqueous hydrogen sulfide up to 160 C, J. Inorg. Nucl. Chem. 41 (12) (1979) 1683–1687.

[112] A. Wikjord, T. Rummery, F. Doern, Crystallization of pyrite from deoxygenated aqueous sulfide solutions at elevated temperature and pressure, Canadian Mineral. 14 (4) (1976) 571–573.

[113] A. Wikjord, T. Rummery, F. Doern, D. Owen, Corrosion and deposition during the exposure of carbon steel to hydrogen sulphide-water solutions, Corros. Sci. 20 (5) (1980) 651–671.

[114] J. Ning, Y. Zheng, B. Brown, D. Young, S. Nešić, The role of pyrite in localized H_2S corrosion of mild steel, in: CORROSION 2017, OnePetro, 2017.

[115] D. Rickard, Kinetics of pyrite formation by the H_2S oxidation of iron (II) monosulfide in aqueous solutions between 25 C and 125 C: The rate equation, Geochim. Cosmochim. Acta 61 (1) (1997) 115–134.

[116] P. Bai, H. Zhao, S. Zheng, C. Chen, Initiation and developmental stages of steel corrosion in wet H_2S environments, Corros. Sci. 93 (2015) 109–119.

Paper III

Shabnam Karimi, Iman Taji, Tarlan Hajilou, Simona Palencsar, Arne Dugstad, Afrooz Barnoush, Kim Verbeken, Roy Johnsen, Tom depover

Thermal desorption spectroscopy study of the interaction between hydrogen and microstructural constituents in high-strength carbon steels

Corrosion Science Journal (2023)
https://www.sciencedirect.com/science/article/pii/S0010938X23002524

Corrosion Science 219 (2023) 111210

Contents lists available at ScienceDirect

Corrosion Science

journal homepage: www.elsevier.com/locate/corsci

Evaluation of microstructural and environmental effects on the hydrogen uptake and desorption in high-strength carbon steels: A thermal desorption spectroscopy study

Shabnam Karimi [a,*], Iman Taji [a], Simona Palencsár [b], Arne Dugstad [b], Tarlan Hajilou [a], Afrooz Barnoush [a,c], Kim Verbeken [d], Roy Johnsen [a], Tom Depover [d]

[a] Department of Mechanical and Industrial Engineering, Norwegian University of Science and Technology (NTNU), N-7491 Trondheim, Norway
[b] Institute for Energy Technology (IFE), P.O. Box 40, NO-2027, Kjeller, Norway
[c] Qatar Environment and Energy Research Institute (QEERI), Hamad Bin Khalifa University (HBKU), P.O. Box 34110, Doha, Qatar
[d] Department of Material, Textiles and Chemical Engineering, Ghent University (UGent), Technologiepark 46, B-9052 Ghent, Belgium

ARTICLE INFO

Keywords:
Thermal desorption spectroscopy
Carbon steel
CO_2 environment
CO_2/H_2S environment
Pearlite
Spheroidite

ABSTRACT

The hydrogen uptake in three high-strength carbon steels is studied after exposure to three different environments: an aqueous solution with CO_2 bubbling, CO_2/H_2S bubbling, and cathodic charging without external gassing. The hydrogen uptake is substantially higher in CO_2/H_2S environment compared to CO_2 environment for all materials. The lamellar cementite morphology absorbs higher hydrogen than the material with spheroidite microstructure with similar carbon content. The corrosion layer formed on the steels in CO_2 environment strongly affects the hydrogen effusion and the thermal desorption spectroscopy spectrum in all materials, while the corrosion layer formed in CO_2/H_2S environment does not show this effect.

1. Introduction

Flexible pipes are key components in offshore oil and gas fields. Their role is to transport the hydrocarbons, fluids, and gas between the production facilities and the subsea installations. They are composed of several metallic and polymeric layers and their structure is illustrated in other studies [1,2]. Carbon steels have a strong position in flexible pipe production due to their excellent mechanical properties, availability, and cost [3]. The carbon steels that are used in flexible pipes are subjected to tension and compression and are prone to failure [2]. Therefore, the potential hydrogen embrittlement of flexible pipe carbon steels is a key factor that should be considered in material selection.

A very corrosive environment can develop in the annulus space of a flexible pipe due to the entry of chemical species like CO_2 and H_2S along with water into the annulus. CO_2 can generate carbonic acid in the brine and accelerate the corrosion process [4,5]. Previous studies showed that steels are susceptible to environmentally assisted cracking due to the presence of CO_2 in a saline environment [6–8]. The detrimental effect of CO_2 is less critical than in the H_2S environment for the same material. H_2S prevents the hydrogen recombination and increases the hydrogen uptake in steels [9]. Furthermore, hydrogen sulfide in an aqueous environment takes part in auto-catalytic cathodic reaction and produce more $H_{(abs)}$ on the surface of the steel [10]. The presence of H_2S along with CO_2 cause different failures like sulfide stress corrosion cracking, hydrogen induced cracking, and hydrogen embrittlement [11–14].

Both CO_2 and H_2S generate hydrogen protons (H^+) in an aqueous environment. The generated proton can corrode the surface of the steel and can also react with the electrons and produce atomic hydrogen. This atomic hydrogen permeates into the steel and can either fill the trapping sites in the material, linked to microstructural heterogeneities, or diffuse via the lattice sites [15]. These hydrogen traps are the microstructural sites with higher hydrogen affinity than the interstitial lattice sites, such as dislocations, voids, vacancies, grain boundaries, phase boundaries, carbides, and some intermetallic particles [16,17]. Therefore, besides the effect of the environment on the hydrogen uptake capacity, the microstructure of carbon steel also plays a crucial role. In a corrosive environment, not only the rate of cathodic reactions controlling the amount of hydrogen produced on the surface but also where the cathodic reaction happens on the surface of the steel is a relevant parameter [18].

In a ferrite/pearlite microstructure, the cementite (Fe_3C)/ferrite interfaces act as a trap for hydrogen [19–21]. The Fe_3C phase can also function as a cathodic site which accelerates the anodic dissolution process of the ferrite phase in a corrosive environment [22,23]. The Fe_3C

* Corresponding author.
E-mail address: shabnam.karimi@ntnu.no (S. Karimi).

https://doi.org/10.1016/j.corsci.2023.111210
Received 7 February 2023; Received in revised form 14 March 2023; Accepted 21 April 2023
Available online 4 May 2023

phase remains on the metal surface after the selective dissolution of ferrite [6]. In CO_2 environment, if the concentration of Fe^{2+} and CO_3^{2-} ions is sufficient, the iron carbonate ($FeCO_3$) can precipitate in between the remaining Fe_3C particles or layers and decrease the corrosion rate, slowing down the diffusion of ions to and from the steel surface and retard the hydrogen uptake [6,24]. Since the remaining Fe_3C functions as a mechanical anchor for the corrosion products like $FeCO_3$ to adhere to the steel surface and make a protective covering on the surface, the morphology and distribution of Fe_3C are of high importance [25]. Indeed the morphology, distribution, and fraction of Fe_3C have an important effect on hydrogen uptake whether Fe_3C is considered as a microstructural feature or a constitute of the corrosion layer. Crolet et al. [26] discussed that a lamellar remaining Fe_3C phase may induce internal acidification in the corrosion layer and inhibit the formation of $FeCO_3$ and as a result prevent the formation of a protective layer. In other studies, it has been discussed that the interlamellar spacing in a lamellar pearlite microstructure and the size of the Fe_3C particles affect the hydrogen embrittlement [27–29]. Bott et al. [30] investigated the effect of Fe_3C morphology and distribution on the hydrogen permeation parameters of a low-carbon steel. Their results verified that the changes in the Fe_3C morphology considerably affect the apparent diffusivity, solubility, and permeability of hydrogen. Ramunni et al. [31] showed similar results as Bott et al. They discussed that the fine Fe_3C increases solubility and decreases hydrogen diffusivity in their studied carbon steel, while the lamellar morphology of Fe_3C enhances the hydrogen diffusion coefficient and reduces the hydrogen solubility.

In the H_2S environment, sulfides are the main corrosion product that is formed on the steel surface. Sulfides can act as cathodic site and increase the hydrogen uptake [32]. It is also probable to decrease the hydrogen concentration on the steel surface and retard the hydrogen permeation to the steel. Wallaert et al. [33] discussed that the FeS layer forms and grows by ionic conduction of S^{2-} and HS^- which causes the release of a lot of hydrogen outside the FeS layer. The released hydrogen will be lost in the environment and therefore decrease the hydrogen permeation to the steel. Folena et al. [34] showed in their study that dependent on the H_2S concentration and test conditions, different FeS morphologies with different characteristics can form on the steel that has different effects on hydrogen permeation. Mackinawite and pyrrhotite present a weak blocking effect in their study. They discussed that the low concentrations of H_2S result in the precipitation of an inefficient and non-compact FeS film which does not have a diminishing effect on the hydrogen uptake.

Extensive studies have been performed to understand how hydrogen uptake is influenced by the microstructure and the microstructural defects' interaction with hydrogen. However, limited research has studied the influence of cementite morphologies and distribution on hydrogen uptake capacity. The role of the corrosion layers formed on the steels in the presence of the oil and gas industry chemical species like CO_2 and H_2S, on the hydrogen permeation characteristics were investigated before [6,35–38]. However, for the first time, the effect of the corrosion layers on hydrogen effusion and thermal desorption spectroscopy (TDS) is studied and discussed in this paper.

In the present work, three carbon steels with different microstructures, containing 0.62%, 0.65%, and 0.83% carbon (which are used as tensile armor wires in flexible pipes) are exposed to modified artificial seawater with CO_2 and CO_2/H_2S gas purging at open circuit. The same materials were also charged cathodically in a brine solution without external gassing. Employing TDS, the hydrogen uptake in these steels under the exposure to the three above-mentioned environments (CO_2 environment, CO_2/H_2S environment and cathodic charging condition) are studied. The effect of exposure medium, microstructures, and corrosion layers on the hydrogen desorption and TDS spectrum are discussed.

2. Experimental

2.1. Materials and sample preparations

Three carbon steels, containing 0.62, 0.65, and 0.83 wt% carbon, with different microstructures, were investigated in the current study. The studied materials' chemical compositions and mechanical properties [18,39] are listed in Table 1. The materials were received as drawn curved wires with a thickness of 3 mm and a width of 9 to 12 mm. Rectangular specimens, with a length of 12 mm and with the same width and thickness as the wires, were cut from the received wires. Three sets of specimens were prepared. For preparing the first set for corrosion tests, all surfaces were ground with 320 grit SiC paper. The second set with the same dimensions was prepared for cathodic charging. They were ground up to 2000 grit SiC papers. The samples of the third set were ground up to 4000 grit SiC papers and mechanically polished with 3 μm and 1 μm diamond suspensions for microstructural analysis in a Scanning Electron Microscope (SEM). After the grinding and polishing steps, all samples were cleaned in acetone and isopropanol in an ultrasound bath and dried.

2.2. Corrosion tests and hydrogen uptake

The corrosion experiments were conducted in a setup comprising two parts: the test cell, where the test specimens were immersed in the test electrolyte, and the refill cell, which contained the fresh electrolyte required to replenish the electrolyte in the test cell to ensure a low concentration of dissolved corrosion products like Fe^{2+}. A schematic of the corrosion test setup is shown in Fig. 1. Modified $ASTM\ D1141$-90 [40] seawater (without calcium chloride to avoid the formation of non-protective calcium carbonate ($CaCO_3$) [41]), was used as the corrosion test electrolyte. Its chemical composition is presented in Table 2. The electrolyte in both the test cell and refill cell purged with the requisite gas mixture persistently. The setup temperature was kept at 25 °C using a water bath. A gas dosing system based on Bronkhorst mass flow controllers was operated to mix the needed gas composition (N_2, CO_2, H_2S) and purge the test cell and the refill cell.

The electrolyte was circulated between the test cell and refill cell using a peristaltic pump equipped with $Tygon$ and PVC tubes. The flow rates were controlled by the tubing diameter and the rotation speed of the pump. To avoid oxygen contamination, the pump was placed in a chamber purged with N_2. When the peristaltic pump was on, the flow of liquid into the test cell was continuous and had a maximum rate of 4 ml/min (using a 1.143 mm tubing diameter). The backward flow had a maximum rate of 18 ml/min (using a 3.175 mm tubing diameter) and was self-regulated by draw-off to eliminate the risk of overflowing the test cell. The backward flow was directed to a waste container. The pH value was continuously recorded. The pH increased slightly (between 5.77 and 6.08) during both the CO_2 and CO_2/H_2S exposure experiments. The test cell electrolyte was sampled frequently during exposure to analyze its Fe^{2+} ion concentration. The Fe^{2+} ions were converted to a colored Fe complex, which was photometrically quantified. The electrolyte was continuously replaced by fresh electrolyte (with no dissolved corrosion products) at a flow rate of ca. 0.8–1.6 l/day to ensure a low concentration of Fe^{2+} (less than 80 ppm in the test cell).

Two sets of corrosion experiments were performed by purging 0.2 bar CO_2 in set number one and 0.2 bar CO_2, 1 mbar H_2S in the other set with a flow rate of 200 ml/min. In the second test set, since the precipitation of FeS kept the concentration of the dissolved Fe^{2+} ions low, no electrolyte replacement was needed. The duration of both sets of tests was 504 h (21 days). After the corrosion test, the specimens were immediately immersed in liquid nitrogen to prevent the hydrogen egress from the specimens, and also to start the TDS test with a specimen with low temperature to minimize the hydrogen loss before the test onset.

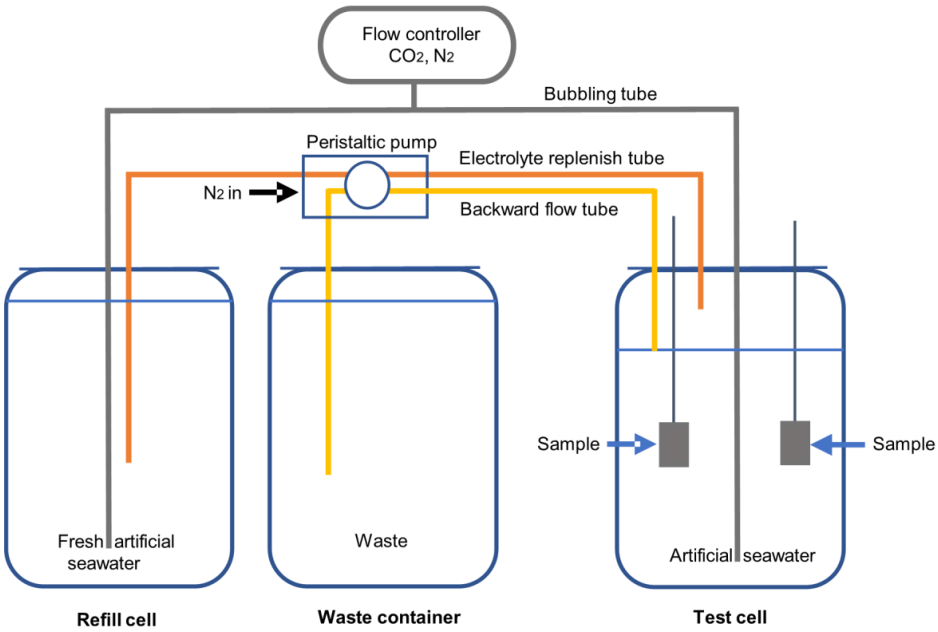

Fig. 1. Schematic of the corrosion test setup used for the CO_2 exposure. The test cell is replenished by fresh artificial seawater in CO_2 environment experiment, while in CO_2/H_2S environment experiment the precipitation of FeS kept the concentration of the dissolved Fe^{2+} ions low and therefore the test cell is not replenished by fresh artificial seawater.

Table 1
Chemical composition and the mechanical properties of the studied materials [18].

Material (wt%)	C	Al	Si	P	Mo	V	Cr	Mn	Ni	Cu	Hardness (HV_{10})	YS (MPa)	UTS (MPa)
$CS62$	0.62	0.26	0.40	0.23	0.46	0.70	0.61	1.36	0.89	0.75	386 ± 8	1100	1300
$CS65$	0.65	0.30	0.24	0.20	0.35	0.51	0.51	0.96	0.60	0.75	384 ± 6	1250	1400
$CS83$	0.83	0.19	0.35	0.30	0.35	0.54	0.55	1.07	0.69	0.59	453 ± 16	1400	1600

Table 2
Chemical composition of the corrosion test electrolyte [40].

Compound	NaCl	$MgCl_2$	Na_2SO_4	KCl	$NaHCO_3$	H_3BO_3	$SrCl_2$
Content (g/l)	24.53	5.2	4.09	0.695	0.201	0.027	0.025

2.3. Cathodic charging of hydrogen

An electrochemical charging using a 3.5% NaCl solution was used to introduce hydrogen in the materials at a constant potential of −1.4 V vs. Ag/AgCl reference electrode. 1 g/L thiourea was added to the solution as a poison to increase the efficiency of hydrogen absorption [42]. Materials were charged for the duration of their saturation limit based on their permeation diffusivity data [18]. In this regard, $CS62$, $CS65$, and $CS83$ were charged for 24, 192, and 168 h, respectively. To assure that they were fully saturated, another set of samples was charged for longer times than their calculated time for saturation limits. Hot extraction tests confirmed that all materials were fully saturated when they were charged for the duration of their saturation limit based on their permeation diffusivity data and no more hydrogen uptake is observed when they are charged longer. Besides, the charging condition was designed in a way to prevent any internal damage or blistering in the materials. After charging, samples were immediately immersed in liquid nitrogen.

This cathodic charging is done as a reference condition where no corrosion products are formed on the sample. This allows the reliable evaluation of the desorption activation energies linked to hydrogen trapping at microstructural constituents. The activation energy for H desorption is calculated using the simplified form of the Kissinger equation [43], which is proposed by Lee et al. [44]:

$$\frac{d(\ln \frac{\phi}{T_{max}^2})}{d(\frac{1}{T_{max}})} = -\frac{E_a}{R} \tag{1}$$

where ϕ is the heating rate (K min^{-1}), T_{max} (K) is the peak temperature, E_a (J K^{-1} mol^{-1}) is the hydrogen detrapping activation energy at T_{max}, and R (J K^{-1} mol^{-1}) is the universal gas constant.

2.4. Thermal desorption spectroscopy (TDS)

The TDS analysis was applied to measure the hydrogen concentration and analyze the hydrogen trapping in the charged samples mentioned in Sections 2.2 and 2.3 using the $G4-Phoenix$ analyzer. TDS analysis is based on the fundamental fact that hydrogen diffuses out from different microstructural features upon heating. Indeed, hydrogen desorbs at different temperatures from each microstructural feature depending on the corresponding binding energy [45]. The detected hydrogen concentration was quantified using the mass spectroscopy (MS) technique with a detection limit of 0.05 ppm(wt).

The hydrogen-charged samples, after corrosion testing (cf. Section 2.2) and after cathodic charging (cf. Section 2.3), were taken from the liquid nitrogen and washed in distilled water and acetone and dried fast (in less than one minute) before they were put into the quartz furnace. The hydrogen concentration was first measured by hot extraction

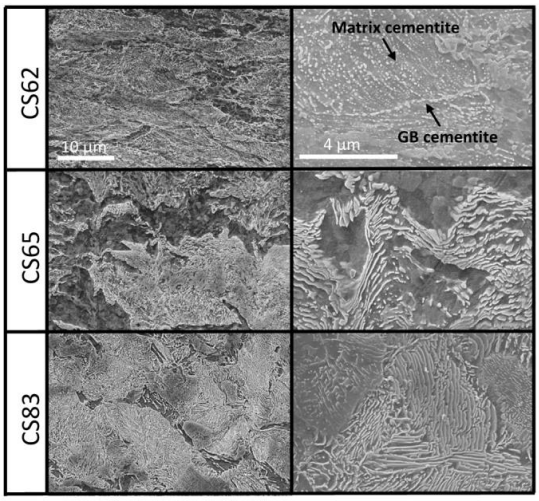

Fig. 2. *SEM* micrographs of the studied materials. The right column shows the higher magnification images of the materials' microstructure. The magnification of the *SEM* images in each column is the same for all materials.

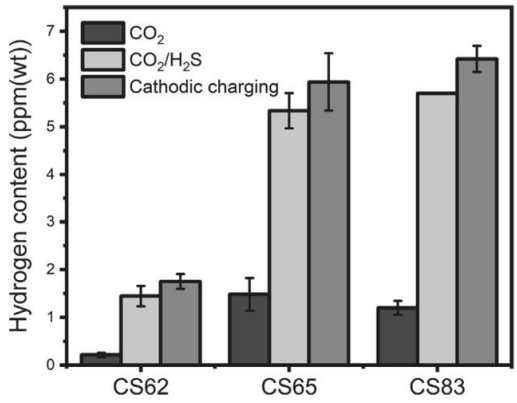

Fig. 3. Hydrogen content obtained by hot extraction at 650 °C for samples exposed to CO_2 and CO_2/H_2S environments for 21 days at room temperature and also after electrochemical charging to saturation. The columns show the mean value of three tests and the bars represent the standard deviation of the mean value. (The hot extraction tests which were done on two *CS*83 samples exposed to CO_2/H_2S environment were failed due to some technical errors of the machine. Therefore the data shown in this graph for material *CS*83 is not an average value).

method where the sample was inserted into the furnace which was pre-heated to 650 °C, an isothermal treatment to determine the hydrogen uptake level. In addition, the hydrogen trapping activation energies were analyzed (Eq. (1)) by heating the sample to 650 °C gradually, using three different heating rates, i.e., 0.2, 0.3, and 0.5 K/s. Three samples of each material and each environmental condition were tested by both hot extraction and *TDS* to ensure the reproducibility of the experiments.

3. Results

3.1. Microstructure characterization

The *SEM* results are presented in Fig. 2. The ferrite, cementite, and pearlite phase fractions for all materials, determined from the *SEM* micrographs analysis with ImageJ [46], are provided in Table 3. *CS*62 has a spheroidite microstructure with small grains of ferrite. The cementite morphology in *CS*62 is spherical or broken lamellae in a ferrite matrix. The cementite particles are located inside the ferrite grains (matrix cementite) and in the grain boundaries (GB cementite) as shown in Fig. 2 (*CS*62). *CS*65 shows a pearlite microstructure with thick lamellae of cementite in a ferrite matrix (Fig. 2 (*CS*65)). It should be noted that the ferrite grain size in *CS*65 is bigger and more connected in comparison with *CS*62. A predominantly lamellar pearlite microstructure with a lower fraction of ferrite in comparison with the other materials constitutes the microstructure of *CS*83.

3.2. Hot extraction

The hot extraction tests were done at 650 °C to determine total H uptake, including reversible, irreversible, and trapped H for *CS*62, *CS*65, and *CS*83 under the three exposure conditions. The results presented in Fig. 3 show that the hydrogen content in the samples which were cathodically charged to saturation for all materials is higher compared to the ones charged in CO_2 and CO_2/H_2S environments. The hydrogen contents in samples exposed to CO_2/H_2S environment remarkably increased in comparison with the samples charged in CO_2 environment. *CS*62 with a spheroidite microstructure shows a significantly lower amount of hydrogen uptake in all environments in comparison with *CS*65 and *CS*83 with ferrite/pearlite microstructure, while the carbon content in *CS*62 is quite close to *CS*65.

Table 3
Microstructures phase fraction and interlamellar spacing.

Material	Ferrite%	Cementite%	Pearlite%	Interlamellar spacing (nm)
*CS*62	91	9	81	–
*CS*65	90	10	85	242 ± 64
*CS*83	88	12	98	117 ± 30

3.3. Thermal desorption spectroscopy

3.3.1. CO_2 and CO_2/H_2S environment

Fig. 4 presents the *TDS* curves for *CS*62, *CS*65 and *CS*83 obtained at a heating rate of 0.5 K/s after exposure to the CO_2 and CO_2/H_2S environments for 21 days. The curves were fitted and deconvoluted into Gaussian curves with three, five, and four peaks for *CS*62, *CS*65, and *CS*83, respectively, in both environments. The shape of the *TDS* spectrum for each material differs significantly in these two environments. In addition, the highest temperature where H is detectable by *TDS* is higher for the materials corroded in CO_2 environment compared to CO_2/H_2S. The hydrogen uptake in *CS*62 in CO_2 environment is remarkably lower than the other materials and is very close to the detection limit of the *G*4−*Phoenix* analyzer. Therefore the resultant curve is noisy and the shoulders in the curve are not necessarily representative of a peak. Due to this obscurity, the curve is not deconvoluted.

3.3.2. Cathodic charging

To investigate the role of corrosion layers formed during the exposure to CO_2 and CO_2/H_2S environments on the hydrogen desorption, the studied materials were cathodically charged with H in a 3.5% NaCl solution containing 1 g/L thiourea for *TDS* measurement. During electrochemical charging, no corrosion product formed on the surface of the materials, and the effect of the corrosion layers on H effusion was eliminated. As mentioned before, according to calculations, the saturation level was reached after 24, 192, and 168 h for *CS*62, *CS*65, and *CS*83, respectively [18]. The results of the *TDS* measurements obtained at a heating rate of 0.5 K/s are presented in Fig. 5.

It should be noted that H mobility within the body-centered cubic (*BCC*) materials is high [47–49]. The diffusion barrier between the tetrahedral sites in a *BCC* iron is 0.1 eV [48]. This fact implies that H starts to effuse from the samples immediately after the sample is taken out from the charging cell and before the start of the H measurement

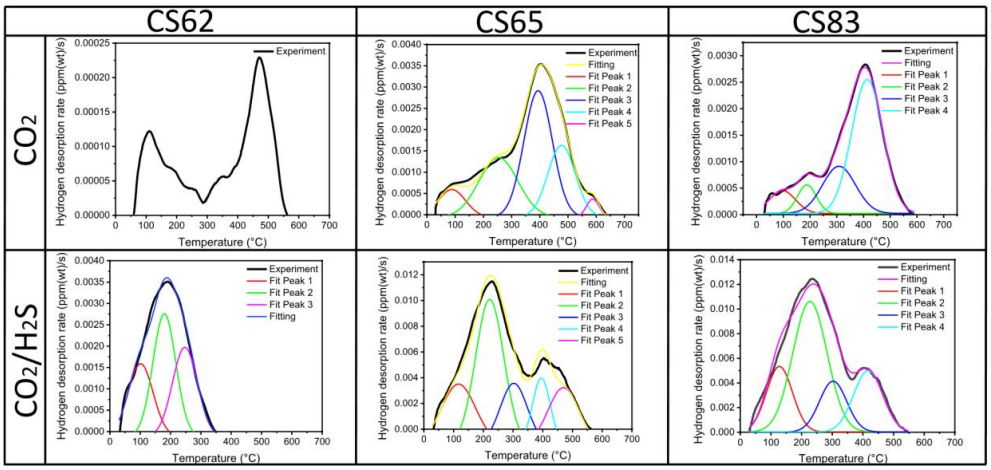

Fig. 4. *TDS* spectra obtained at a heating rate of 0.5 K/s for the studied materials exposed to 0.2 bar CO_2 and 0.2 bar CO_2/1 mbar H_2S environments for 21 days at room temperature. The deconvoluted curves is associated with the H desorption from particular microstructural features. (For interpretation of the references to color in this figure legend, the reader is referred to the web version of this article.)

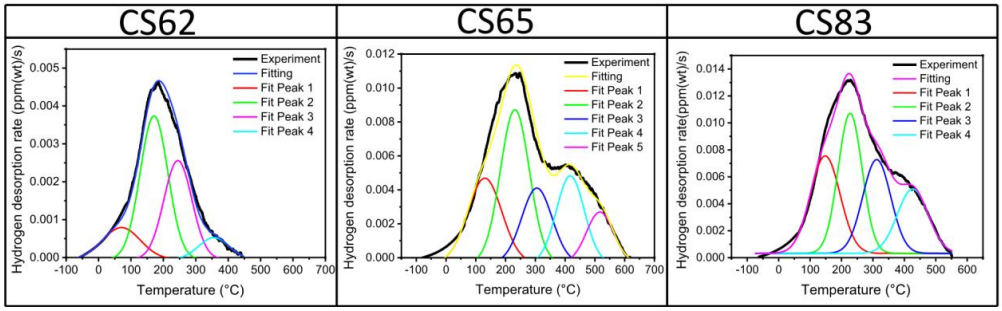

Fig. 5. *TDS* spectra obtained at a heating rate of 0.5 k/s for the studied materials charged cathodically with H till saturation. The deconvoluted curves are associated with the H desorption from particular microstructural features.

[50]. Pinson et al. [51] presented a numerical extrapolation towards cryogenic temperatures to compensate for the amount of H which is lost before the start of the *TDS* measurement. The *TDS* spectra shown in Fig. 5 are extrapolated towards cryogenic temperatures based on the method presented in [51]. A difference between the initial parts of the *TDS* spectrum is obvious when comparing the curves in Figs. 4 and 5. The initial sharp increase in the H effusion which is visible in the *TDS* spectrum in Fig. 4, has been replaced by a gradual increase in Fig. 5 using the numerical extrapolation towards cryogenic temperatures. Therefore, the H effusion starts from the negative temperatures in the *TDS* spectra in Fig. 5. This numerical extrapolation facilitates the *TDS* spectrum deconvolution. This allows a reliable determination of the desorption activation energies related to hydrogen trapping at specific microstructural features. Therefore, the cathodically charged samples, as a reference, are used for this purpose.

Fig. 5 illustrates that the *TDS* spectrum of *CS*62 is fitted with four peaks while it is fitted with three peaks under CO_2/H_2S environment (Fig. 4). The other two materials' *TDS* spectrum were deconvoluted to the same number of peaks as in CO_2 and CO_2/H_2S environments. The H desorption continues at higher temperatures for *CS*62 and *CS*65 which are charged cathodically in comparison with the same materials exposed to CO_2/H_2S environment (*cf*. Figs. 4 and 5). However, H desorption in *CS*83 shows the same ending temperature (around 550 °C) in both the CO_2/H_2S environment and under cathodic charging.

3.4. Peak analysis

The percentage of the total H content related to each deconvoluted peak is shown in Tables 4, 5 and 6 for CO_2 environment, CO_2/H_2S environment and the cathodic charging condition where possible, respectively. The activation energy of each peak was only calculated for the materials which were charged cathodically (Table 6). In CO_2 and CO_2/H_2S environments, the corrosion layer formed on the sample surface can affect both the absorption and desorption of hydrogen. Therefore, to calculate the trap energies of microstructural features, the cathodically charged samples were used.

4. Discussion

4.1. Effect of charging conditions on hydrogen uptake

The studied materials were submitted to three different charging conditions, 0.2 bar CO_2 environment, 0.2 bar CO_2/1 mbar H_2S environment, and cathodic charging using 1 g/L thiourea in a 3.5% NaCl solution. To investigate the hydrogen uptake in a CO_2 environment, one should consider that CO_2 has a significant contribution to the corrosion of carbon steel and corrosion plays an important role in the hydrogen generation and absorption. The higher cathodic currents in the presence of CO_2 in aqueous solutions due to the H_2CO_3 buffering effect [52]

Table 4
The data obtained from the peak analysis of TDS results of the samples exposed to the CO_2 environment.

Peak	*CS*62		*CS*65		*CS*83	
	T_{max} (°C)	H fraction (%)	T_{max} (°C)	H fraction (%)	T_{max} (°C)	H fraction (%)
1st peak	–	–	89 ± 6	7	93 ± 7	8.4
2nd peak	–	–	250 ± 3	26.1	184 ± 6	8.2
3rd peak	–	–	386 ± 10	42.4	303 ± 6	23.2
4th peak	–	–	471 ± 6	22.5	409 ± 7	60.2
5th peak	–		584 ± 9	2	–	–

Table 5
The data obtained from the peak analysis of TDS results of the samples exposed to the CO_2/H_2S environment.

Peak	*CS*62		*CS*65		*CS*83	
	T_{max} (°C)	H fraction (%)	T_{max} (°C)	H fraction (%)	T_{max} (°C)	H fraction (%)
1st peak	100 ± 2	25.3	110 ± 9	17	131 ± 5	18
2nd peak	176 ± 5	42.5	183 ± 9	44.8	224 ± 5	48
3rd peak	244 ± 4	32.2	296 ± 6	13.9	303 ± 6	15
4th peak	–	–	387 ± 12	10.3	403 ± 9	19
5th peak	–	–	462 ± 11	14	–	–

Table 6
The data obtained from the peak analysis of TDS results of the samples charged under the cathodic charging condition.

Peak	*CS*62			*CS*65			*CS*83		
	T_{max} (°C)	H fraction (%)	Activation energy (kJ/mol)	T_{max} (°C)	H fraction (%)	Activation energy (kJ/mol)	T_{max} (°C)	H fraction (%)	Activation energy (kJ/mol)
1st peak	80 ± 9	12	15.2	141 ± 10	21.4	14.3	154 ± 17	27.2	18.6
2nd peak	164 ± 7	48	15	228 ± 10	34.6	17.1	227 ± 5	28.6	37.8
3rd peak	251 ± 7	33	26.4	314 ± 11	16.6	19.9	313 ± 17	25	35
4th peak	349 ± 7	7	63.8	423 ± 8	18.1	35.3	415 ± 12	19.2	64
5th peak	–	–	–	514 ± 9	9.3	69.3	–	–	–

and the reduction of H_2CO_3 and HCO_3^- close to the surface is vastly reported in previous studies [53–55]. This results in an increased H^+ availability on the carbon steel surface according to the following reactions [54,56]:

$$CO_2 + H_2O \rightleftarrows H_2CO_3 \quad (2)$$

$$H_2CO_3 \rightleftarrows H^+ + HCO_3^- \quad (3)$$

$$HCO_3^- \rightleftarrows H^+ + CO_3^{2-} \quad (4)$$

The generated H^+ ions in the above-mentioned reactions can adsorb on the metal surface through the Volmer reaction (Eq. (5)) and combine to form H_2 molecules through the Tafel chemical reaction (Eq. (6)) [57]:

$$H^+ + e^- \rightleftarrows H_{(ads)} \quad (5)$$

$$H_{(ads)} + H_{(ads)} \rightleftarrows H_2 \quad (6)$$

Or through the electrochemical Heyrovsky reaction [58]:

$$H_{(ads)} + H^+ + e^- \rightleftarrows H_2 \quad (7)$$

Or they can absorb to the subsurface and then diffuse into the steel [59]:

$$H_{(ads)} \rightleftarrows H_{(abs)} \quad (8)$$

In a CO_2/H_2S coexisting environment, the corrosion behavior is more vague and intricate and even a small amount of CO_2 in an H_2S environment or a small amount of H_2S in a CO_2 environment can affect the corrosion significantly compared to the pure H_2S or CO_2 environments, respectively. As it is discussed above, CO_2 can react with water and form acid and then decompose and generate a proton (Eqs. (2)–(4)). H_2S can also decompose to HS^- and S^{2-} and generate protons [60,61]:

$$H_2S \rightleftarrows H^+ + HS^- \quad (9)$$

$$HS^- \rightleftarrows H^+ + S^{2-} \quad (10)$$

In a CO_2/H_2S mixed environment, the amount of H which is available on the steel surface is higher compared to pure CO_2 environment due to the synergistic effects of CO_2 and H_2S on corrosion and H generation. The hydrogen uptake in all studied materials shows a higher value in CO_2/H_2S environment compared with the results in pure CO_2 environment as shown in Fig. 3. The significant difference between the hydrogen uptake in these two environments can be correlated to the fact that in CO_2 environment, the dissociation and H generation process includes one more step which is related to the dissolution of CO_2 in water and forming carbolic acid (Eq. (2)), while the direct dissociation process of H_2S (Eq. (9)) in CO_2/H_2S environment accelerates the H generation. Besides, in environments containing sulfur species, the kinetics of the evolution of gaseous hydrogen or the recombination of atomic H (Eqs. (6) and (7)) is slowed down significantly. Therefore, the adsorption of atomic H on the material surface increases [62–64].

During cathodic charging, the cathodic reaction rate is increased and generates more H atoms and at the same time enhances the H atom recombination rate (Eqs. (6) and (7)) [59]. In this study, however, thiourea is added to the cathodic charging electrolyte to decrease the H recombination rate and increase the amount of absorbed H into the material. Therefore as it can be seen in Fig. 3, the H uptake is higher for all the materials which are cathodically charged in comparison with the materials corroded in CO_2 and CO_2/H_2S environments.

*CS*65 and *CS*83 display two distinct peaks before deconvolution in CO_2/H_2S environment which are shown by black color in Fig. 4. One peak at a lower temperature originates from reversible hydrogen and one at a higher temperature originates from deep-trapped hydrogen. In cathodic charging, these two peaks are closer to each other in both materials (Fig. 5). Kirchheim [65] discussed that when these two peaks are separated sufficiently, the deep trap sites stay filled during the first peak hydrogen desorption. At higher temperatures, when the second peak is revealed, the hydrogen from the deep traps starts to effuse out of the sample. The saturation after cathodic charging

causes the overlap between the peaks of hydrogen desorption from the different traps. Indeed after saturation, the diffusible hydrogen traps like grain boundaries and dislocations are filled with hydrogen and the hydrogen desorption from these traps continues even at higher temperatures. Therefore, the hydrogen desorption from the diffusible traps can overlap with high-temperature peaks.

Although the same trap density is available in each microstructure, the trap occupancy differs depending on the environment and equilibrium obtained (depending on the total hydrogen uptake). In the corrosion exposure testing (CO_2 and CO_2/H_2S environments), the occupancy of the reversible trap sites was lower due to the lower uptake level, while a higher concentration was obtained for the cathodically charged exposure. This affects the equilibrium between the lower and higher trapping sites in the microstructure, which can result in the observed variations in the overlapping of the different peaks. Nevertheless, since the corrosion layers can also affect desorption, the most reliable interpretation of trap sites can only be done based on the cathodically charged samples.

4.2. Effect of microstructure on hydrogen uptake

When H penetrates a material, it interacts with the microstructural defects and sometimes it is trapped in a defect to decrease its energy. The results in Fig. 3 confirm that in CO_2/H_2S environment and cathodic H charging condition, the H uptake increases with carbon content and $CS83$ exhibits the highest amount of H uptake. There is a significant difference between H uptake in $CS62$ and $CS65$. The carbon content of these two materials is very close (0.62% and 0.65%). However, the $CS62$ microstructure consists of the spherical or broken lamella of cementite in a ferrite matrix while $CS65$ shows a pearlite/ferrite microstructure with thick lamellae of cementite in a ferrite matrix (Fig. 2). The significant difference between the H uptake of these two materials shows that the microstructure and the morphology and distribution of the cementite phase play a more important role than the carbon content in the H uptake capacity in carbon steels. Amemiya et al. [66] showed in their Electron Backscatter Diffraction ($EBSD$) analysis that the lattice parameters ratios of the cementite lamellae are completely different from the spheroidized cementite particles which indicates that a lamellar pearlite microstructure has a certain amount of internal stress. The internal stress in a lamellar microstructure can cause a higher H uptake in $CS65$ in comparison with $CS62$. Moreover, the cementite/ferrite interface area in a lamellar microstructure of $CS65$ is higher than this area in a spheroidite microstructure of $CS62$.

The H uptake in $CS83$ is slightly higher than that in $CS65$ in both CO_2/H_2S environment and under cathodic charging. The high amount of cementite/ferrite interfaces in $CS83$ leads to a higher H uptake in comparison with $CS65$. Furthermore, since the grain size and the pearlite colony size in $CS83$ are finer than in $CS65$ [18], this material has more area of pearlite/pearlite interfaces in its microstructure. The high susceptibility of pearlite/pearlite interfaces to H embrittlement has previously been investigated and published by the present authors [39]. Therefore $CS83$ shows a higher capacity for H uptake.

According to the deconvoluted peaks in Fig. 5 which are related to the cathodic charging condition, the first three peaks show very similar activation energies for all materials, in a range of 15 to 37.8 kJ/mol (Table 6). Correlating each peak with the particular microstructural defects would not be straightforward. However, using the activation energies found in the literature one can relate these peaks to the microstructural defects with a reasonable approximation. For instance, the activation energy for hydrogen desorption in different microstructural defects based on the literature are as follows: 0–20 kJ/mol for elastic strain field of dislocations [67], 17–60 kJ/mol for screw dislocation cores and grain boundaries [68–70], 30–50 kJ/mol for micro-voids, voids and vacancies [67,71], and 41–59 kJ/mol for cementite vacancies [72]. In a pearlitic microstructure, the hydrogen trapping activation energy within the ferrite/cementite interfaces is reported in a wide range from 10.85 to 66.3 kJ/mol [72–76]. Some studies considered the ferrite/cementite interface as a reversible trap [77] while others correspond it to the irreversible hydrogen trapping sites [75,76]. With a comparison between the activation energies reported in the literature and the calculated activation energies in Table 6, the first three deconvoluted peaks in all the materials can be related to grain boundaries, dislocations, micro-voids, and vacancies.

Based on Table 6 for cathodic charging the diffusible hydrogen fraction (sum of the first three peaks) in $CS62$ is 93% which is higher than for $CS83$ (≅81%). It should be noted that this comparison is between the hydrogen fraction relative to the total hydrogen in both materials and it is obvious from Fig. 5 that the diffusible peaks (1,2 and 3) in $CS83$ contain more hydrogen in comparison with the same peaks in $CS62$. In $CS62$, the spherical or broken lamella of cementite particles is dispersed in the ferrite grains. In $CS83$ cementite lamellar morphology constitutes the pearlitic microstructure. Therefore, the boundaries between the prior-austenite grains are the boundaries between two ferritic grains in $CS62$, while in $CS83$, they are the boundaries between two pearlite colonies. As discussed before, the pearlite/ferrite and the pearlite/pearlite boundaries are incoherent and high-energy interfaces that are susceptible to hydrogen embrittlement. The stress field due to the volume change during the austenite to pearlite transformation, exposes a high tension in these interfaces with high dislocation density [19]. These boundaries are a suitable trap for hydrogen accumulation [39]. The fourth deconvoluted peak in $CS83$ is related to the presence of a large area of pearlite/pearlite interfaces, while in $CS62$, there is not any high-temperature peak in CO_2/H_2S environment. In this material, only after cathodic charging and saturation, the high-temperature peak (fourth peak) appears (Fig. 5 and Table 6). In fact, in $CS62$ the interfaces between the prior-austenite grains are not of the same type as in $CS83$. As mentioned before, these interfaces are the boundaries between two ferrite grains which are not considered as irreversible traps as the pearlite/pearlite or pearlite/ferrite interfaces in $CS65$ and $CS83$. Therefore, the diffusible hydrogen fraction related to ferrite/cementite interfaces, dislocations, vacancies, and grain boundaries in $CS62$ is higher than for the two other materials.

The sum of the H fraction of peaks 1, 2, and 3 is almost the same in CO_2/H_2S environment and cathodic charging for $CS65$ and $CS83$ (H fraction related to peak 1,2 and 3 for $CS65$ is 75.7% and 72.6% in CO_2/H_2S environment and cathodic H charging condition, respectively, while for $CS83$ is ≅81% in both CO_2/H_2S environment and cathodic H charging condition). This means that the reversible peaks (peaks 1, 2, and 3) are filled with almost the same amount of H in both charging conditions. The H fugacity is high enough in both CO_2/H_2S and cathodic charging conditions to fill the reversible traps. In $CS65$, this H fraction is higher in CO_2/H_2S environment (75.7%) in comparison with the cathodic charging condition (72.6%) whose reason is explained in the next paragraph. For $CS62$, in CO_2/H_2S environment, all three peaks are considered to be related to the reversible H, while under cathodic charging a small irreversible H peak appears with the H fraction of 7%.

To analyze the irreversible peaks, it should first be noted that as shown in Figs. 4 and 5, the TDS spectrum of $CS65$ deconvoluted to 5 peaks, i.e that this material exhibits two irreversible peaks while $CS83$ shows one irreversible peak. These two materials exhibit a lamellar cementite morphology. The fourth peak in the TDS spectrum of $CS65$ with the maximum temperature of 423 ± 8 °C (Table 6) can be correlated to the release of H from the previous reversible trap with the maximum temperature of 314 ± 11 °C. The activation energy of the fourth peak of $CS65$ is 35.3 kJ/mol which is similar to the activation energy of peak 3 in $CS83$ that has almost the same maximum temperature of the third peak in $CS65$ as is shown in Table 6 (314 ±11 °C and 313 ± 17 °C, respectively). Therefore, the fourth peak in $CS65$ can be a part of the third peak in this material whose H desorbs with a delay. Based on electrochemical permeation tests done by Skilbred et al. [18] on the

same materials as this study, $CS65$ showed the highest time lag and the lowest diffusion coefficient. Furthermore, $CS65$ has the highest amount of tortuosity [18]. All of the above-mentioned parameters delay the H desorption from the traps. This can explain the higher temperature in which the H desorption stops in $CS65$ compared to the other materials as well (Fig. 5). As a result, it seems reasonable to verify the idea that the fourth peak is a part of the third peak which desorbs with a delay. This observation is in agreement with Takai et al. [75] who showed that the high-temperature peak in the TDS spectrum consists of non-diffusible hydrogen and a part of diffusible hydrogen in high-strength steel. The fifth peak in $CS65$ can correspond to the fourth peak of $CS62$ and $CS83$ whose activation energies are close to each other (69.3, 63.8 and 64 kJ/mol, respectively (Table 6)). The H fraction related to each trap in Table 6 shows that the fourth peak in $CS83$ contains ≅19.2% of the total H, while the H fraction in the corresponding peaks in $CS62$ and $CS65$ are 7% (fourth peak) and 9.3% (fifth peak), respectively. These irreversible peaks are related to the pearlite/pearlite and/or pearlite/ferrite interfaces which are strong traps for H. As discussed previously, $CS83$ has the highest amount of pearlite/pearlite interfaces, therefore this interface-related peak contains the highest amount of H fraction in this material compared to the other materials.

With a comparison between Fig. 4 (CO_2/H_2S environment) and Fig. 5, the temperatures at which the H desorption stops are higher in values in cathodic charging conditions for $CS62$ and $CS65$. After cathodic charging, more irreversible trap sites are filled by H and cause the H to effuse out at a higher temperature as it can be seen in the TDS spectrum of $CS62$ and $CS65$ compared to the same materials in CO_2/H_2S environment. The H desorption from the deeper traps (peaks 3 and 4 in $CS62$ and peaks 4 and 5 in $CS65$) retards to higher temperatures after cathodic charging (Figs. 4 and 5, Tables 5 and 6). Since the grain size or the pearlite colony size is smaller in $CS83$ and therefore more pearlite/pearlite or pearlite/ferrite interfaces exist in its microstructure, it was expected that the same trend is observed for $CS83$. Moreover, the activation energies of the peaks are almost the same in all materials. However, in $CS83$ the H desorption stops at the same temperature in both CO_2/H_2S environment and in cathodic H charging condition (Fig. 4 (CO_2/H_2S environment) and Fig. 5). As it is shown in Tables 5 and 6, for $CS83$ the H fraction related to the reversible peaks (Peaks 1, 2 and 3) is ≅81% and the H fraction related to the irreversible peak is ≅19.2% in both CO_2/H_2S environment and cathodic H charging condition. Therefore it can be inferred that due to the higher fugacity with cathodic charging, deep traps in $CS62$ and $CS65$ can be more activated while in $CS83$ a higher fugacity is not required to activate deep trap more efficiently.

4.3. Effect of corrosion layer on hydrogen desorption

In Fig. 4, the TDS spectra of all studied materials charged in CO_2 environment, displays that the diffusible or reversible H desorbs gradually leading to a peak related to the irreversible H desorption appearing. Since the H uptake for $CS62$ in CO_2 environment is close to the detection limit of the $G4-Phoenix$, its TDS spectrum is too noisy. Therefore, the TDS spectrum for $CS62$ in CO_2 environment is not deconvoluted. For $CS65$ and $CS83$, the deconvolution is done similarly as for the other conditions. $CS65$ and $CS83$ are deconvoluted to five and four peaks, respectively. However, based on Tables 4, 5 and 6, the reversible and irreversible H fraction is quite different than the same peaks from the same material in the CO_2/H_2S environment or cathodic H charging condition. If the first three peaks in $CS65$ and $CS83$ are considered as the reversible peaks which are related to the traps like ferrite/cementite interfaces, dislocations, micro-voids, and grain boundaries [68], the sum of the H fractions related to the first three peaks in $CS83$ is ≅81% and the H fraction related to the fourth peak which is the irreversible peak is ≅19.2% for both CO_2/H_2S environment and in cathodic H charging condition. For $CS83$, in CO_2 environment the reversible and irreversible H fractions are 39.8% and 60.2%, respectively which is quite different than the corresponding H fractions in CO_2/H_2S environment or cathodic H charging condition. A similar trend can be seen in $CS65$ as well. However, it should be noted that as discussed in the previous section, the fourth peak in this material has a complexity and it can be related to the H desorption from a reversible trap which appears with a delay. To investigate the difference between the TDS spectrum of the studied materials in CO_2 environment and CO_2/H_2S environment, the corrosion layer formed on the surfaces of the materials during the charging process should be studied.

Fig. 6 shows the cross sections of the corrosion layers formed on all materials in both CO_2 and CO_2/H_2S environment. Under cathodic H charging, no corrosion layer is formed. First of all the SEM images show a significant difference in the thickness of the corrosion layers formed on the materials in CO_2 and CO_2/H_2S environment. The corrosion layer thickness range is 17–25 μm for CO_2 environment while it is less than 1 μm for CO_2/H_2S environment. From the thickness observation, it can be deduced that H has to go through a longer route to effuse out from the materials exposed to CO_2 environment. In addition to the thickness, the morphology of the corrosion layer can have a determinant role in H desorption. In a ferritic-pearlitic microstructure, a micro-galvanic cell forms between the ferrite and cementite lamellae which act as the anode and cathode, respectively [78,79]. Therefore, the ferrite lamellae or grains dissolve while the cementite lamellae which are the cathodic components remain in the corrosion layer [80]. The remaining cementite layers in galvanic corrosion cause the corrosion layer to adopt almost the same morphology as the microstructure of the material as can be seen in Fig. 6 for $CS65$ and $CS83$. Therefore, H passes a tortuous path to effuse out of the materials exposed to CO_2 environment. Skilbred et al. [18] used the same materials as in this study in an electrochemical hydrogen permeation cell to measure the hydrogen permeation flux through the steels. Their results showed that the hydrogen uptakes reduced in the steels with the accumulation of remaining Fe_3C, despite increasing corrosion rates over time. They explained that in both pure CO_2 corrosion and in the presence of a small amount of H_2S (less than 1 mbar) hydrogen adsorbed on remaining Fe_3C which is located far from the ferrite phase on the surface of the material and therefore has a small chance for absorption into the steel since the hydrogen diffusivity and solubility in Fe_3C phase is low. In the present study during the TDS measurement both the hydrogen absorbed and uptaken by the material and the hydrogen trapped in the remaining Fe_3C in the corrosion layer is measured.

It can be inferred that in materials exposed to the CO_2 environment, H desorbs with a delay due to the fact that H passes through a tortuous corrosion layer containing remaining Fe_3C that is partially filled with corrosion products and can trap the hydrogen and release it with a delay and as a result the shape of the TDS spectrum is different in this condition (Fig. 4). H desorbs gradually at first due to the slow movement of H through the tortuous corrosion layer. Then a peak appears in higher temperatures which is related to the H desorption delay. In CO_2/H_2S environment, the fast formation of iron sulfide layer in the first stages of corrosion [81] decreases the corrosion rate significantly and therefore a thinner corrosion layer forms under this environmental condition. With a comparison between the TDS spectrum for materials after exposure to CO_2/H_2S environment (Fig. 4) and after cathodic charging (Fig. 5), it can be concluded that the thin corrosion layer formed in CO_2/H_2S environment layer does not change the H desorption rate. These results are in agreement with the study performed by Silva et al. [82]. They evaluated the susceptibility of $API\ 5L\ X65$ steel to hydrogen uptake and hydrogen embrittlement in CO_2 environment containing a low concentration of H_2S, at OCP. Their results displayed that FeS film formed on the steel surface has no effect on hydrogen uptake, but reduced the corrosion rate. Huang et al. [36] showed in their experiments that the iron sulfide film blocks the hydrogen permeation through the steel. However, their results displayed that the iron sulfide film which is formed in low concentration

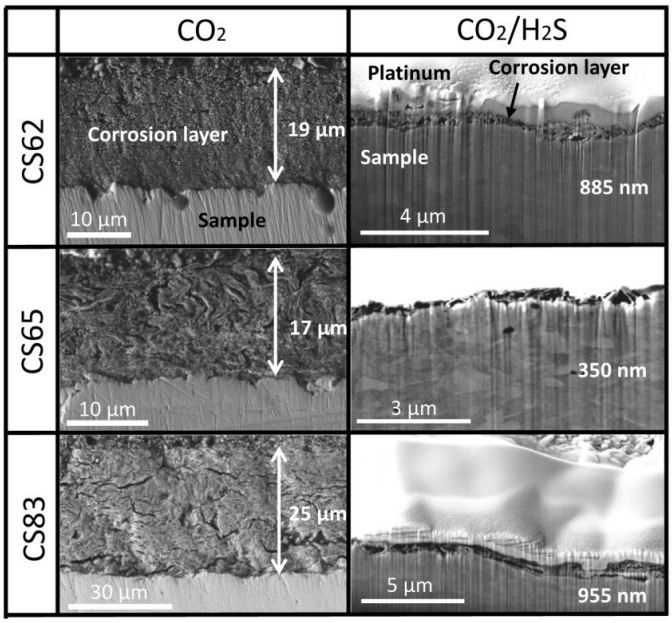

Fig. 6. Cross-section morphologies of the corrosion layers of the studied materials exposed to 0.2 bar CO_2 (left column) and 0.2 bar CO_2/1 mbar H_2S (right column) environments for 21 days. The surface of the samples, exposed to 0.2 bar CO_2/1 mbar H_2S environment, were covered with platinum before milling to protect the nano-scale corrosion layers. The numbers written in each image are the average thickness of the corrosion layers of two samples for each material and environment.

of H_2S has a small effect on hydrogen uptake. Another investigation by Kappes et al. [83] presented that the amount of H_2S is a crucial factor in the formation of the iron sulfide layer and its ability on reducing the hydrogen uptake. In this study, the H_2S concentration is 1 mbar which is considered low. Therefore, the corrosion layer that formed on the material, which is supposed to be a combination of Fe_3C, $FeCO_3$ and FeS, does not make a barrier to retard hydrogen uptake and hydrogen effusion.

5. Conclusions

Hydrogen thermal desorption and hot extraction analysis were performed on three high-strength carbon steels with different cementite morphology and microstructure. These materials were exposed to modified artificial seawater bubbled with CO_2 and H_2S at open circuit potential. The same materials were also charged cathodically in a 3.5% NaCl solution containing 1 g/L thiourea. *TDS* and hot extraction were performed on the materials after testing to evaluate the role of different environments and charging conditions, cementite morphology, and the corrosion layer on hydrogen uptake and hydrogen desorption. All tests were done at room temperature. The following conclusions can be drawn from the present study:

- The hydrogen uptake in all studied materials shows a higher value in the CO_2/H_2S environment compared with the results in the pure CO_2 environment. The H uptake is higher for all materials which are charged cathodically to their saturation in comparison with the materials exposed to CO_2 and CO_2/H_2S environments.
- In CO_2/H_2S environment and cathodic H charging condition, the H uptake increases with carbon content.
- The hydrogen uptake in the material with the lamellar cementite morphology is significantly higher than the material with the spherical cementite morphology with almost similar carbon content, in CO_2/H_2S environment, and cathodic H charging condition.
- In CO_2 environment, the H uptake and the hydrogen desorption are affected by the corrosion layer formed on the steel. In this condition, H desorbs with a delay because H passes through a tortuous corrosion layer containing remaining Fe_3C partially filled with corrosion products that can trap H and release it with a delay.
- The pearlite/ferrite and pearlite/pearlite interfaces act as strong irreversible traps in pearlitic microstructures.
- In CO_2/H_2S environment and cathodic H charging condition, the tortuosity in the lamellar pearlitic microstructures delays the H desorption from the traps. This leads to H desorption continuing at higher temperatures. The high-temperature peak in the *TDS* spectrum of the lamellar pearlitic microstructures can consist of non-diffusible hydrogen and a part of diffusible hydrogen.
- The thin corrosion layer forms in CO_2/H_2S environment does not affect the H desorption rate while based on our previous study it retards the corrosion rate.

CRediT authorship contribution statement

Shabnam Karimi: Conceptualization, Data curation, Investigation, Methodology, Visualization, Writing – original draft, Writing – review & editing. **Iman Taji:** Conceptualization, Data curation, Investigation, Methodology, Writing – review & editing. **Simona Palencsár:** Conceptualization, Data curation, Investigation, Methodology, Writing – review & editing. **Arne Dugstad:** Conceptualization, Data curation, Investigation, Methodology, Writing – review & editing. **Tarlan Hajilou:** Methodology, Writing – review & editing. **Afrooz Barnoush:** Funding acquisition, Supervision, Writing – review & editing. **Kim Verbeken:** Supervision, Writing – review & editing. **Roy Johnsen:** Conceptualization, Funding acquisition, Supervision, Writing – review & editing. **Tom Depover:** Supervision, Writing – review & editing.

Declaration of competing interest

The authors declare the following financial interests/personal relationships which may be considered as potential competing interests: Shabnam Karimi reports financial support was provided by Norwegian University of Science and Technology.

Data availability

Data will be made available on request

Acknowledgments

This work was performed as part of the KPN project "Environmental Cracking of Flexible Pipe Armour Wires", Research Council of Norway project no. 280760 within the $PETROMAKS$ 2 program. The authors would like to thank the following project participants for financial and technical support: The Research Council of Norway, Norway; Equinor, Norway; Shell, Norway; Chevron, United States of America; Petrobras, Brazil; OKEA, Norway; TechnipFMC, France; NOV, Denmark; Baker Hughes, United Kingdom; 4Subsea, Norway.

References

[1] X. Li, M.A. Vaz, Analytical estimation on the number of bending cycles to initiate armour wires lateral buckling in flexible pipes, Ocean Eng. 228 (2021) 108838.
[2] M. Tang, S. Li, H. Zhang, X. Bian, X. Zhao, Monitoring the slip of helical wires in a flexible riser under combined tension and bending, Ocean Eng. 256 (2022) 111512.
[3] S. Papavinasam, Corrosion Control in the Oil and Gas Industry, Elsevier, 2013.
[4] G. Zhang, Y. Cheng, Localized corrosion of carbon steel in a CO_2-saturated oilfield formation water, Electrochim. Acta 56 (3) (2011) 1676–1685.
[5] G. Cooney, J. Littlefield, J. Marriott, T.J. Skone, Evaluating the climate benefits of CO_2-enhanced oil recovery using life cycle analysis, Environ. Sci. Technol. 49 (12) (2015) 7491–7500.
[6] S.C. da Silva, E.A. de Souza, F. Pessu, Y. Hua, R. Barker, A. Neville, J.A.d.C.P. Gomes, Cracking mechanism in API 5L X65 steel in a CO_2-saturated environment, Eng. Fail. Anal. 99 (2019) 273–291.
[7] S.Y. Kondrat'ev, A. Al'khimenko, A. Khar'kov, O. Shvetsov, A. Davydov, Criteria for accelerated estimation of susceptibility of pipe steels to corrosion cracking under oilfield conditions, Metal Sci. Heat Treat. 63 (9) (2022) 533–539.
[8] O. Zvirko, O. Tsyrulnyk, N. Kret, Susceptibility of steel sucker rods operated in oil well to environmentally assisted fatigue, in: Fatigue and Fracture of Materials and Structures, Springer, 2022, pp. 119–125.
[9] X. Wen, P. Bai, B. Luo, S. Zheng, C. Chen, Review of recent progress in the study of corrosion products of steels in a hydrogen sulphide environment, Corros. Sci. 139 (2018) 124–140.
[10] L. Li, J. Wang, J. Xiao, J. Yan, H. Fan, L. Sun, L. Xue, Z. Tang, Time-dependent corrosion behavior of electroless Ni–P coating in H2S/Cl- environment, Int. J. Hydrogen Energy 46 (21) (2021) 11849–11864.
[11] Y. Baik, Y. Choi, The effects of crystallographic texture and hydrogen on sulfide stress corrosion cracking behavior of a steel using slow strain rate test method, Phys. Metals Metallogr. 115 (13) (2014) 1318–1325.
[12] M. Mohtadi-Bonab, M. Eskandari, K. Rahman, R. Ouellet, J. Szpunar, An extensive study of hydrogen-induced cracking susceptibility in an API X60 sour service pipeline steel, Int. J. Hydrogen Energy 41 (7) (2016) 4185–4197.
[13] M. Mohtadi-Bonab, J. Szpunar, R. Basu, M. Eskandari, The mechanism of failure by hydrogen induced cracking in an acidic environment for API 5L X70 pipeline steel, Int. J. Hydrogen Energy 40 (2) (2015) 1096–1107.
[14] C. Dong, Z. Liu, X. Li, Y. Cheng, Effects of hydrogen-charging on the susceptibility of X100 pipeline steel to hydrogen-induced cracking, Int. J. Hydrogen Energy 34 (24) (2009) 9879–9884.
[15] Z. Liu, X. Gao, L. Du, J. Li, P. Li, C. Yu, R. Misra, Y. Wang, Comparison of corrosion behaviour of low-alloy pipeline steel exposed to H_2S/CO_2-saturated brine and vapour-saturated H_2S/CO_2 environments, Electrochim. Acta 232 (2017) 528–541.
[16] P. Kedzierzawski, Hydrogen trapping in iron and iron alloys, in: Hydrogen Degradation of Ferrous Alloys, Noyes Publications, 1985, pp. 271–288.
[17] T. Depover, K. Verbeken, The detrimental effect of hydrogen at dislocations on the hydrogen embrittlement susceptibility of Fe-CX alloys: An experimental proof of the HELP mechanism, Int. J. Hydrogen Energy 43 (5) (2018) 3050–3061.
[18] E.S. Skilbred, M. Kappes, M. Iannuzzi, R. Johnsen, Hydrogen uptake and diffusivity in steel armor wires with different chemical composition, carbide distribution, grain size, and degree of deformation, Mater. Corros. 73 (3) (2022) 326–345.
[19] S. Chan, J. Charles, Effect of carbon content on hydrogen occlusivity and embrittlement of ferrite–pearlite steels, Mater. Sci. Technol. 2 (9) (1986) 956–962.
[20] X. Zhu, W. Li, H. Zhao, L. Wang, X. Jin, Hydrogen trapping sites and hydrogen-induced cracking in high strength quenching & partitioning (Q&P) treated steel, Int. J. Hydrogen Energy 39 (24) (2014) 13031–13040.
[21] M.M. Islam, C. Zou, A.C. Van Duin, S. Raman, Interactions of hydrogen with the iron and iron carbide interfaces: a ReaxFF molecular dynamics study, Phys. Chem. Chem. Phys. 18 (2) (2016) 761–771.
[22] D. Staicopolus, The role of cementite in the acidic corrosion of steel, J. Electrochem. Soc. 110 (11) (1963) 1121.
[23] F. Farelas, M. Galicia, B. Brown, S. Nesic, H. Castaneda, Evolution of dissolution processes at the interface of carbon steel corroding in a CO_2 environment studied by EIS, Corros. Sci. 52 (2) (2010) 509–517.
[24] A. Dugstad, Mechanism of protective film formation during CO_2 corrosion of carbon steel, in: CORROSION 98, OnePetro, 1998.
[25] D. Lopez, W.d. Schreiner, S. De Sánchez, S. Simison, The influence of carbon steel microstructure on corrosion layers: an XPS and SEM characterization, Appl. Surf. Sci. 207 (1–4) (2003) 69–85.
[26] J. Crolet, N. Thevenot, S. Nesic, Role of conductive corrosion products in the protectiveness of corrosion layers, Corrosion 54 (3) (1998) 194–203.
[27] W. Hui, Z. Xu, Y. Zhang, X. Zhao, C. Shao, Y. Weng, Hydrogen embrittlement behavior of high strength rail steels: A comparison between pearlitic and bainitic microstructures, Mater. Sci. Eng. A 704 (2017) 199–206.
[28] Y. Ogawa, H. Nishida, M. Nakamura, V. Olden, A. Vinogradov, H. Matsunaga, Dual roles of pearlite microstructure to interfere/facilitate gaseous hydrogen-assisted fatigue crack growth in plain carbon steels, Int. J. Fatigue 154 (2022) 106561.
[29] R.d.C.P. Loureiro, M. Beres, M. Masoumi, H.F.G. de Abreu, The effect of pearlite morphology and crystallographic texture on environmentally assisted cracking failure, Eng. Fail. Anal. 126 (2021) 105450.
[30] A. Bott, D. Dos Santos, P. De Miranda, Influence of cementite morphology on the hydrogen permeation parameters of low-carbon steel, J. Mater. Sci. Lett. 12 (6) (1993) 390–393.
[31] V. Ramunni, T.D.P. Coelho, P.V. de Miranda, Interaction of hydrogen with the microstructure of low-carbon steel, Mater. Sci. Eng. A 435 (2006) 504–514.
[32] P. Bai, Y. Liang, S. Zheng, C. Chen, Effect of amorphous FeS semiconductor on the corrosion behavior of pipe steel in H_2S-containing environments, Ind. Eng. Chem. Res. 55 (41) (2016) 10932–10940.
[33] E. Wallaert, T. Depover, I. De Graeve, K. Verbeken, FeS corrosion products formation and hydrogen uptake in a sour environment for quenched & tempered steel, Metals 8 (1) (2018) 62.
[34] M.C. Folena, J.A. da Cunha Ponciano, Assessment of hydrogen embrittlement severity of an API 5LX80 steel in H_2S environments by integrated methodologies, Eng. Fail. Anal. 111 (2020) 104380.
[35] C. Zhou, S. Zheng, C. Chen, G. Lu, The effect of the partial pressure of H_2S on the permeation of hydrogen in low carbon pipeline steel, Corros. Sci. 67 (2013) 184–192.
[36] F. Huang, P. Cheng, X. Zhao, J. Liu, Q. Hu, Y.F. Cheng, Effect of sulfide films formed on X65 steel surface on hydrogen permeation in H_2S environments, Int. J. Hydrogen Energy 42 (7) (2017) 4561–4570.
[37] C. Zhou, B. Fang, J. Wang, S. Hu, B. Ye, Y. He, J. Zheng, L. Zhang, Effect of interaction between corrosion film and H_2S/CO_2 partial pressure ratio on the hydrogen permeation in X80 pipeline steel, Corros. Eng. Sci. Technol. 55 (5) (2020) 392–399.
[38] S. Zheng, C. Zhou, P. Wang, C. Chen, L. Chen, Effects of the temperature on the hydrogen permeation behaviours of l360ncs pipeline steel in 1MPa H_2S environments, 2013.
[39] S. Karimi, I. Taji, T. Hajilou, A. Barnoush, R. Johnsen, Evaluation of the cementite morphology influence on the hydrogen induced crack nucleation and propagation path in carbon steels, Int. J. Hydrogen Energy 47 (30) (2022) 14121–14129.
[40] A.S. for Testing, Materials, Standard Practice for the Preparation of Substitute Ocean Water, ASTM International, 2013.
[41] S. Navabzadeh Esmaeely, Y.-S. Choi, D. Young, S. Nešić, Effect of calcium on the formation and protectiveness of iron carbonate layer in CO_2 corrosion, Corrosion 69 (9) (2013) 912–920.
[42] A. Drexler, T. Depover, K. Verbeken, W. Ecker, Model-based interpretation of thermal desorption spectra of Fe-C-Ti alloys, J. Alloys Compd. 789 (2019) 647–657.
[43] H.E. Kissinger, Reaction kinetics in differential thermal analysis, Anal. Chem. 29 (11) (1957) 1702–1706.
[44] J. Lee, J.Y. Lee, Hydrogen trapping in AISI 4340 steel, Metal Sci. 17 (9) (1983) 426–432.
[45] F. Von Zeppelin, M. Haluška, M. Hirscher, Thermal desorption spectroscopy as a quantitative tool to determine the hydrogen content in solids, Thermochim. Acta 404 (1–2) (2003) 251–258.
[46] M.D. Abràmoff, P.J. Magalhães, S.J. Ram, Image processing with imagej, Biophoton. Int. 11 (7) (2004) 36–42.
[47] Y.A. Du, J. Rogal, R. Drautz, Diffusion of hydrogen within idealized grains of bcc Fe: A kinetic Monte Carlo study, Phys. Rev. B 86 (17) (2012) 174110.

[48] Y.A. Du, L. Ismer, J. Rogal, T. Hickel, J. Neugebauer, R. Drautz, First-principles study on the interaction of H interstitials with grain boundaries in α-and γ-Fe, Phys. Rev. B 84 (14) (2011) 144121.

[49] D. Jiang, E.A. Carter, Diffusion of interstitial hydrogen into and through bcc Fe from first principles, Phys. Rev. B 70 (6) (2004) 064102.

[50] K. Verbeken, Analysing hydrogen in metals: bulk thermal desorption spectroscopy (TDS) methods, in: Gaseous Hydrogen Embrittlement of Materials in Energy Technologies, Elsevier, 2012, pp. 27–55.

[51] M. Pinson, L. Claeys, H. Springer, V. Bliznuk, T. Depover, K. Verbeken, Investigation of the effect of carbon on the reversible hydrogen trapping behavior in lab-cast martensitic FeC steels, Mater. Charact. 184 (2022) 111671.

[52] A. Kahyarian, B. Brown, S. Nešić, Electrochemistry of CO2 corrosion of mild steel: effect of CO2 on cathodic currents, Corrosion 74 (8) (2018) 851–859.

[53] C. De Waard, D. Milliams, Carbonic acid corrosion of steel, Corrosion 31 (5) (1975) 177–181.

[54] B. Linter, G. Burstein, Reactions of pipeline steels in carbon dioxide solutions, Corros. Sci. 41 (1) (1999) 117–139.

[55] S. Nesic, J. Postlethwaite, S. Olsen, An electrochemical model for prediction of corrosion of mild steel in aqueous carbon dioxide solutions, Corrosion 52 (4) (1996) 280–294.

[56] E. Remita, B. Tribollet, E. Sutter, V. Vivier, F. Ropital, J. Kittel, Hydrogen evolution in aqueous solutions containing dissolved CO_2: Quantitative contribution of the buffering effect, Corros. Sci. 50 (5) (2008) 1433–1440.

[57] Y. Li, H. Wang, L. Xie, Y. Liang, G. Hong, H. Dai, MoS_2 nanoparticles grown on graphene: an advanced catalyst for the hydrogen evolution reaction, J. Am. Chem. Soc. 133 (19) (2011) 7296–7299.

[58] M. Truschner, A. Trautmann, G. Mori, The basics of hydrogen uptake in iron and steel, BHM Berg-und Hüttenmännische Monatsh. 166 (9) (2021) 443–449.

[59] Y. Cheng, L. Niu, Mechanism for hydrogen evolution reaction on pipeline steel in near-neutral pH solution, Electrochem. Commun. 9 (4) (2007) 558–562.

[60] C. Plennevaux, J. Kittel, M. Fregonese, B. Normand, F. Ropital, F. Grosjean, T. Cassagne, Contribution of CO_2 on hydrogen evolution and hydrogen permeation in low alloy steels exposed to H_2S environment, Electrochem. Commun. 26 (2013) 17–20.

[61] L. Li, J. Yan, J. Xiao, L. Sun, H. Fan, J. Wang, A comparative study of corrosion behavior of S-phase with AISI 304 austenitic stainless steel in $H_2S/CO_2/Cl^-$ media, Corros. Sci. 187 (2021) 109472.

[62] S. Wilhelm, D. Abayarathna, Inhibition of hydrogen absorption by steels in wet hydrogen sulfide refinery environments, Corrosion 50 (02) (1994).

[63] E. Hörnlund, J. Fossen, S. Hauger, C. Haugen, T. Havn, T. Hemmingsen, et al., Hydrogen diffusivities and concentrations in 520 M carbon steel under cathodic protection in 0.5 M NaCl and the effect of added sulphite, dithionite, thiosulphate, and sulphide, Int. J. Electrochem. Sci. 2 (2007) 82–92.

[64] R.D. Kane, M.S. Cayard, Roles of H_2S in the behavior of engineering alloys: a review of literature and experience, in: Corrosion 98, OnePetro, 1998.

[65] R. Kirchheim, Bulk diffusion-controlled thermal desorption spectroscopy with examples for hydrogen in iron, Metall. Mater. Trans. A 47 (2) (2016) 672–696.

[66] Y. Amemiya, N. Nakada, S. Morooka, M. Kosaka, M. Kato, Dynamic accommodation of internal stress and selection of crystallographic orientation relationship in pearlite, ISIJ Int. 62 (2) (2022) 282–290.

[67] R. Silverstein, O. Sobol, T. Boellinghaus, W. Unger, D. Eliezer, Hydrogen behavior in SAF 2205 duplex stainless steel, J. Alloys Compd. 695 (2017) 2689–2695.

[68] A. Laureys, L. Claeys, M. Pinson, T. Depover, K. Verbeken, Thermal desorption spectroscopy evaluation of hydrogen-induced damage and deformation-induced defects, Mater. Sci. Technol. 36 (13) (2020) 1389–1397.

[69] W. Choo, J.Y. Lee, Thermal analysis of trapped hydrogen in pure iron, Metall. Trans. A 13 (1) (1982) 135–140.

[70] D.P. Escobar, K. Verbeken, L. Duprez, M. Verhaege, Evaluation of hydrogen trapping in high strength steels by thermal desorption spectroscopy, Mater. Sci. Eng. A 551 (2012) 50–58.

[71] E. Dabah, V. Lisitsyn, D. Eliezer, Performance of hydrogen trapping and phase transformation in hydrogenated duplex stainless steels, Mater. Sci. Eng. A 527 (18–19) (2010) 4851–4857.

[72] K. Kawakami, T. Matsumiya, Ab-initio investigation of hydrogen trap state by cementite in bcc-Fe, ISIJ Int. 53 (4) (2013) 709–713.

[73] G.-W. Hong, J.-Y. Lee, The interaction of hydrogen and the cementite-ferrite interface in carbon steel, J. Mater. Sci. 18 (1) (1983) 271–277.

[74] W. Choo, J.Y. Lee, Hydrogen trapping phenomena in carbon steel, J. Mater. Sci. 17 (7) (1982) 1930–1938.

[75] K. Takai, R. Watanuki, Hydrogen in trapping states innocuous to environmental degradation of high-strength steels, ISIJ Int. 43 (4) (2003) 520–526.

[76] J.S. Kim, Y.H. Lee, D.L. Lee, K.-T. Park, C.S. Lee, Microstructural influences on hydrogen delayed fracture of high strength steels, Mater. Sci. Eng. A 505 (1–2) (2009) 105–110.

[77] W.M. Robertson, A.W. Thompson, Permeation measurements of hydrogen trapping in 1045 steel, Metall. Trans. A 11 (4) (1980) 553–557.

[78] P.K. Katiyar, S. Misra, K. Mondal, Corrosion behavior of annealed steels with different carbon contents (0.002, 0.17, 0.43 and 0.7% C) in freely aerated 3.5% NaCl solution, J. Mater. Eng. Perform. 28 (7) (2019) 4041–4052.

[79] K. Godbole, K. Mondal, Influence of salinity, total dissolved solids, conductivity, and pH on corrosion behavior of different morphologies of pearlitic steels, J. Mater. Eng. Perform. (2022) 1–11.

[80] R. Cabrera-Sierra, N. Batina, I. González, Electrochemical characterization of pearlite phase oxidation of 1018 carbon steel in a borate medium using ECSTM technique, J. Electrochem. Soc. 152 (12) (2005) B534.

[81] E. Anyanwu, B. Brown, M. Singer, Effect of iron carbide on the morphology and protectiveness of iron sulfide layer, in: Corrosion 2020, OnePetro, 2020.

[82] S. Silva, A. Silva, J.P. Gomes, Hydrogen embrittlement of API 5L X65 pipeline steel in CO_2 containing low H_2S concentration environment, Eng. Fail. Anal. 120 (2021) 105081.

[83] M. Kappes, G. Frankel, N. Sridhar, R. Carranza, Reaction paths of thiosulfate during corrosion of carbon steel in acidified brines, J. Electrochem. Soc. 159 (4) (2012) C195.

Unpublished work

(There is not any plan for publishing this part.)

In this PhD project, six carbon steels with different microstructures were received from the suppliers. These carbon steels are used for the fabrication of the armor wires in flexible pipes. Due to lack of time, for each part of the investigation, 2 to 4 samples were selected to perform the tests on them and analyze their data. The materials selection was based on the necessities and the purpose of that part of the study. However, the TDS tests have been done on all six materials. After doing the experiments, three materials were selected to be presented in paper no.3. More experiments and investigations had been done on the selected materials. In this section, some of the TDS tests results from the materials which are not included in paper no.3, are presented.

Materials characteristics

The composition and mechanical properties of materials CS35 and CS51 are listed in Table 1. These materials are named based on their carbon contents (the same as the materials presented in the papers). The test samples from materials CS35 and CS51 were prepared in the same way as the other samples as described in section 2.1.

Table 1. Chemical composition in wt% and the mechanical properties (yield strength (YS), and ultimate tensile strength (UTS) of the studied materials [66].

Element	C	Al	Si	P	Mo	V	Cr	Mn	Ni	Cu	YS(MPa)	UTS(MPa)
CS35	0.35	0.35	0.32	0.23	0.25	0.6	0.58	0.79	0.56	0.56	610	740
CS51	0.51	0.26	0.40	0.23	0.46	0.70	0.61	1.36	0.89	0.75	870	1000

Figure 1. shows the SEM micrographs of materials CS35 and CS51. Material CS35 microstructure consists of ferrite grains and cementite particles which are mainly located in the grain boundaries. Material CS51 microstructure shows both ferrite and pearlite grains and the cementite phase in this material has various features: the spherical particles, the broken lamella, and the lamellar morphology. The microstructure phase fraction of material CS35 and CS51 is presented in Table 2. The average grain size in materials CS35 is 2.5 µm. The interlamellar spacing in material CS51 is different in different grains. The mean value of the interlamellar spacing in this material is between 119 to 265 based on the ImageJ results. (The microstructure

characterization of material CS28 was presented in paper no.2. These data are not presented here to avoid repetition.)

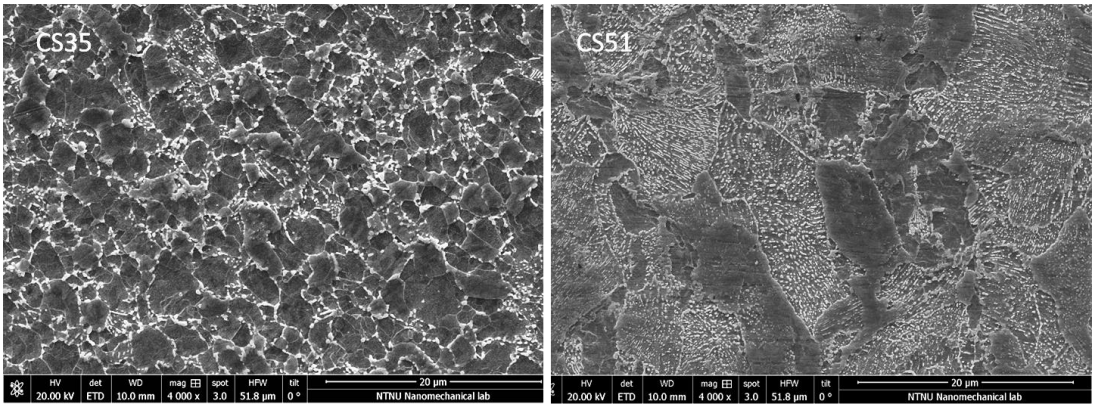

Figure 1. SEM micrographs of materials CS35 and CS51

Table 2. Microstructures phase fraction

Element	Ferrite %	Cementite%	Pearlite-spheroidite %
CS35	95	5	44
CS51	93	7	66

Thermal desorption spectroscopy

All the results which are shown in this section are from the tests performed in the same conditions as presented in paper no.3. The hot extraction test results are presented in Fig.2. The hydrogen uptake of all six materials is presented in this figure for comparison (the hydrogen uptake of materials CS62, CS65, and CS83 from paper no.3).

Material CS35 has a different microstructure in comparison with the other materials. In this material, the cementite particles are mainly located in the grain boundaries, while in the other materials, the cementite phase is distributed in the form of particles, broken lamella, or lamella both in the grain boundaries and inside the grains. Material CS35 shows the lowest hydrogen uptake after exposure to the CO_2/H_2S environment. Materials CS28 and CS51 show a similar amount of hydrogen uptake in the CO_2/H_2S environment. In the CO_2 environment, the hydrogen uptake increases with the carbon content. However, material CS62 with a spheroidite

microstructure shows a lower hydrogen content in comparison with material CS51. This can be related to the role of the corrosion layer morphology that formed on the surface of the

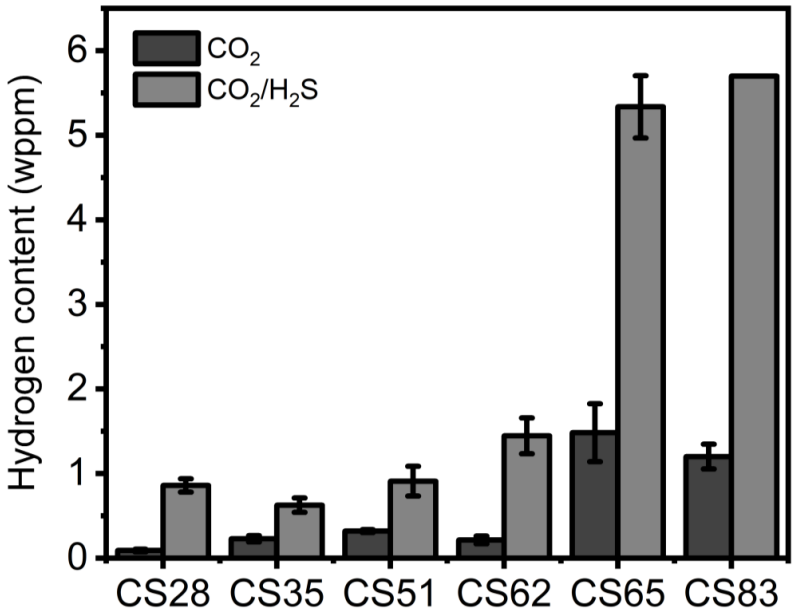

Figure 2. Hydrogen content obtained by hot extraction at 650°C for samples exposed to CO_2 and CO_2/H_2S environments for 21 days at room temperature. The columns show the mean value of three tests and the bars represent the standard deviation of the mean value.

materials in the CO_2 environment on the hydrogen uptake and desorption (discussed in paper no.3). However, more experiments and analyses need to be performed to compare and discuss these results. In the CO_2/H_2S environment, the hydrogen uptake is higher in material CS62 in comparison with material CS51. The TDS curves of materials CS28, CS35, and CS51 obtained at a heating rate of 0.5 K/s after exposure to the CO_2 and CO_2/H_2S environments for 21 days are presented in Fig.3. The curves were fitted and deconvoluted into Gaussian curves with three peaks. The shapes of the TDS spectrum are different for each material. More investigation and analysis are needed to do to discuss the role of the microstructure on hydrogen uptakes and TDS curves. The hydrogen uptake in materials CS28 and CS35 in the CO_2 environment is lower than in material CS51 and is close to the detection limit of the G4-Phoenix analyzer (such as material CS62 in paper no.2). Therefore, the TDS spectrum of these two materials in the CO_2 environment is not presented here. Fig.4 shows the TDS spectrum of material CS51 in the CO_2 environment. It was discussed in paper no.3 that the diffusible or reversible hydrogen

desorbs gradually for materials that are exposed to the CO_2 environment. The corrosion layer that is formed in the CO_2 exposure can lead to this gradual desorption.

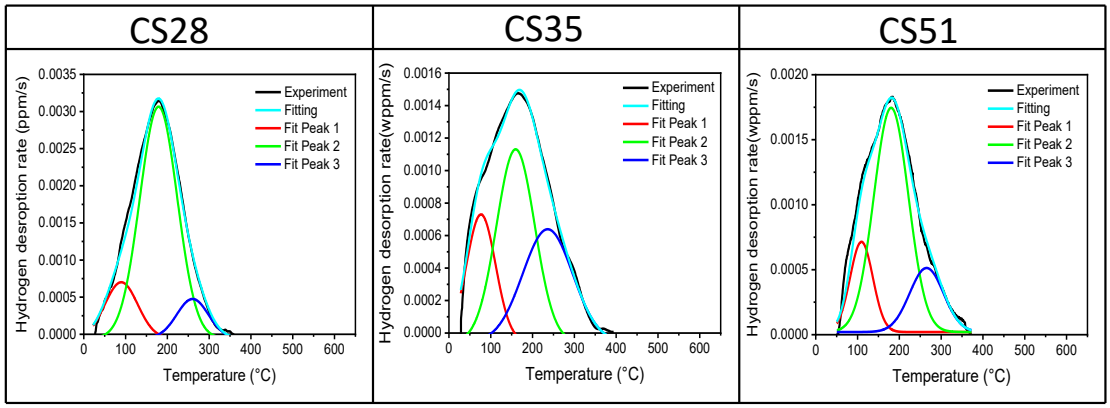

Figure 3. TDS spectra obtained at a heating rate of 0.5 K/s for materials CS28, CS35, and CS51 exposed to 0.2 bar CO_2/1 mbar H_2S for 21 days at room temperature. The deconvoluted curves are associated with hydrogen desorption from particular microstructural features.

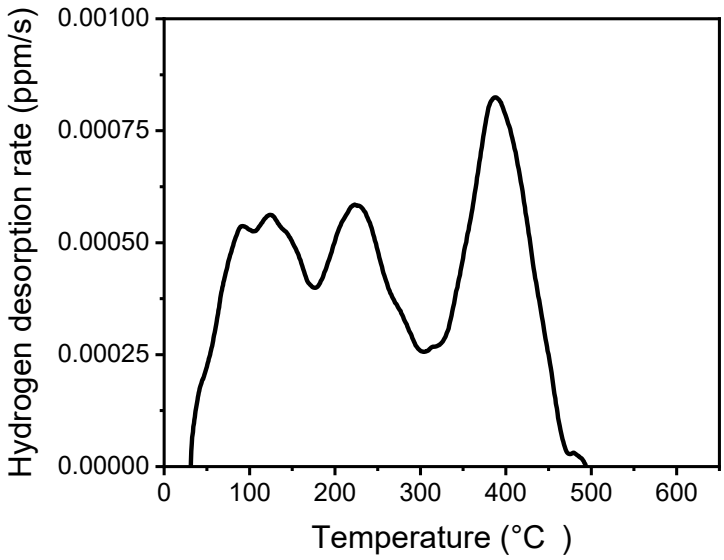

Figure 4. TDS spectra obtained at a heating rate of 0.5 K/s for materials CS51 exposed to 0.2 bar CO_2 for 21 days at room temperature. The deconvoluted curves are associated with hydrogen desorption from particular microstructural features.

ISBN 978-82-326-7184-7 (printed ver.)
ISBN 978-82-326-7183-0 (electronic ver.)
ISSN 1503-8181 (printed ver.)
ISSN 2703-8084 (online ver.)

NTNU

Norwegian University of
Science and Technology